

# Transient Sputtering Method for Estimating Ion Confinement Times in ECRIS Plasma

Master's thesis, 20.8.2018

Author:

MIHA MARTTINEN

Supervisors:

OLLI TARVAINEN

HANNU KOIVISTO





# Tiivistelmä

Marttinen, Miha

Transient Sputtering Method for Estimating Ion Confinement Times in ECRIS Plasma  
Pro Gradu -tutkielma

Fysiikan laitos, Jyväskylän yliopisto, 2018, 108 sivua

Elektronisyklotroniresonanssi-ionilähteillä (ECRIS) tuotetaan korkeasti varattuja ioneja kiihdytinpohjaisen fysiikan tutkimuksen tarkoituksiin. Pitkät ionien säilöntäajat ovat välttämättömiä korkeasti varattujen ionien tuottamiseksi. Tässä Pro Gradussa testataan transienttimenetelmää ionien säilöntäaikojen arvioimiseksi sputteroinnalla.

Tutkielmassa esitellään tarpeellinen tausta plasmafysiikalle, ECR-ionilähteelle ominaisille plasmailmiöille, sekä käytännön menetelmille ionien tuottamiseksi ECR-plasmassa. Kokeellisessa osiossa esitellään sputterointiin perustuva transienttimenetelmä ionien säilöntäaikojen arvioimiseksi ionivirtojen transienttien aikavakioista. Aikavakioiden riippuvuus ionilähteen operointiparametreista analysoidaan nojaten teoreettiseen taustaan, ja sen havaitaan sopivan ionien sähköstaattiseen säilöntämalliin.

Lisäksi työssä tutkitaan ionien tuottoaikoja soveltamalla sputterointimetodia nopeassa sputteroinnissa. Tuottoaikoja verrataan ionivirtojen saturaatioaikoihin, joita käytetään tyypillisesti radioaktiivisten ionisuihkujen tuoton rajakriteerinä. Havaitaan, että ionien tuottoajat ovat merkittävästi lyhyempiä kuin saturaatioajat, mikä on radioaktiivisten ionisuihkujen tuoton kannalta tärkeä havainto.

Avainsanat: ECRIS, ionien säilöntäaika, ionien tuottaminen



# Abstract

Marttinen, Miha

Transient Sputtering Method for Estimating Ion Confinement Times in ECRIS Plasma

Master's thesis

Department of Physics, University of Jyväskylä, 2018, 108 pages.

Electron Cyclotron Resonance Ion Sources (ECRIS) are used for Highly Charged Ion (HCI) production for accelerator based physics research. A necessary condition for HCI production are long ion confinement times. In this thesis, a transient sputtering method for estimating the confinement times is tested.

In this thesis, the necessary background of plasma physics, ECRIS-specific theoretical plasma phenomena, and practicalities of HCI production with the ECRIS are introduced. In the experimental section, a transient sputtering method for estimating ion confinement times based on the ion current transient decay times is presented. The parameter dependence of the decay times is analyzed relying on the theoretical background, and found to be in accordance with the electrostatic ion confinement model.

Additionally, the ion production times are probed by applying the sputtering method in a fast sputtering experiment. The production times are compared to the ion current saturation times, which are typically used as limiting criteria for radioactive ion beam production. It is observed, that the ion production times are significantly shorter than the current saturation times, which is an important finding with respect to radioactive beam production.

Keywords: ECRIS, ion confinement time, ion production



## Kiitokset

Tämä tutkielma on vaatinut aika paljon töitä, mutta sen kirjoittaminen on muuttunut sitä helpommaksi, mitä enemmän sitä on tehnyt, joten uskon oppineeni jotain. Kiitän ohjaajiani ja koko ionilähderyhmää tämän urakan aikana saamastani ohjauksesta, avusta ja neuvoista. Mun on myös välttämätöntä kiittää ystäviäni, joita ilman olisin loppuunpalanut ja joiden ansioista fysiikka on hauskaa. Erityisesti kiitän äitiäni, joka tuntuu tietävän kaikesta muusta paitsi fysiikasta paremmin kuin minä.





# Contents

<b>Tiivistelmä</b>	<b>3</b>
<b>Abstract</b>	<b>5</b>
<b>Kiitokset</b>	<b>7</b>
<b>1 Introduction</b>	<b>11</b>
<b>2 Basic properties of plasmas</b>	<b>13</b>
2.1 Definition of a plasma . . . . .	13
2.2 Charged particle motion in magnetic and electric fields . . . . .	14
2.3 Particle diffusion in magnetized plasma . . . . .	16
<b>3 ECRIS plasma phenomena</b>	<b>19</b>
3.1 Electron confinement . . . . .	20
3.1.1 ECRIS magnetic field configuration . . . . .	21
3.1.2 The loss cone . . . . .	23
3.2 Electron cyclotron resonance heating . . . . .	25
3.3 Plasma potential . . . . .	27
3.4 Collisions in plasma . . . . .	28
3.4.1 Collisions affecting plasma charge state distribution . . . . .	28
3.4.2 Collisions affecting plasma confinement and temperature . . . . .	31
3.5 Plasma temperatures and energy distributions . . . . .	36
3.5.1 Electron temperatures . . . . .	36
3.5.2 Ion temperatures . . . . .	39
<b>4 Production of highly charged ions in the ECRIS</b>	<b>43</b>
4.1 Balance equation of the ion densities . . . . .	44
4.1.1 Confinement time . . . . .	44
4.2 Ion confinement . . . . .	45
4.2.1 Diffusion models . . . . .	48
4.2.2 Spatial distribution of ions . . . . .	53
4.3 Methods for improving ECRIS efficiency . . . . .	56
4.4 Gas mixing . . . . .	58
4.5 Material injection . . . . .	60
4.5.1 Sputtering method for material injection . . . . .	63
<b>5 Experimental setup and methods</b>	<b>65</b>
5.1 JYFL 14 GHz ECRIS . . . . .	67
5.2 Pulsed sputtering method for material injection . . . . .	69

5.3	Transient of the ion current . . . . .	72
5.4	Measurements with the JYFL 14 GHz ECRIS . . . . .	73
5.4.1	Parameter sweep measurements . . . . .	74
5.4.2	Fast sputtering measurements . . . . .	75
<b>6</b>	<b>Results and analysis</b>	<b>77</b>
6.1	Selecting the fitting range . . . . .	78
6.2	Error estimation . . . . .	80
6.3	Parameter sweep results . . . . .	82
6.3.1	The effect of the buffer gas species . . . . .	83
6.3.2	The effect of the minimum-B field . . . . .	84
6.3.3	The effect of the injection pressure . . . . .	85
6.3.4	The effect of sputtering voltage . . . . .	87
6.3.5	The effect of microwave heating power . . . . .	88
6.4	Fast sputtering results . . . . .	89
6.4.1	Production times . . . . .	90
6.4.2	Superpositions . . . . .	93
6.5	Buffer plasma response to sputtering . . . . .	95
6.5.1	Response as a function of the pulse width . . . . .	96
6.5.2	Response in different buffer gases . . . . .	97
6.6	Comparison to literature values . . . . .	99
<b>7</b>	<b>Conclusions and future prospects</b>	<b>101</b>
	<b>References</b>	<b>103</b>

# 1 Introduction

The Electron Cyclotron Resonance Ion Source (ECRIS) is used for highly charged ion (HCI) production for nuclear -and particle physics research, industrial applications and medical purposes. The ECRIS relies on plasma formation via electron impact ionization of gas atoms. The electrons are heated by microwave radiation and confined in a magnetic field. Because of their high collisionality, the ions are not magnetically confined like the electrons, but thanks to the selective heating the ions remain cold and slow moving, which increases their confinement times. Long ion confinement times are necessary for HCI production, because the step-by-step ionization process requires the ions to undergo multiple ionizing collisions with the electrons.

In this thesis, a pulsed sputtering method is applied to measure the ion confinement times in an ECRIS. Sputtering is a method for introducing metallic substances into plasma. A metal (in this work copper) sample is inserted radially into the ECRIS plasma chamber at its edge, and it is biased to a high negative voltage. The negative potential in the metal sample attracts the positively charged ions of the plasma, which are accelerated towards the sample. Upon collision, metal atoms are separated from the sample's surface and they make their way into the plasma. The voltage can be operated in a pulsed mode using a TTL control signal to switch it on and back off again.

By varying the different ECRIS parameters: the magnetic field, the microwave heating power, plasma chamber pressure, buffer gas species and the sputtering voltage, it is possible to perform a factor analysis of the extracted  $m/q$ -analyzed ion current decay time. The decay times of the different charge states have been measured in sweeps of the aforementioned parameters, and the response of the decay time has been analyzed.

Ion production times have also been investigated with a fast sputtering experiment. By making the sputtering times shorter, the amount of metal introduced into the plasma decreases, and the disturbance caused by the sputtering voltage becomes smaller. Due to the time that it takes the metal atoms to become ionized, for the shortest sputtering pulses the sputtering voltage is switched off before any current is measured. As such, the measured current corresponds to a plasma that is not disturbed by the sputtering voltage. By integrating the current it is thus possible to determine, how quickly ions of particular charge are extracted from the ion source after material injection into the source. It is of particular importance to be able accurately to determine ion production times when it comes to radioactive beams. In this case the time to produce ions needs to be short. If the production times are very long in comparison to the half lives of the beam particles, sufficient beam intensities cannot be reached due to in-beam decay.

The text is arranged as follows: The fundamental properties of plasmas are introduced in section 2, and the ECRIS specific plasma phenomena are described in section 3. Then, in section 4, the conditions (including the confinement time) and methods for efficient

production of highly charged ions are discussed. The development of the experimental setup and methods are shown in section 5, and the results of the experiments and their analysis in section 6. Finally, conclusions are drawn in section 7.

## 2 Basic properties of plasmas

Plasma is an ionized gas consisting of charged ions, electrons and neutral atoms and molecules exhibiting collective behavior under the influence of electromagnetic fields. A plasma is formed when a gas is heated until the particle-particle collisions are intense enough to cause electrons to be removed from the neutral particles. Because the ionization process does not involve a specific heat but is continuous in nature, there is no clearly defined phase shift between a gas, a very weakly ionized gas, and a plasma. Typically, however, once the ionization degree of the gas exceeds a few percent it exhibits collective motion, and thus can be considered to be plasma [1]. Because of the abundance of free ions, plasmas are a good basis for ion source operation. In this section the basic properties of plasmas distinguishing them from gases are briefly covered.

### 2.1 Definition of a plasma

Plasmas are quasi-neutral – i.e. approximately macroscopically neutral, but can have internal charge distributions – and thus their properties are dominated by electromagnetic interactions[2]. In a cold plasma (such as in ion sources), the massive ions move slowly relative to the electrons, which may be considered to oscillate about the ions in their electric potential: The charge separation causes an electric force to manifest between the electrons and ions, which causes a harmonic oscillation of the electrons about the ions. The angular frequency of the electrons' oscillation about the ions, or the so-called electron plasma oscillation frequency is given by[2]

$$\omega_{pe} = \left( \frac{e^2 n_e}{\varepsilon_0 m_e} \right)^{1/2}, \quad (1)$$

where  $m_e$  is the electron mass,  $e$  is the elementary charge,  $\varepsilon_0$  is the vacuum permittivity, and  $n_e$  is the electron number density. In order for this oscillation to take place, the motion must not be significantly perturbed by collisions with neutrals, that is:  $\omega_{pe} \gg \omega_{en}$ , where  $\omega_{en}/2\pi = \nu_{en}$  is the electron-neutral collision frequency. If this condition is not met, the properties of the gas are determined by the neutral atoms, and the gas cannot be considered a plasma. Usually this condition is met when the ionization degree exceeds a few percent[1].

The kinetic energy of the electrons determines the amplitude of the oscillation, i.e. the charge separation. Therefore, based on the electron temperature a measure of the charge separation can be derived, and it is given by the Debye-Hückel length [3, 2]

$$\lambda_D = \left( \frac{\varepsilon_0 k_B T_e}{e^2 n_e} \right). \quad (2)$$

Deviations in the plasma charge neutrality are in the scale of the Debye-Hückel length (often referred to simply as the Debye length). Because of this, the condition for plasma quasi-neutrality is determined such that the characteristic dimension of the plasma  $L$  is required to be much greater than the Debye length, i.e.  $L \gg \lambda_D$ . Furthermore, in the derivation of the Debye length it is assumed that there is a statistically significant number of electrons present, which is achieved if  $n_e \lambda^3 \gg 1$ , where the cube of the Debye length is termed the 'Debye sphere.' Based on these conditions it can be said, that an ionized gas can be considered a plasma when deviations from charge neutrality are small in comparison to the the size of the volume occupied by the gas, and the degree of ionization is high enough for the charged particles to dominate the dynamics of the gas.

## 2.2 Charged particle motion in magnetic and electric fields

Laboratory plasmas are confined by magnetic fields, the plasma heating is often achieved via radiowave absorption by the plasma, and an electric field arises across the plasma sheath due to the plasma potential (see section 3). Additionally, the quasi-neutrality of the plasma allows small scale electric fields to manifest between the particles. The plasma dynamics are governed by interactions between the constituent particles and these fields. The following treatment[2] can be used to model single particle motion in electric -and magnetic fields:

Considering a single particle with mass  $m$  and charge  $eq$ , moving at velocity  $\vec{v}$  in a magnetic field  $\vec{B}$  and acted upon by the stationary force  $\vec{F}$ , its equation of motion is

$$m\dot{\vec{v}} = eq\vec{v} \times \vec{B} + \vec{F}, \quad (3)$$

where the time derivative is designated with the dot. This equation may be separated to its components perpendicular ( $\perp$ ) and parallel ( $\parallel$ ) to the magnetic field. The velocity, for example, may be written as  $\vec{v} = \vec{v}_\perp + \vec{v}_\parallel$ . The cross product term in the equation has only components perpendicular to  $\vec{B}$ . Parallel to  $\vec{B}$  the equation thus describes acceleration determined by the force  $\vec{F}_\parallel$ . Perpendicular to the magnetic field we have

$$m\dot{\vec{v}}_\perp = eq\vec{v}_\perp \times \vec{B} + \vec{F}_\perp, \quad (4)$$

which is a system of two coupled, inhomogeneous differential equations.

The homogeneous part of equation (4) is

$$m\dot{\vec{v}}_\perp = eq\vec{v}_\perp \times \vec{B}, \quad (5)$$

whose solution describes particle gyromotion in a plane whose normal is along the magnetic field line. The gyration occurs at constant speed  $v_\perp$  at a Larmor radius

$$r = \frac{mv_\perp}{eqB}. \quad (6)$$

and at an angular frequency

$$\omega = \frac{eqB}{m}, \quad (7)$$

where the sign of the charge state  $q$  determines the direction of rotation (The direction can be obtained easily according to the well known 'right hand rule': right handed rotation for positive charges, left handed for negative).

The inhomogeneous part of (4), in the special case of constant velocity  $\vec{v}_\perp$  is

$$-eq\vec{v}_\perp \times \vec{B} = \vec{F}_\perp \quad (8)$$

and it can be solved by taking its cross-product with  $\vec{B}$ , i.e.

$$\vec{v}_\perp = \frac{\vec{F} \times \vec{B}}{eqB^2} \equiv \vec{v}_{\text{drift}}. \quad (9)$$

The result is the so-called drift velocity  $\vec{v}_{\text{drift}}$  in the direction perpendicular to both  $\vec{B}$  and  $\vec{F}$ , which causes the particles to drift across the magnetic field from one field line to another. The particle drifts can be caused by such forces as those arising from electric fields ( $\vec{F} = eq\vec{E}$ ), the magnetic field gradient ( $\vec{F} = -\mu\nabla B$ ; where  $\mu$  is the magnetic dipole moment) or particle density gradients (in the case of stellar and ionospheric plasmas gravity also causes notable particle drift). The single particle motion in the transverse magnetic plane is thus a combination of the gyromotion about the field line and the drift across the field lines.

The drift caused by a magnetic field gradient  $\nabla B$  is relevant for the purposes of ECR ion sources. The magnetic field gradient causes charged particles gyrating in the field to move perpendicular to the magnetic field, or towards regions of lower magnetic field. The  $-\nabla B \times \vec{B}$ -drift that causes the particle to drift across the field lines, and a gradient parallel to  $\vec{B}$  the charged particles drift towards weaker magnetic field due to the conservation of the magnetic dipole moment of the gyrating particle. This effect is used in the ECRIS to achieve electron confinement in the so-called 'magnetic bottle' and it is treated more thoroughly in section 3.1.

## 2.3 Particle diffusion in magnetized plasma

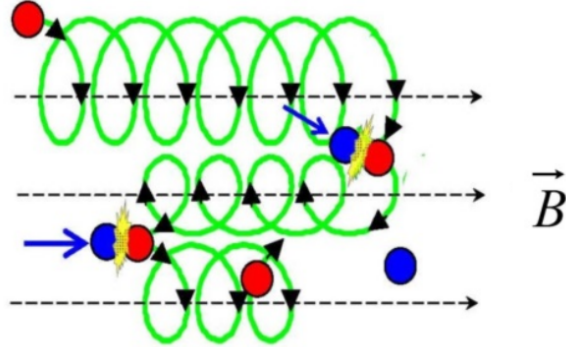


**Figure 1.** Diffusion of a charged particle across magnetic field lines. The positively charged particle (red sphere) collides with neutrals (blue spheres) as it spirals about the field lines. Arrows indicate the trajectories of the neutrals, which are unaffected by the field. The particle trajectory begins in the upper left corner. Note the change in direction parallel to the magnetic field  $\vec{B}$  caused by the collisions. Figure adapted from [2].

Unlike in the case of a simple gas at equilibrium, the motion of particles in a plasma is not governed by Brownian motion, due to the long range Coulomb interactions between the charged particles. A magnetic field applied across the plasma will further alter the dynamics of the system. This section presents a brief version of the treatment of diffusion in a magnetized plasma by [2].

Temperature and density gradients cause particle flows along the gradient in a transport process referred to as diffusion. Diffusion is described by Fick's laws, which state that the diffusive particle flux

$$\vec{\Gamma}_{\text{diff}} = -D\nabla n, \quad (10)$$

where  $D$  is the diffusion coefficient, and  $n$  the particle density. Here the diffusion coefficient for electrons and ions ( $e,i$ ) is determined by the particle mobilities and temperatures according to the Einstein relation

$$D_{e,i} = b_{e,i}k_B T_{e,i} \approx \nu\lambda_{\text{mfp}}^2, \quad (11)$$

The mobility  $b_{e,i}$  is a proportionality constant describing the friction between the electrons or ions and the other plasma particles: In the case of a weakly ionized plasma the friction is due to collisions with neutrals, while in a fully ionized plasma the collisions are between the charged particles. The collisions take place at the frequency  $\nu$  and determine the particle mean free path  $\lambda_{\text{mfp}}$ <sup>1</sup>. Equation (10) shows that the diffusion happens from

<sup>1</sup>Collisions also cause the particle velocities to be changed, which has important consequences with respect to electron confinement in an ECRIS, as described in section 3.1.

regions of higher particle density towards lower densities. Meanwhile equation (11) shows that particles with higher mobility and temperature have higher particle fluxes in absence of ambipolar electric fields balancing the fluxes.

Applying a magnetic field onto the plasma causes the mobility to differ along and across the magnetic field, due to the gyromotion of the charged particles about the field lines. This is illustrated in figure 1, which shows a charged particle spiraling in a magnetic field  $\vec{B}$ . In the figure, the particle is deflected from one field line to another in collisions with neutral particles, whereupon its velocity vector also changes leading to a change in its Larmor radius and possibly the direction of its motion along  $\vec{B}$ . From the figure it can be deduced, that while the diffusion of the particle along  $\vec{B}$  is still determined by the mean free path between collisions ( $\lambda_{\text{mfp}}$  in equation (11)), the diffusion across the field is now governed by the Larmor radius. Therefore, the diffusion coefficient for particles in a magnetized plasma needs to be defined independently perpendicular and parallel to  $\vec{B}$  as  $D_{\perp}^{e,i}$  or  $D_{\parallel}^{e,i}$ .

Because the Larmor radius determines the average step size of a charged particle diffusing perpendicular to the magnetic field, it is the electron which is the slow particle when diffusing in the transverse magnetic plane, as its Larmor radius is much smaller than that of the relatively massive ion. Meanwhile, in the direction parallel to the magnetic field the ions are the slower particle to diffuse – mainly due to their large mass, which decreases their mobility, but also due to their smaller temperature. In an ECRIS, however, the electrons diffuse out of the plasma at an overall faster rate, which leads to the build up of a positive 'plasma potential' relative to the vessel containing the plasma. This phenomenon is important, and is looked at more closely in section 3.3.



### 3 ECRIS plasma phenomena

The operation of an Electron Cyclotron Resonance Ion Source (ECRIS) is based on the confinement and heating of electrons, and subsequent electron impact ionization of the injected gas. The electron confinement is realized by a minimum-B magnetic field structure, which has a minimum close to the plasma center and thence increases in every direction. In the minimum-B configuration the magnetic field structure forms closed constant-B surfaces roughly the shape of American footballs (prolate spheroids). The electrons follow helical orbits around the magnetic field lines and thus, as they travel towards an increasing B-field, they experience a force which tends to reflect them back towards the plasma center [4].

In the ECRIS the electron heating is achieved via absorption of microwaves. As the electrons cross the so called ECR surface in the magnetic field, where the angular frequency of the electrons' orbital motion about the field lines is in resonance with the microwave frequency, as discussed later, the electrons crossing the ECR surface in the accelerating phase can absorb energy from the microwave. The electrons in the accelerating phase gain more energy than is lost by electrons crossing the ECR surface in the decelerating phase, which means that statistically the electrons gain energy. Because the heating affects mainly the electron's velocity component perpendicular to the magnetic field lines, the heating improves the electron confinement. Thus, a well confined hot electron population accumulates in the center of the plasma, and a cold electron population in the outer regions.

The plasma is formed as energetic electrons ionize gas atoms injected into the plasma chamber. The ionization occurs step-by-step, which means that Highly Charged Ion (HCI) production requires ions to undergo multiple ionizing collisions with electrons. As such, the ions need to have long confinement times and the electron number densities must be sufficiently high to reach high charge states, as formulated later in equation (34) in section 4.

Collisions define many of the plasma phenomena relevant to ECRIS. Electron confinement is limited by their collisionality, as the requisite for magnetic confinement is that the gyromotion of the electrons is unperturbed. If the electron is deflected from its orbit by a collision before the period is complete, it undergoes no true gyromotion in the field and cannot be confined. The same is true for the high charge state ions, which indeed are not magnetically confined due to their collisionality[5, 6]. The diffusion of electrons into the loss cone is governed by collisions, microwave induced scattering and non-linear effects [7].

Due to the small mass and higher mobility of the electrons they tend to diffuse out of the plasma at a faster rate than the ions. Therefore, the plasma develops a charge imbalance with the plasma being at a higher potential than the plasma chamber walls. This

potential difference is termed the plasma potential. As the plasma potential increases, it increasingly retards the electrons and conversely accelerates the ions, until the diffusion rates of negative and positive charges equilibrate in the plasma – an effect termed ambipolar diffusion.

In a plasma, there are two (or three) electron populations each having different temperature: the cold, (warm) and hot electron population. Since the hot electrons are well confined in the plasma center, it is the population of cold electrons that is mainly responsible for the build up of the plasma potential. Meanwhile in the plasma center the hot electrons are slightly slower to diffuse out of the region. Thus, in analogy with the build up of the plasma potential, a potential dip is formed in the plasma center[6, 8]. No direct measurement has so far provided evidence for the potential dip, but its existence is strongly suggested by indirect evidence and theoretical models, as will be seen later.

The collisions also determine the energy equipartition rates between electron and ion populations, since the energy transfer occurs in collisions between them. The collision frequency decreases as the energy of the particle increases, and as such the energy equipartition times between the hot electrons and the ions are much longer than the ion production times<sup>2</sup>, which means that the ions will not reach the high energies of the hot electrons. Equipartition between the cold electrons and the ions on the other hand is possible, and the ions could be reasonably expected to attain energies in the (10 – 20) eV range typical to cold electrons. Typically, however, the ions are assumed to be quite cold, having a temperature of a few eV[5, 9].

As ions in the ECRIS plasma are too collisional to be magnetically confined, the ion confinement is believed to be electrostatic: the ions are confined in the potential dip generated by the hot electron population in the plasma core. This is especially beneficial with respect to HCI production, as the potential dip traps especially highly charged ions, which are produced in the core plasma. An additional benefit gained from the accumulation of the hot electrons in the plasma chamber is, that as the charge state of an ion increases, so does the energy required for further ionization. Thus, the necessary large number densities of hot electrons for HCI production can be realized in the ECRIS. The following subsections discuss the processes introduced here in detail.

### 3.1 Electron confinement

Both the ECRIS plasma confinement and heating rely on the magnetic field configuration of the ion source. The magnetic field of the ECRIS is arranged in a minimum-B configuration, which has its minimum near the plasma center and increases into all directions therefrom. The field generates the ECR surface where energy transmission from microwaves to electrons is possible, and it confines the electrons, which follow helical orbits about the magnetic field lines.

The electron confinement is based on the restorative force experienced by a charged particle as it spirals towards increasing magnetic field. The necessary condition for the

---

<sup>2</sup>The production time is a measure of the time it takes for a particle to be both ionized and lost from the plasma.

electrons to be confined is that the electron orbital angular frequency  $\omega_{ce}$  about the magnetic field lines must be much higher than the electron-electron collision frequency  $\omega_{ee}$ , mathematically stated as

$$\omega_{ce} \gg \omega_{ee}. \quad (12)$$

When this condition is satisfied, the electrons can be considered to undergo true circular motion required for them to experience the restoring force.

The velocity component perpendicular to the magnetic field  $v_{\perp}$  is favored in the heating (see section 3.2), and consequentially the heated electron moves further away from the so-called loss cone in velocity space. In this way, the ECR-heating improves the electron confinement. Furthermore, if the electron gains enough energy as it crosses the ECR-surface, the point  $B_{\text{ECR}}$  may become its mirror point (the reflection point as explained below). Then the electron is reflected back towards the center of the plasma, and it becomes trapped inside the ECR-surface, where it will repeatedly bounce against the surface absorbing more and more energy, and becoming better and better confined. As such, a population of hot electrons accumulates in the center of the plasma. The confinement of electrons allows them to encounter the resonance zone multiple times, which leads to increased electron energies necessary to further ionize highly charged ions, and the good confinement of hot electrons makes the conditions in the plasma center favorable for HCI production.

### 3.1.1 ECRIS magnetic field configuration

In an ECRIS, the magnetic field is formed by superposing an axial solenoid field with a radial multipole field. In typical room-temperature ECR ion sources solenoid field is generated by coils at the injection and extraction ends of the plasma chamber and the multipole field by permanent magnet rods. In superconducting ECRIS the permanent magnets are replaced by coils. The minimum-B configuration in the ECRIS could also be realized by superposing a quadrupole field onto the solenoid field. This would improve the radial confinement by reducing the number of available loss channels for the particles. The improved confinement would come at the cost of a less optimal extraction, as the end-loss flux would have a rectangular shape. Thus, the hexapole field is a compromise between confinement and extraction[10].

The effect of the superposed axial and radial fields is to generate a so called minimum-B magnetic field configuration. In this configuration the magnetic field is composed of constant-B surfaces roughly in the shape of American footballs (prolate spheroids), such that the field has its minimum near the center of the plasma chamber. Thus, any charged particle in the center of the plasma chamber will see an increasing magnetic field gradient in every direction. As the electrons are on helical orbits about the magnetic field lines, they will feel a force

$$\vec{F} = -\mu\nabla B, \quad (13)$$

where  $\mu$  is the magnetic moment generated by the electron's orbital motion. The effect of the force is to resist the electron motion in the direction of the increasing magnetic field density.

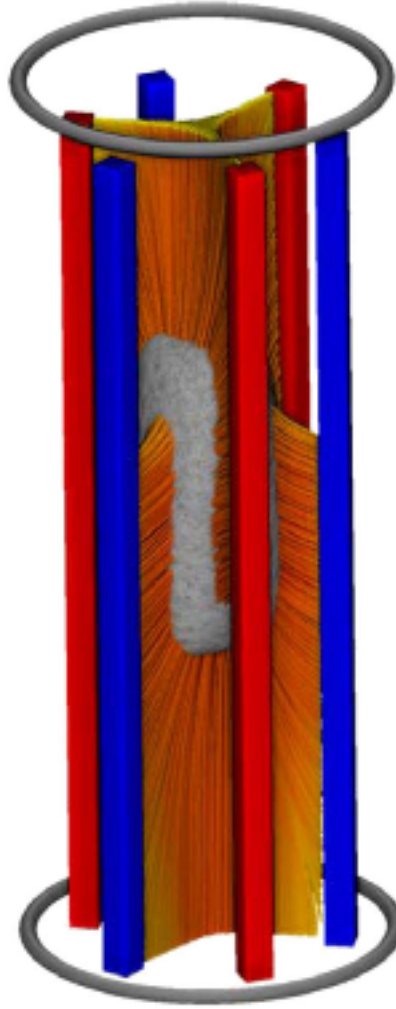


**Figure 2.** The magnetic field lines crossing the ECR zone (illustrated as gray in the figure). From [11].

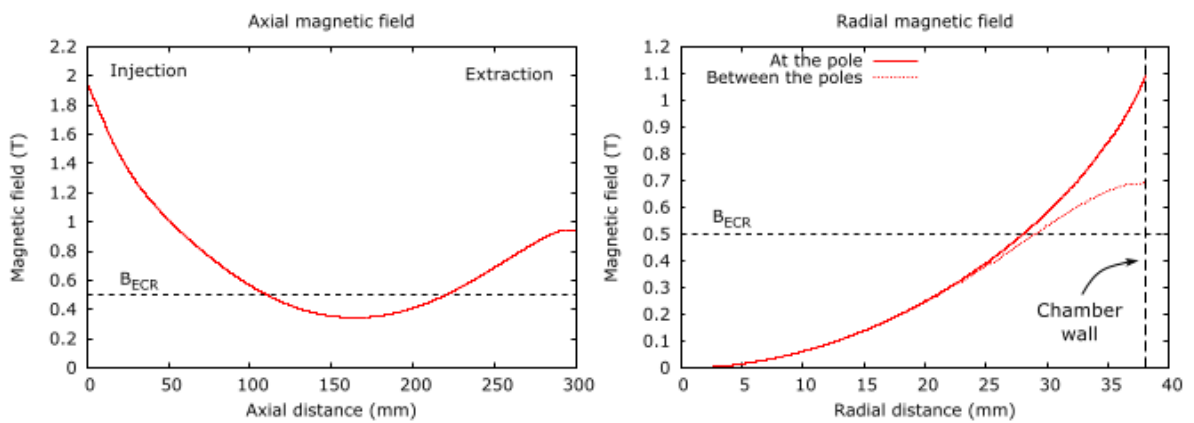


**Figure 3.** Minimum-B field strength axially and radially in the JYFL 14 GHz ECRIS. From [12].

In figure 2 are shown the magnetic field lines forming the ECR surface, and in figure 3 the magnetic field intensity in the axial and radial directions. Note the axially twisting, triangular shape assumed by the magnetic field lines as the superposition of the solenoid and hexapole fields. The plasma itself will conform to this shape set by the field lines.

### 3.1.2 The loss cone

Consider a particle having charge  $q$  and mass  $m$  orbiting about a magnetic field line with velocity  $v^2 = v_{\perp}^2 + v_{\parallel}^2$ , where the velocity is expressed in terms of its components perpendicular and parallel to the magnetic field. Its magnetic moment is

$$\mu = IA = \frac{|q|v_{\perp}}{2\pi r_L} \cdot \pi r_L^2 = \frac{W_{\perp}}{B}, \quad (14)$$

where the Larmor-radius  $r_L = mv_{\perp}/|q|B$ , and the kinetic energy associated with the perpendicular velocity component is  $W_{\perp} = mv_{\perp}^2/2$ . In a static magnetic field  $\mu$  is conserved, and in the absence of electric fields the total kinetic energy  $W = W_{\perp} + W_{\parallel}$  is also conserved. Thus, from equation (14) it can be seen, that as the particle moves towards regions of stronger  $B$ , the parallel kinetic energy component must decrease to maintain a constant  $\mu$ .

Defining the velocity space in terms of the velocity components perpendicular and parallel to the magnetic field, the pitch angle between the components is

$$\tan \theta = \frac{v_{\perp}}{v_{\parallel}} \quad (15)$$

and  $v_{\perp} = v \sin \theta$ , which means that we can write also  $W_{\perp} = W \sin^2 \theta$ . As such

$$\mu = \frac{W \sin^2 \theta}{B}. \quad (16)$$

For any two points in the magnetic field

$$\mu_1 = \frac{W \sin^2 \theta_1}{B_1} = \frac{W \sin^2 \theta_2}{B_2} = \mu_2 \quad (17)$$

or

$$\frac{\sin^2 \theta_1}{\sin^2 \theta_2} = \frac{B_1}{B_2}. \quad (18)$$

As the particle moves towards increasing magnetic field, its parallel velocity component decreases. The condition for the particle to be reflected before exiting the magnetic bottle is that the component  $v_{\parallel}$  goes to zero at the point of maximum magnetic field. As  $v_{\parallel} \rightarrow 0$  the pitch angle  $\theta \rightarrow \pi/2$  according to equation (15). Assuming the point 2 as the mirror point, it follows that

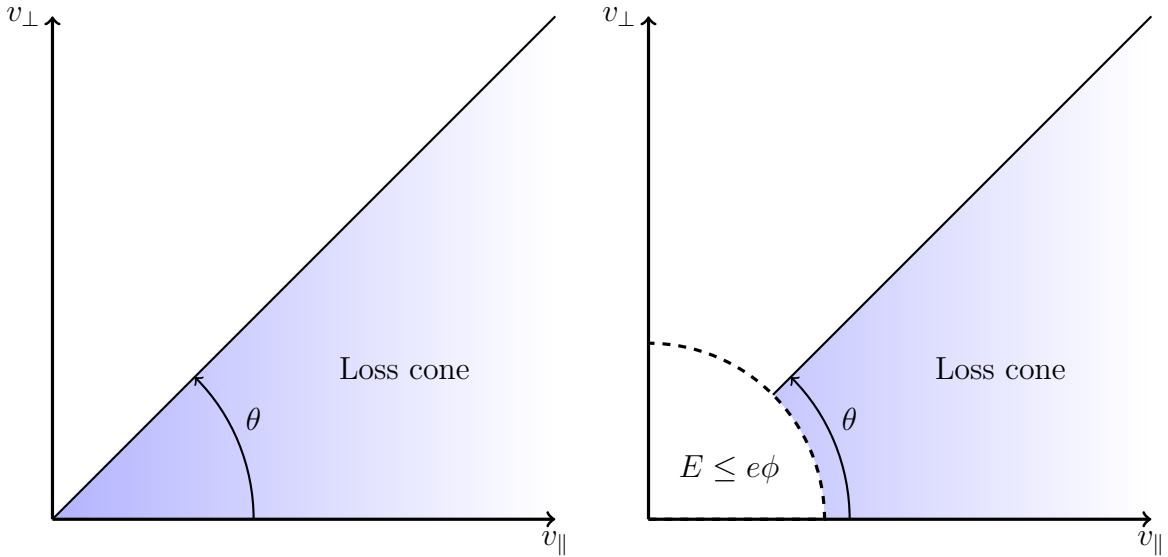
$$\theta_1 = \arcsin \sqrt{\frac{B_1}{B_{\max}}}. \quad (19)$$

Taking the point 1 as the point of origin for the particle, equation (19) determines the minimum pitch angle required for the particle to be trapped in the magnetic bottle (i.e.

its pitch angle being 90 degrees corresponding to  $v_{\parallel} = 0$  at  $B = B_{\max}$ ). For electrons this gives

$$\theta = \arcsin \sqrt{\frac{B_{\text{ECR}}}{B_{\max}}} = \arcsin \sqrt{\frac{1}{R}}, \quad (20)$$

where the ECR zone is taken as the point of origin for the electron, because the conservation of the magnetic moment is broken due to energy gain as the electron crosses the resonance. Thus, the ECR surface is the only logical solution for the point of origin of the electrons. The value  $R = B_{\max}/B_{\text{ECR}}$  is referred to as the magnetic mirror ratio. This relation between the magnetic field at the ECR-surface and the field maximum defines the so-called loss cone in velocity space. Any particles inside the loss cone have a large enough parallel velocity component to escape the magnetic confinement and will be lost from the plasma. While ECR heating will predominantly increase the perpendicular velocity components of electrons collisions diffuse particles into the loss cone. The loss cone is illustrated in figure 4. The effect of the positive plasma potential (see section 3.3) is to confine the electrons, which modifies the loss cone such that only electrons having energies sufficient to overcome the plasma potential can escape.



(a) Loss cone without the plasma potential

(b) Loss cone modified by the plasma potential.

**Figure 4.** Illustration of the loss cone in velocity space. The electron velocity is expressed in terms of its components perpendicular ( $v_{\perp}$ ) and parallel ( $v_{\parallel}$ ) to the magnetic field lines. The pitch angle  $\theta$  defines the loss cone. The plasma potential  $\phi$  truncates the loss cone into a loss hyperboloid by confining electrons with energies  $E$  less than the barrier height  $e\phi$ .

### 3.2 Electron cyclotron resonance heating

In an ECRIS the plasma heating is realized by microwaves. The electrons absorb energy from the microwaves on the so-called ECR-surface, where the electrons' orbital angular frequency  $\omega_{ce}$  about the magnetic field line is the same as the microwave frequency  $\omega_{RF}$ . The frequency can be derived from the Lorentz force to be

$$\omega_{ce} = B \cdot \frac{e}{\gamma m_e}, \quad (21)$$

where  $e/m_e$  is the charge to mass ratio for the electron. The relativistic gamma factor  $\gamma = 1/\sqrt{1 - (v/c)^2}$  is taken into account, because the ECR heating causes a fraction of the electrons to have relativistic energies. The corresponding angular frequency for ions can be obtained by substituting the ion's mass in place of the electron mass. On the ECR-surface  $\omega_{ce} = \omega_{RF}$ . Thus equation (21) determines the location of the ECR-surface as

$$B_{\text{ECR}} = \omega_{RF} \cdot \frac{\gamma m_e}{e}. \quad (22)$$

If the electron gains enough energy at the resonance surface, the surface becomes its mirror point, and the electron is trapped inside the ECR-surface. The electron then begins to bounce-oscillate within the surface, being periodically reflected back towards the plasma center at the resonance zone.

An electron encountering the resonance zone can gain or lose energy depending on the phase difference between the electron's orbital motion and the microwave. An electron in the accelerating phase absorbs energy and thus its Larmor-radius grows. The larger radius corresponds to a longer circular path in the ECR-region, and thus a larger energy gain  $\int F \cdot dl$  along the path. Overall, therefore, the electrons will statistically gain energy as they encounter the resonance zone.

The ECR heating has an upper limit, which is reached when the relative phase of the microwave and the bounce-oscillations becomes locked at a constant value, and the heating ceases to be stochastic [13, and references therein]. On the other hand, the upper limit of the electron energies is limited by the maximum magnetic field intensity. As an electron's energy increases, the relativistic effects cause its respective ECR zone to shift towards stronger magnetic field values (as can be seen from equation (22)). If the relativistic resonance field is stronger than anywhere inside the plasma chamber, the heating cannot take place.

The electrons' velocity components change at the resonance according to the equations [9]

$$\Delta v_{\parallel} = \frac{eE}{m_e} \frac{v_{\perp}}{v_{\phi}} \sqrt{\frac{\pi}{\omega' v_{\parallel}}} \quad (23)$$

and

$$\Delta v_{\perp} = \frac{eE}{m_e} \left(1 - \frac{v_{\parallel}}{v_{\phi}}\right) \sqrt{\frac{\pi}{\omega' v_{\parallel}}}, \quad (24)$$

where  $E$  is the RF electric field and  $v_{\phi} = \omega/k$  is the phase velocity of the wave. The derivative of the orbital angular frequency  $\omega'$  originates from the expansion  $\omega_c(z) \approx$

$\omega_R + \omega'(z - z_R)$ , in which  $z_R$  and  $\omega_R$  refer to the position of the resonance and the electron angular frequency at the resonance respectively ( $z$ -axis defined along the static magnetic field). From the equations it can be seen, that at velocities low relative to the phase velocity of the propagating microwave the electrons gain mainly transverse energy, while at high velocities the perpendicular energy is converted to longitudinal energy. The increase of the longitudinal energy at high electron energies leads to populating the loss cone with high energy electrons – a process referred to as RF-scattering or elastic pitch-angle scattering, which limits the hot electron confinement.

### 3.3 Plasma potential

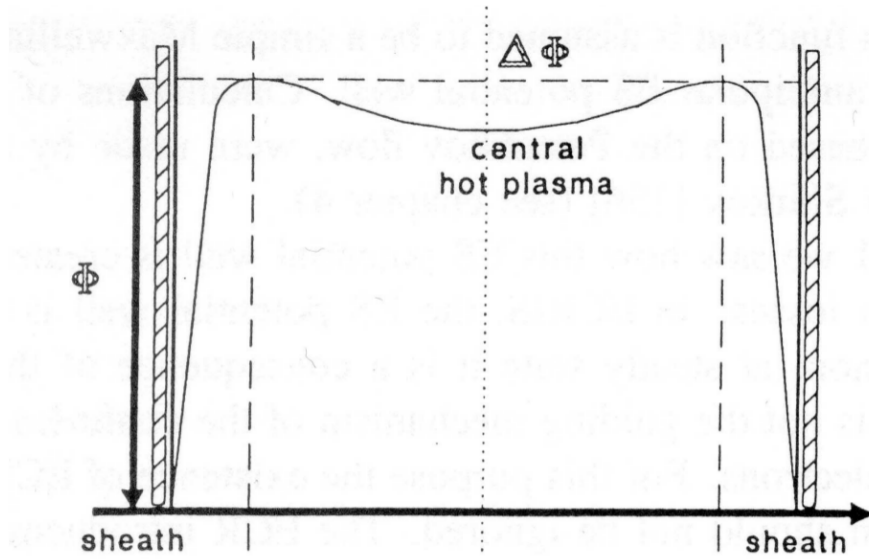


**Figure 5.** The supposed form of the plasma potential in the ECRIS. From [4].

Due to their lighter mass, electrons diffuse out of the plasma at a faster rate than ions. This creates a charge imbalance, leaving the plasma more positive than the chamber walls due to the build up of so-called plasma potential. As electrons continue to diffuse onto the chamber walls, the plasma potential grows and begins to retard the electrons, and conversely to accelerate ions, until their respective diffusion rates equilibrate. This phenomenon is termed ambipolar diffusion. The positive plasma potential thus confines the electrons, modifying the electron loss cone such that only those electrons that have an energy higher than the confining potential barrier can escape. The effect is illustrated in figure 4. The plasma sheath, illustrated in figure 5, is the region between the bulk plasma and the chamber wall, where the plasma potential and density fall due to the electric screening effect. The sheath width is a few multiples of the Debye length.

As the hot, well confined electrons accumulate in the center of the plasma – trapped within the ECR-surface – it is the cold electron population that is responsible for the build up of the plasma potential. The hot electron population causes the electron density to be slightly higher in the plasma center and it causes a dip to form in the potential profile [4, 8]. The figure 5 depicts the plasma potential profile. The depth of the well at the center is about or less than 1 V according to [14].

There is some disagreement on whether or not a dip is actually formed in the potential profile. The dip has never been directly measured in an ECRIS, but it is observed in fusion devices where ECR heating is utilized. Nevertheless, there are phenomena observed in the ECRIS plasma can be explained straightforwardly by assuming its existence: for example the effect that gas mixing has on the beam emittance and HCI production, or the HCI outpour in the 'afterglow'-regime of ECRIS operation. These are discussed in more detail in section 4.2 in conjunction with ion confinement, which is believed to depend on

the potential dip.

### 3.4 Collisions in plasma

The plasma consists of neutral atoms, ions and electrons which interact via the electric Coulomb interaction. Even neutral-neutral interactions take place via their respective electron clouds. Collisions between the plasma particles can be categorized as: (i) inelastic collisions affecting the charge state or electronic excitation of the ions, and (ii) elastic collisions affecting plasma confinement and temperatures of different plasma components.

The collision frequencies in plasmas are usually defined as an average over the supposedly Maxwell-Boltzmann-like energy distribution as

$$\nu = n \langle \sigma v \rangle \quad (25)$$

where  $n$  is the particle density,  $\sigma$  the collision cross section and  $v$  the relative speed of the colliding particles. The factor  $\langle \sigma v \rangle$  is referred to as the rate coefficient.

As it is that collisions between charged, point-like particles are mediated by the coulomb interaction over distance, the relative velocity of the interacting particles determines the quality of the interaction. In order for a collision to be ionizing, for example, the incident particle must possess sufficient kinetic energy to overcome the ionization potential of the target atom (or ion), but it must also spend sufficient amount of time in the vicinity of the target for the coulomb force to cause sufficient acceleration on the ejected electron. Thus, the cross section for charged particle collisions is heavily energy dependent.

#### 3.4.1 Collisions affecting plasma charge state distribution

The first category of collisions includes processes such as ionization, electronic excitation, charge exchange and recombination. Ionization in an ECRIS takes place stepwise from one charge state to the next<sup>3</sup>, while recombination and charge exchange processes compete with it to decrease the charge state. In the ECRIS plasma charge exchange takes place mainly between ions and neutrals, as it is that the loosely bound electron of a massive neutral is far more likely to be captured by a highly charged ion than, for example, even the valence electron of a singly charged ion, due to the rapidly diminishing cross section [15].

To estimate the cross section for ionization by electron impact the so-called Lotz formula [16] can be used:

$$\sigma_{q-1 \rightarrow q} = 4.5 \times 10^{-14} \sum_k \xi_{q-1,k} \frac{\ln(E_e/I_{qk})}{E_e I_{qk}} \text{cm}^2. \quad (26)$$

---

<sup>3</sup>Although it is possible for two (or more) electrons to be ejected in an electron-ion collision, the stepwise process is much more probable.

In the Lotz formula,  $E_e$  is the energy of the incident electron,  $I_{qk}$  the ionization potential of the  $k^{\text{th}}$  subshell of the ion and  $\xi_{q-1,k}$  is the number of electrons on the subshell  $k$ . The Lotz formula takes into account that the electron may be lost from any of the ion's subshells for which the electron energy is higher than the ionization potential.

The Lotz formula shows that the cross section depends strongly on both the incident electron energy and the ionization potential. The cross section for ionization decreases markedly as the charge state of the atom increases, while the optimum electron energy increases – both effects being due to the increasing ionization potential. This can be seen in figure 6, where the ionization cross sections for neutral argon and  $\text{Ar}^{8+}$  are shown as functions of the bombarding electron energy: While the optimum bombarding energy increases by a factor of ten, the cross section for ionization decreases by three orders of magnitude. The maximum of the cross section is reached at a bombarding energy around three times the ionization potential. Going over the optimal bombarding energy causes the cross section to decrease. This means that it's the warm electron population that is mainly responsible for ionization processes in the ECRIS plasma, and not the hot electrons with up to hundreds of keVs energy.

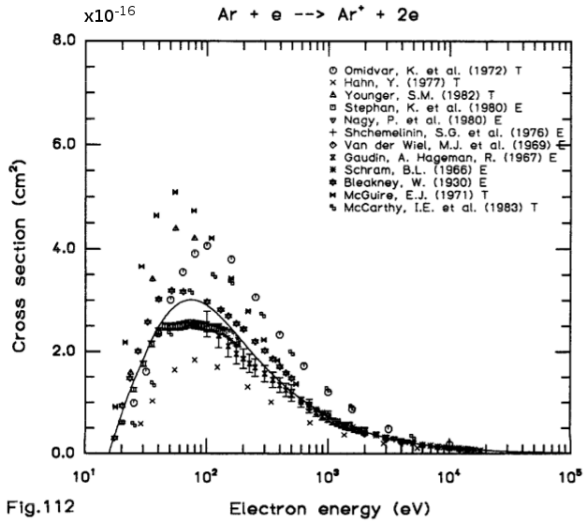


Fig.112

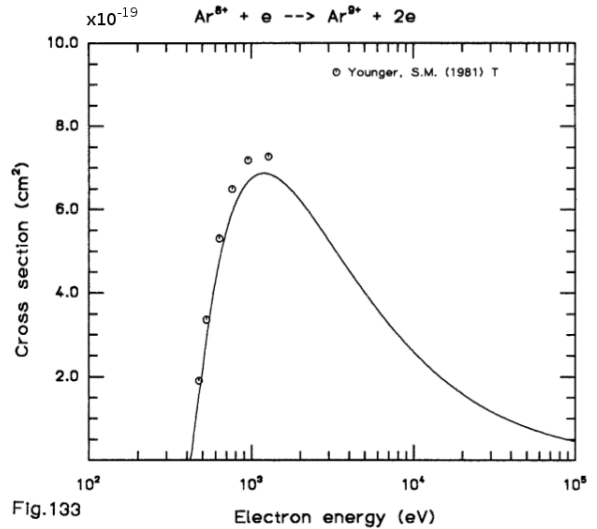


Fig.133

**Figure 6.** The electron-impact ionization cross sections for neutral argon (left) and  $\text{Ar}^{8+}$  (right). Figures from [15, and references therein].

The charge exchange cross section between an ion and a neutral atom can be estimated by [17]

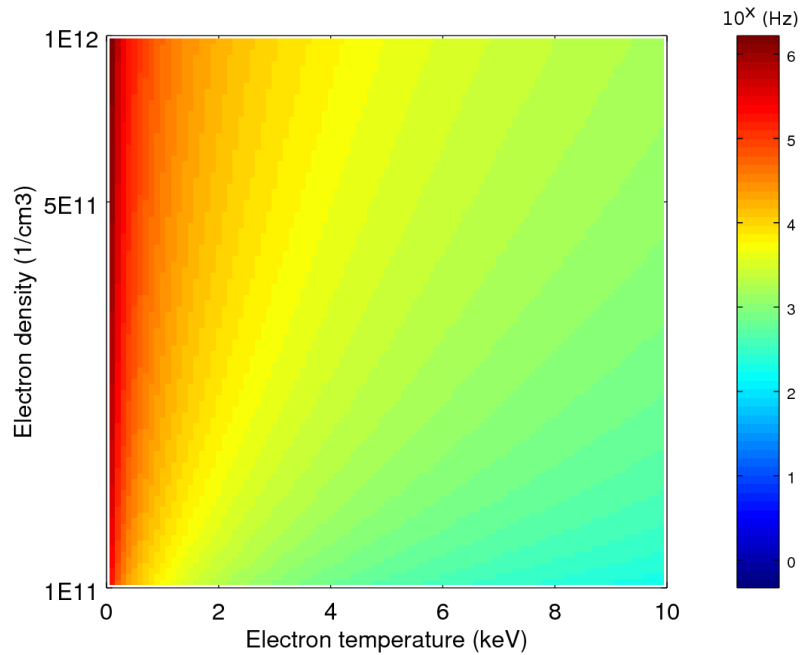
$$\sigma_{q \rightarrow q-1} = \pi a_0^2 q Z^{1/3} \left( \frac{I_0}{I} \right)^{3/2}. \quad (27)$$

Here  $a_0 \approx 0.53 \times 10^{-10} \text{m}$  and  $I_0 \approx 13.6 \text{eV}$  are the Bohr radius and Bohr energy respectively. The ionization potential  $I$  of the neutral atom corresponds to the binding energy of its outermost electron and  $Z$  to its proton number, while  $q$  is the charge state of the ion capturing the electron. From the formula it can be seen, that the probability of charge exchange increases with the charge state of the capturing ion and decreases with

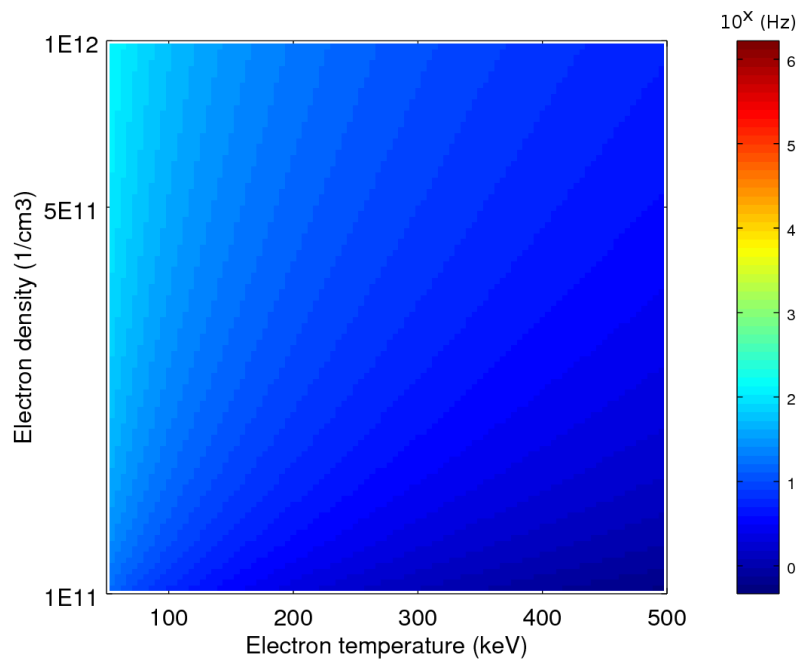
the ionization potential of the neutral.

Because the rates of ionization and charge exchange depend on the particle densities, the cross sections alone are not sufficient to compare the frequencies of these events. Nevertheless, the probability of charge exchange is significantly greater than that of ionization, and in particular, the cross section for an ion to capture an electron increases as the charge state increases – contrary to the case with ionization. Therefore, in order to produce high charge states, it is essential for the ion source to be operated in good vacuum conditions in order to minimize the charge exchange processes (i.e. to minimize the number of neutrals).

### 3.4.2 Collisions affecting plasma confinement and temperature



(a)



(b)

**Figure 7.** Electron-electron collision frequency in the ECRIS plasma according to equation (28) for electrons in the temperature range 0.1 keV – 10 keV for the cold electrons (a) and 50 keV – 500 keV for the hot electrons (b) as functions of both the temperature and electron density. Typical 14 GHz ECRIS parameters were used.

The second category of collisions in the plasma are the elastic collisions, which do not directly affect the plasma charge state distribution. This category includes non-ionizing particle-particle collisions – electron-electron and ion-ion collisions.

Because there are two or three distinct electron populations with different temperatures formed in the plasma, i.e. the electron population as a whole is not in thermal equilibrium, there is no one collision frequency that could be determined for the whole electron population. The different populations may however be considered separately[10]. The average electron-electron collision frequency is [1]

$$\langle \nu_{ee} \rangle \approx \frac{n_e e^4 \ln \Lambda}{\varepsilon_0^2 m_e^{1/2} (kT_e)^{3/2}}. \quad (28)$$

Here  $\ln \Lambda = \ln(n_e \lambda_D^3)$  is the Coulomb logarithm, which in the JYFL 14GHz ECRIS is typically around 12. Figure 7 shows the behavior of the collision frequency with respect to electron temperature and density. The electron density range  $1 \times 10^{11} \text{ cm}^{-3} - 1 \times 10^{12} \text{ cm}^{-3}$  is typical of ECRIS plasmas [10, 18]. It can be seen that the collisionality increases for higher electron densities and lower temperatures.

Assuming the electrons to oscillate about a stationary ion population, the electron-ion collision frequency [1] is given by

$$\langle \nu_{ei} \rangle = \frac{\sqrt{2} n_i q^2 e^4 \ln \Lambda}{12 \pi^{3/2} \varepsilon_0^2 m_e^{1/2} (kT_e)^{3/2}}. \quad (29)$$

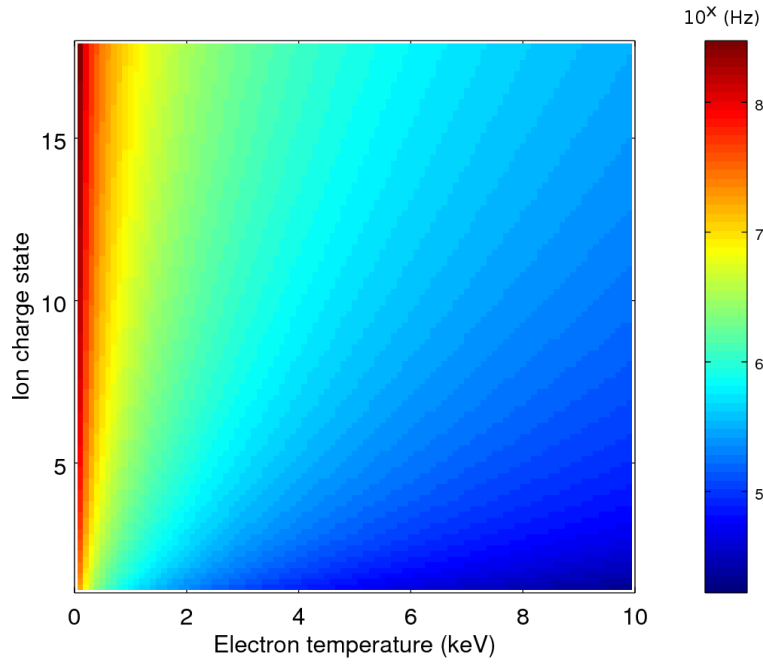
In figure 8 the electron-ion collision frequency according to equation (29) has been plotted with respect to the electron temperature (in the cold and the hot electron temperature ranges) and ion charge state for an ion density of  $n_i = 5 \times 10^{11} \text{ cm}^{-3}$ . The fast decrease of the collisionality as the electron temperature increases can be clearly seen from the figure, as well as the effect of the increasing ion charge state. For a given ion density, the difference in  $\nu_{ei}$  between the low and high charge state ions is as much as an order of magnitude due to the  $q^2$  scaling of the frequency.

The heavy, slow ions experience many collisions with each other. Their collision frequency is given by [5]

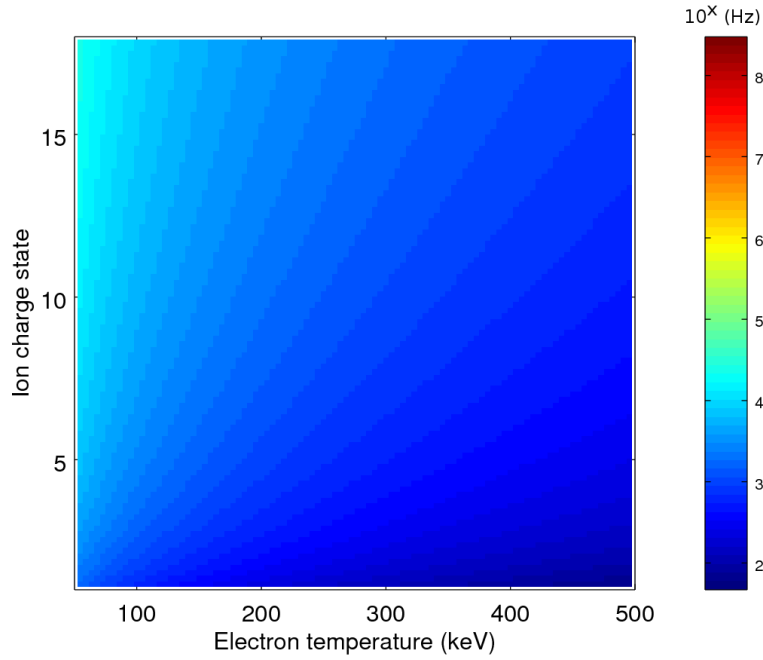
$$\nu_{ij} = \frac{1}{\tau_{ij}} \approx \frac{6.8 \times 10^{-8} \ln \Lambda_{ij} q^2}{T_i^{3/2}} \frac{q^2}{A_i} \sum_j \sqrt{A_j} \sum_q n_j^q q^2, \quad (30)$$

where  $\sum_q n_j^q q^2 \approx n_e q_{\text{eff}}$  – given approximate quasi-neutrality of the plasma. Here,  $A_i$  is the mass number of the ion  $i$  for which the collision frequency is calculated, while  $\sum_j A_j$  are the masses of the ionic species  $j$  making up the plasma. In the case of a pure plasma (single ion species only – e.g. a pure oxygen plasma) the equation simplifies, but for the purposes of this thesis the complete form is presented as copper is mixed into the buffer gas. The average time between collisions is the inverse of the collision frequency:  $\tau_{ij} = 1/\nu_{ij}$ .

In figure 9 the collision frequency of  $^{16}\text{O}^{q+}$ -ions in an  $^{16}\text{O}$  buffer plasma has been calculated, given an effective plasma charge state of  $q_{\text{eff}} = 4$ , electron density of  $n_e = 5 \times 10^{11} \text{ cm}^{-3}$  and  $\ln \Lambda_{ij} = 12$ . The figure illustrates the temperature and charge state



(a)



(b)

**Figure 8.** Electron-ion collision frequency in the ECRIS plasma according to equation (29). Frequencies plotted for different ion charge states at electron energies in the range 0 keV – 10 keV (a), and 50 keV – 500 keV (b). Note that the ion charge state only has discrete values in reality, but is shown as continuous for plotting purposes. The ion density was set to  $5 \times 10^{11} \text{cm}^{-3}$  and otherwise values typical for a 14 GHz ECRIS were used.

dependence of the collision frequency – the highest collisionality is obtained for cold, highly charged ions.

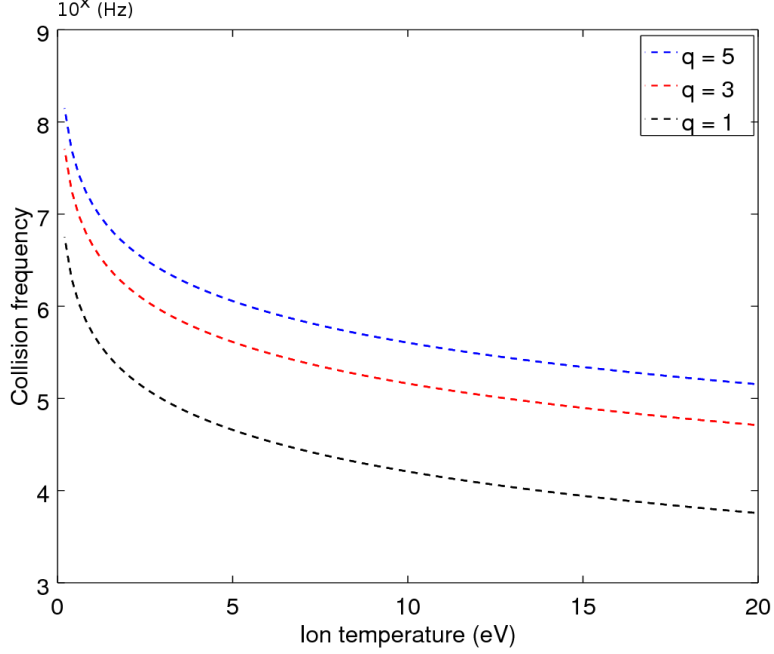


**Figure 9.** Collision frequency for  $^{16}\text{O}^{q+}-^{16}\text{O}$  collisions in a pure oxygen plasma according to equation (30). The values  $\ln \Lambda_{ij} = 12$ ,  $\sum_q n_j^q q^2 \approx n_e \cdot q_{\text{eff}}$  with  $n_e = 5 \times 10^{11} \text{cm}^{-3}$  and  $q_{\text{eff}} = 4$ , and  $j = i$  were used.

The ions can gain energy in elastic collisions between them and the electrons. The electron-ion collisional energy equipartition time (derived assuming steady state conditions in the ECRIS plasma) is [5]

$$\nu_{eq,e \rightarrow i} = \frac{1}{\tau_{eq,e \rightarrow i}} \approx \frac{3.2 \times 10^{-9} \ln \Lambda_{ei}}{T_e^{3/2}} \sum_i \frac{\sum_q n_i^q q^2}{A_i}, \quad (31)$$

where again  $\sum_q n_i^q q^2 \approx n_e q_{\text{eff}}$ .

Figure 10 shows the electron-ion equipartition time according to equation (31) for  $^4\text{He}$ ,  $^{16}\text{O}$  and  $^{40}\text{Ar}$  separately, with their effective charge states set to 1.5, 4 and 8 respectively. As the mass of the ion increases, so does the equipartition time. From the figure can be seen, that in an argon plasma the ions may gain an energy greater than 21 eV, if they remain in the plasma for more than 50 ms.

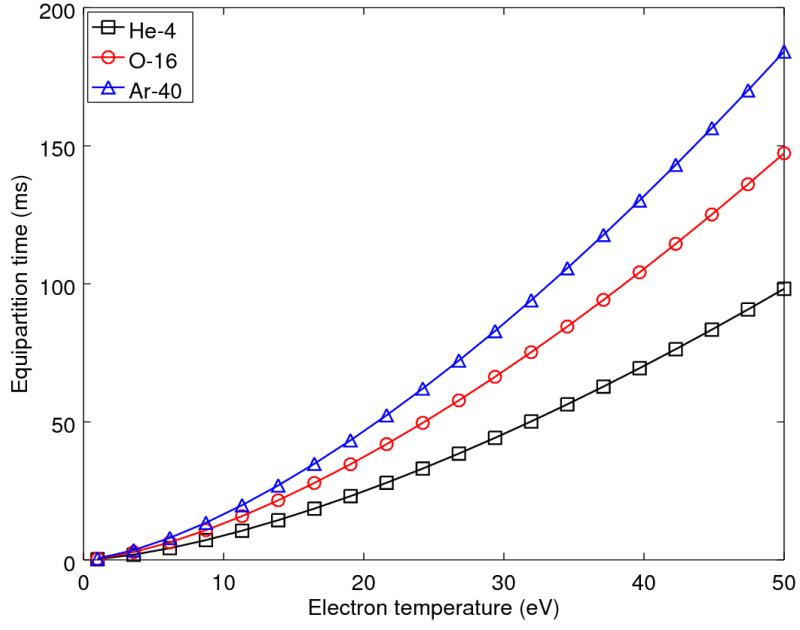


**Figure 10.** The energy equipartition time between electrons and  $^{63}\text{Cu}$  ions according to equation (31). The equipartition time is calculated for  $^4\text{He}$ ,  $^{16}\text{O}$  and  $^{40}\text{Ar}$  plasmas with their effective charge states set to 1.5, 4 and 8 respectively. The calculation is carried out for the cold electron population, whose density is taken to be half the total electron density  $n_{e,\text{cold}} = 0.5 \cdot 5 \times 10^{11} \text{cm}^{-3}$ .

## 3.5 Plasma temperatures and energy distributions

Due to the selective heating process in the ECRIS, electrons and ions have distinctly different temperatures. This is a desirable property in the ECRIS, because the high charge states of the ions are reached in collisions between them and the energetic electrons, while the low ion temperatures allow them to be confined for a long enough time for them to experience multiple such collisions.

### 3.5.1 Electron temperatures

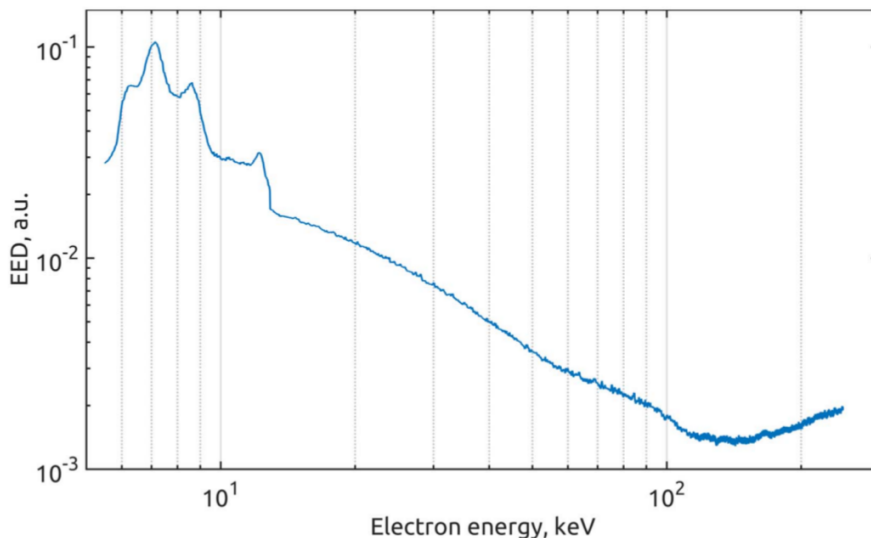


**Figure 11.** The electron energy distribution of the electrons escaping through the extraction aperture measured at 600 W microwave heating power at 14 GHz,  $3.5 \times 10^{-7}$  mbar oxygen pressure and  $B_{\min}/B_{\text{ECR}} = 0.79$ . Distribution area is normalized by the total number of electrons to equal unity. The figure is reproduced from [13].

Due to the energy dependence of the electron heating and electron loss processes, the electron velocity distribution function (EVDF), and consequently the electron energy distribution (EED), becomes very anisotropic. The resultant EVDF is believed to consist of at least three components: cold, warm and hot populations, each having a distinct temperature, and energies in the ranges 10 eV – 100 eV, 1 keV – 10 keV and 10 keV – 1000 keV respectively [14, 19, 20].

In [13] the Electron Energy Distribution (EED) of axially escaping electrons was studied in the JYFL 14 GHz ECRIS – the same source used in this work. It was found that the EED in the range 5 keV – 250 keV is strongly non-Maxwellian and that it exhibits several local maxima at energies below 20 keV. The EEDs measured were those of escaped electrons, which may differ from that of the electrons still confined. In figure 11, an example of the measured EEDs is given for a microwave power of 600 W at 14 GHz

frequency, oxygen pressure of  $3.5 \times 10^{-7}$  mbar and magnetic field setting  $B_{\min}/B_{\text{ECR}} = 0.79$ .

In [13] it was found that the EED of the escaping electrons is sensitive to the variations of the magnetic field, which affected the distribution the most at energies less than 100 keV. In figure 12 the shift of the EED with the changing magnetic field is depicted for a constant microwave power and oxygen pressure, 400 W at 14 GHz and  $3.5 \times 10^{-7}$  mbar respectively. The microwave heating power or the frequency of the wave were not found to markedly affect the distribution, at least in the ranges of 100 W – 600 W and 11 GHz – 14 GHz respectively.

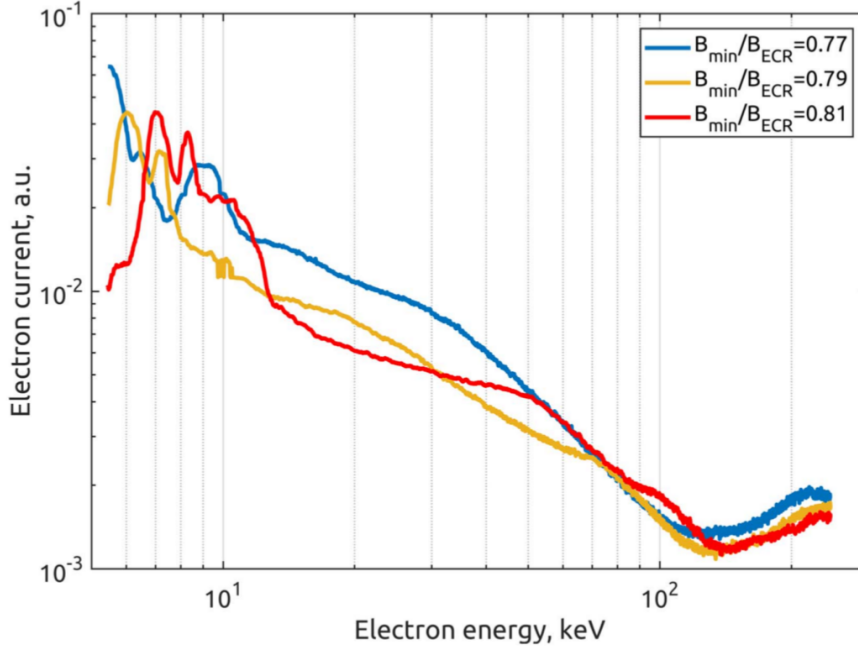


**Figure 12.** The magnetic field dependence of the electron energy distribution at constant 400 W microwave power at 14 GHz and pressure of  $3.5 \times 10^{-7}$  mbar oxygen. The distributions are unnormalized. The high energy ( $>200$  keV) electron population is only partly visible. Figure reproduced from [13].

In figure 13(a) can be seen how the number of escaping electrons decreases as the magnetic field strength is increased. Meanwhile, the average energy of escaping electrons increases, as can be seen in figure 13(b). It can be inferred that the decrease of escaping electron flux results from their better confinement due to an increase in their temperature, and the fact that the varying  $B_{\min}/B_{\text{ECR}}$  ratio causes the increment of electron losses in the radial direction to increase.

Figures 11 and 12 demonstrate, that the assumption of a Maxwellian velocity distribution is only approximately valid. The thermal electrons, with their large collision rates, are more precisely Maxwellian, but the hot electrons carry almost all of the total electron energy[5]. Therefore, mathematically simple Maxwellian and Maxwell-like distributions (such as the Druyvesteyn distribution) are used to model the electron temperature in theoretical plasma studies.

In [20] the electron temperatures in the 18 GHz MinimaFios ECRIS were studied based on the electron cyclotron emission (ECE) -and bremsstrahlung spectra, as well as the diamagnetism of the plasma. Figure 14 shows the results for ECE and bremsstrahlung measurements with respect to the microwave heating power. It can be seen, that the electron temperature increases with increasing heating power and decreasing neutral gas pressure. For heating powers higher than 50 W, however, the rate of temperature increase becomes lower and the temperature reaches its asymptotic limit at powers higher than 200 W. The increase in electron temperature cannot continue indefinitely, as the very hot electrons become confined such that their mirror point lies within the ECR surface. Thus, they no longer encounter the resonance and their heating ceases to be efficient[20]. The temperature is further limited by the increase in RF-scattering effects, which push hot electrons into the loss cone. The systematically lower electron temperatures for higher pressures are due to the increase in electron density: The same heating power is distributed to more electrons leading to lower temperature [10].

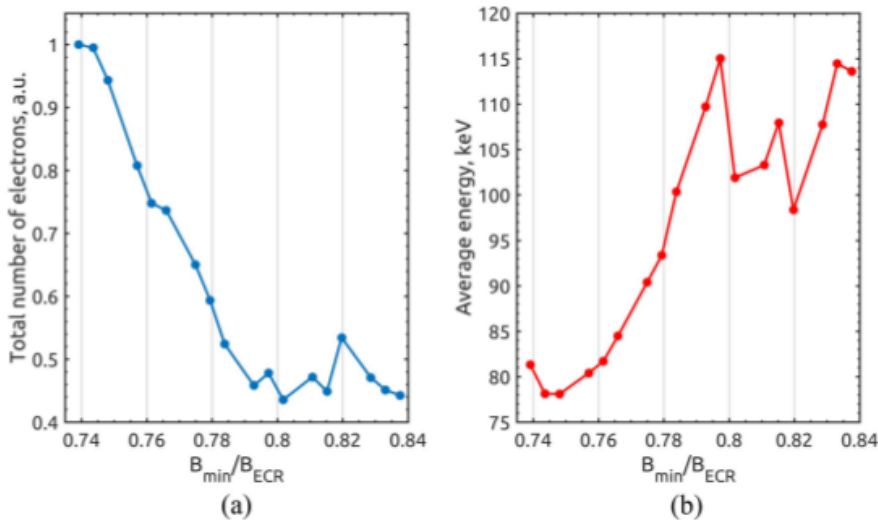


**Figure 13.** Total number of escaped electrons normalized to unity (a) and the average energy of an escaped electron (b) as functions of  $B_{\min}/B_{\text{ECR}}$ . Heating power 100 W at 14 GHz and pressure  $3.5 \times 10^{-7}$  mbar of krypton. From [13].

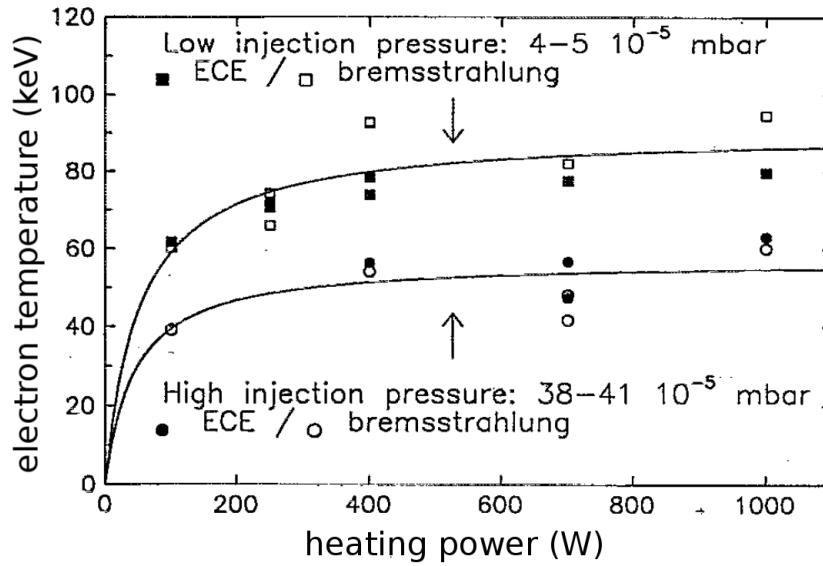


**Figure 14.** The electron temperature as a function of the microwave heating power at low and high pressures in the 18 GHz Minimafox ECRIS. From [20]

### 3.5.2 Ion temperatures

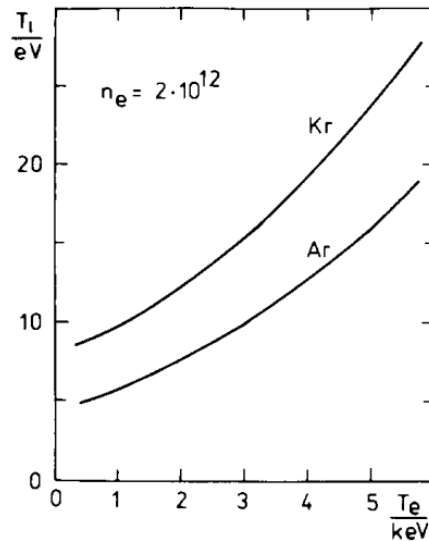


**Figure 15.** The temperatures  $T_i$  of argon and krypton ions as functions of electron temperature  $T_e$  in pure plasmas with an electron density of  $n_e = 2 \times 10^{12} \text{cm}^{-3}$ . From [18].

Ion temperatures in ECR plasmas are generally considered to be quite low – on the order of few electronvolts [5]. This is due to the low electron-ion energy equipartition rates, which lead to low power transfer between electrons and ions. The electron-ion equilibration power  $P_{ei}$  can be calculated from the ion particle losses  $\sum_i \sum_q (I_i^q/q)$ , ion

temperature  $T_i$  and fraction of ion losses ending up into the ion source extraction region  $k_L$  according to [21]

$$P_{ei} \simeq \frac{3}{2} n_e T_e \nu_{eq,e \rightarrow i} \approx \frac{3}{2} \frac{T_i}{k_L} \sum_i \sum_q \frac{I_i^q}{q}, \quad (32)$$

where the first form of the approximation is more descriptive. It indicates that the energy for the heating power is transferred to the ions at the energy-equilibration rate  $\nu_{eq,e \rightarrow i}$ .

Because the ion confinement times are typically believed to be much shorter than the energy equipartition rates, the ions cannot reach very high temperatures. Melin *et al.* give the following parameters as typical for a pure argon plasma, and particularly for the ion  $\text{Ar}^{10+}$ : Electron temperature  $T_e = 500 \text{ eV}$ , electron-ion energy equilibration rate  $\nu_{eq,e \rightarrow i} = 0.28 \text{ s}^{-1}$ , average charge  $q_{\text{eff}} = 8$ , and electron density  $n_e = 5 \times 10^{11} \text{ cm}^{-3}$ . Assuming additionally a confinement time of  $\tau = 5 \text{ ms}$ , the ion temperature calculated from the equipartition power would be

$$T_i = \frac{P_{ei}}{n_i} \cdot \tau = \frac{3 n_e}{2 n_i} T_e \nu_{eq,e \rightarrow i} \cdot \tau = \frac{3}{2} \cdot 8 \cdot 500 \text{ eV} \cdot 0.28 \text{ s}^{-1} \cdot 5 \times 10^{-3} \text{ s} = 8.4 \text{ eV}, \quad (33)$$

where  $n_e/n_i \approx 8$  based on the average charge in the plasma, and the quasi-neutrality condition. For shorter confinement times the temperature is even lower: For example, in [14] for  $\text{Ar}^{12+}$  optimization the confinement time of  $\text{Ar}^{10+}$  was estimated as  $\approx 0.8 \text{ ms}$ , which would yield a temperature  $T_i \simeq 1.3 \text{ eV}$ . In reference [22] the simulated ion confinement times for  $\text{Ar}^{5+}$  were found to be in the range  $0.2 \text{ ms} - 1 \text{ ms}$ . They also simulated the ion temperatures, and found them to be around  $0.5 \text{ eV}$ <sup>4</sup>.

Referring back to figure 10 it can be seen that for the cold electron population (temperature in the range 10 to 50 eV), the energy equipartition time ranges from 10 to 100 milliseconds. Given that the ion confinement times are generally found to be of the order of 5 ms [14, 23, 24] one would expect that the ion temperatures wouldn't exceed a few electronvolts[5]. In a numerical simulation made in reference [18], however, the ion temperatures are found to range between 5 and 10 eV, and 10 and 30 eV for pure argon and krypton plasmas respectively. Here the ions were assumed to absorb their energy from the hot electron population, which is noticeably more than the few eV typically assumed. The result of the simulation is shown in figure 15. It becomes clear that there is no common understanding of the confinement times and therefore the development of new methods, including this work, to estimate them is highly desirable.

Furthermore, due to their low energy the ions are highly collisional, and as a consequence they have high energy equilibration rates between themselves. This would imply that the ions share one temperature common to all ion species regardless of charge state [5, 6]. However, in optical and ion end loss flux measurements the ion energies have been observed to depend on charge state, and to exceed 10 and even 20 eV in quadrupole magnetic fusion device largely similar to an ECRIS [23]. The results from the Doppler

---

<sup>4</sup>The low ion temperatures are due to the assumption of their short confinement times. There is, however, an important distinction that needs to be made between the confinement time and the cumulative confinement time (see section 4.1.1). The experimentally observed high ion temperatures suggest that the cumulative confinement time should be preferred as a measure of the time an ion spends in the plasma – i.e. the time available for the ion to absorb energy from the electrons.

broadening measurements are shown in table 1. Similar results have been obtained from Doppler broadening measurements of the plasma optical spectrum with the JYFL 14 GHz ECRIS[25]. Figure 16 shows temperatures for argon ions as a function of temperature obtained by Kronholm *et al.* [25]. The values for the neutral argon, and charge states 1+ and 2+ were obtained from multiple electronic transitions, while the rest were obtained from only one transition. The temperatures were obtained from a single optical spectrum in a source tuned for Ar<sup>9+</sup> extraction. The figure shows that the ion temperatures can be in excess of 20 eV, and that there exists a charge state dependence.

Furthermore, the end loss flux measurements made in [23] provided ion temperatures 'substantially higher' than those acquired from the optical spectrum with the disagreement increasing linearly with the ion charge state. If there is a dip in the plasma potential profile (see section 3.3), then only those ions having sufficient energy to scale the potential barrier can escape the plasma, which would manifest in the ion energy distribution measured from the end loss fluxes as a shift towards higher temperatures.

**Table 1.** Oxygen ion temperatures in a 10.5 GHz (at 1 kW power) ECR-heated plasma at  $5 \times 10^{-7}$ Torr neutral pressure, as determined from the Doppler broadened emission lines. From [23].

Ion species	$T_i$ (eV)
O <sup>+</sup>	17
O <sup>2+</sup>	18
O <sup>3+</sup>	22
O <sup>4+</sup>	23

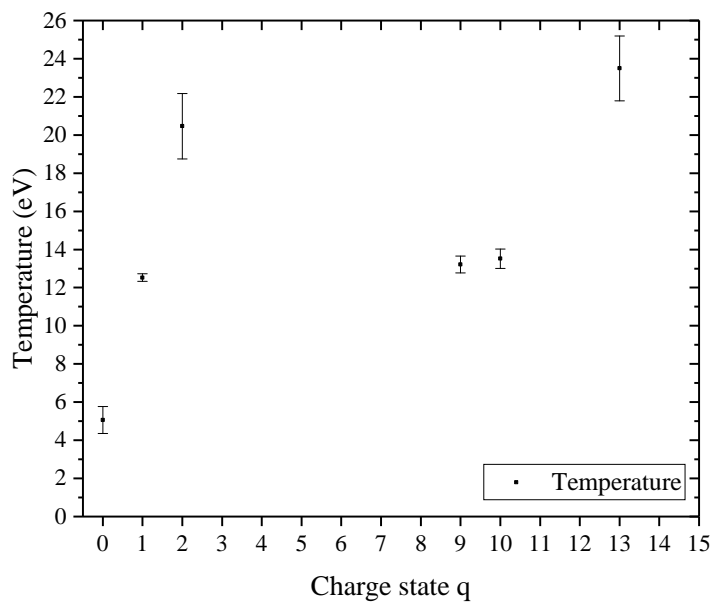


**Figure 16.** The temperatures for different charge states of argon determined from Doppler broadening measurements of the plasma optical spectrum in the JYFL 14 GHz ECRIS. The ECRIS was operated at 350 W heating power,  $B_{\min}/B_{\text{ECR}} = 0.70$  at  $2.0 \times 10^{-7}$ mbar argon pressure. Figure from [25].

## 4 Production of highly charged ions in the ECRIS

The ECRIS produces highly charged ions in stepwise electron impact ionization processes. In order to produce HCIs it is necessary for an ion to undergo multiple collisions with electrons. Thus, long ion confinement times are a requisite for HCI production. As the ion's charge state increases, the ionization potential – the energy required for further ionization – also increases. As such, an adequate density of high energy electrons is necessary for HCI production. The criterion for ionization from charge state  $q$  to  $q + 1$  is [4]

$$n_e \tau_i^q \geq \left[ \langle \sigma v_e \rangle_{q \rightarrow q+1}^{ion} \right]^{-1}, \quad (34)$$

where the product of the electron density  $n_e$  and the confinement time  $\tau_i^q$  for ions of species  $i$  and charge state  $q$  is the so-called 'ionization factor' [6]. The term  $\langle \sigma v \rangle_{q \rightarrow q+1}^{ion}$  is the rate coefficient for ionization to higher charge state. Increased ion confinement times allow the ions to undergo multiple ionizing collisions with the electrons, which improves the production of HCIs.

Because an ion can only be further ionized by an electron having a kinetic energy higher than the ionization potential, the plasma's Charge State Distribution (CSD) – particularly its average charge state – is dependent on the electron energies. Competing with the ionization process is charge exchange, which lowers the average charge state in the plasma as ions capture electrons from neutral gas atoms. In order for charge exchange processes to be minimized the neutral gas pressure must be kept sufficiently low, so that the number densities of neutral gas atoms stay small. This means that the ion source must be operated in good vacuum conditions. The so-called balance equation is employed to describe the densities of different charge states.

As the ions are determined to be electrostatically rather than magnetically confined, the key to ion confinement is in minimizing their energy – contrary to the case of the electrons. The ECRIS selectively heats the electrons, but the ions do absorb energy from the cold electron population in collisions. Ion cooling can be achieved via 'gas mixing' [26] where a lighter element is introduced into the plasma. As a result, the lighter element depletes the heavier of its kinetic energy in collisions between the two species. The ions may also be heated by a so-called ion sound wave in the plasma. Turbulences and other plasma instabilities also cause the ion temperatures to increase, but in operating conditions the ion source parameters are tuned to minimize the effects of these phenomena.

When operating the ECRIS, the operator must find a balance between the ion loss and confinement by 'tuning' the ion source parameters. While HCI production requires the ions to be well confined, most applications require also that the output ion beam is sufficiently intense. In essence, the operator must simultaneously optimize the balance between ion confinement and losses.

## 4.1 Balance equation of the ion densities

The time evolution  $dn_i^q/dt$  of the density of ions of charge  $q$  and species  $i$  can be described by the balance equation[5]

$$\begin{aligned} \frac{dn_i^q}{dt} = & + n_e n_i^{q-1} \langle \sigma v \rangle_{q-1 \rightarrow q}^{ion} - n_e n_i^q \langle \sigma v \rangle_{q \rightarrow q+1}^{ion} \\ & + n_0 n_i^{q+1} \langle \sigma v \rangle_{q+1 \rightarrow q}^{cx} - n_0 n_i^q \langle \sigma v \rangle_{q \rightarrow q-1}^{cx} \\ & - \frac{n_i^q}{\tau_i^q}. \end{aligned} \quad (35)$$

On the right hand side of the equation, the first two terms describe electron impact ionization processes. The first term increases the number density of ions of charge  $q$  by ionizing particles from a lower charge state  $q-1$  to state  $q$ , and the second term decreases it by ionization from  $q$  to a higher state  $q+1$ . The third and fourth terms describe the charge exchange processes between ions and neutrals, where the ion captures an electron from the neutral atom's outer orbital. The third term increases  $n_i^q$  via charge exchange from a higher charge state  $q+1$  to the state  $q$ , and the fourth term decreases  $n_i^q$  via charge exchange to a lower state  $q-1$ . The final term is key for the operation of the ECRIS, as it describes diffusion and transport losses of ions. It determines the rate at which ions are lost to the plasma chamber walls and/or extracted from the ion source, and defines the confinement time  $\tau_i^q$ .

### 4.1.1 Confinement time

The ion may be lost either along the plasma chamber axis towards the ends of the magnetic mirror, or along the radial direction to the plasma chamber walls. As such, the true confinement time of a particle is the combination of the axial and radial confinement times  $\tau_{\parallel}$  and  $\tau_{\perp}$  according to the equation [24]

$$\tau = \left( \frac{1}{\tau_{\parallel}} + \frac{1}{\tau_{\perp}} \right)^{-1}. \quad (36)$$

It should be noted, that the confinement time is not an absolute time limit for the ion confinement – nor is it an average. In equilibrium conditions, populations of ions having different charge states are established such that their number densities are constant<sup>5</sup>. The confinement time tracks the characteristic time for a particle to be lost from one of these populations. This is in analogy with radioactive decay, as a radionuclide can have a half life that is in fact very short, but might not decay until several half lives later. In the same way, the confinement time is a measure of probability for an ion to be expelled from the plasma.

To put it another way: In the plasma, a particle starts out its life cycle when it is injected as a neutral particle. It then changes its charge state in ionization and charge exchange

---

<sup>5</sup>The number densities of each charge state are determined according to the balance equation, depending on the rate coefficients for ionization and charge exchange, neutral densities and, of course, the confinement time.

reactions, until it is expelled at charge state  $q$ . As the particle leaps from charge state to another, there is a probability – characterized by the confinement time – for the particle to be expelled as an ion at charge state  $q$ . On the other hand, when the ion is injected into the plasma, there is a probability – characterized by the cumulative confinement time – for it to be expelled later as an ion at charge state  $q$ . This distinction is critically important, as it is the cumulative confinement time which is a measure of the time that a specific particle actually dwells in the plasma. Meanwhile, the confinement time determines the rate at which ions of charge  $q$  are lost from the plasma volume.

## 4.2 Ion confinement

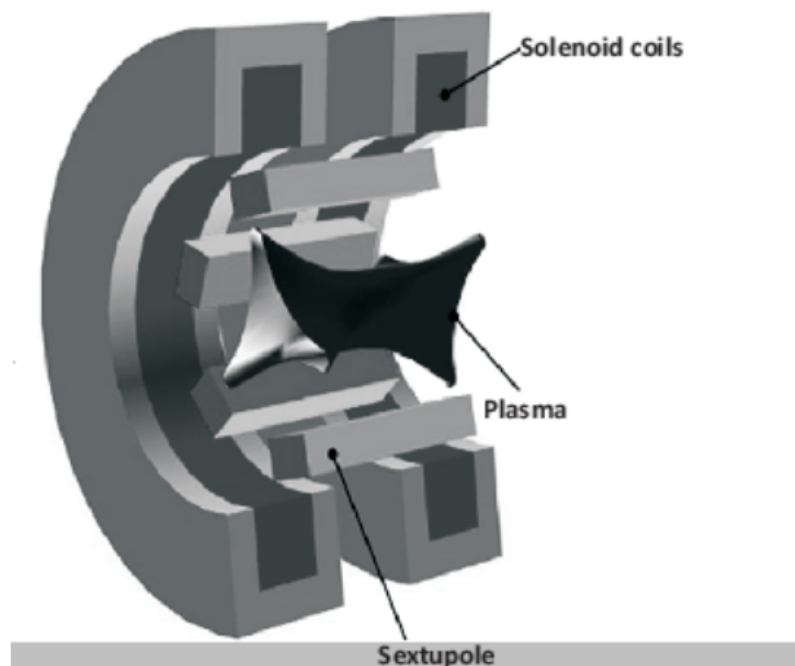


**Figure 17.** A schematic view of an ECRIS plasma contained in the minimum-B field of a sextupole-solenoid configuration similar to that of the JYFL 14 GHz ECRIS. From [27].

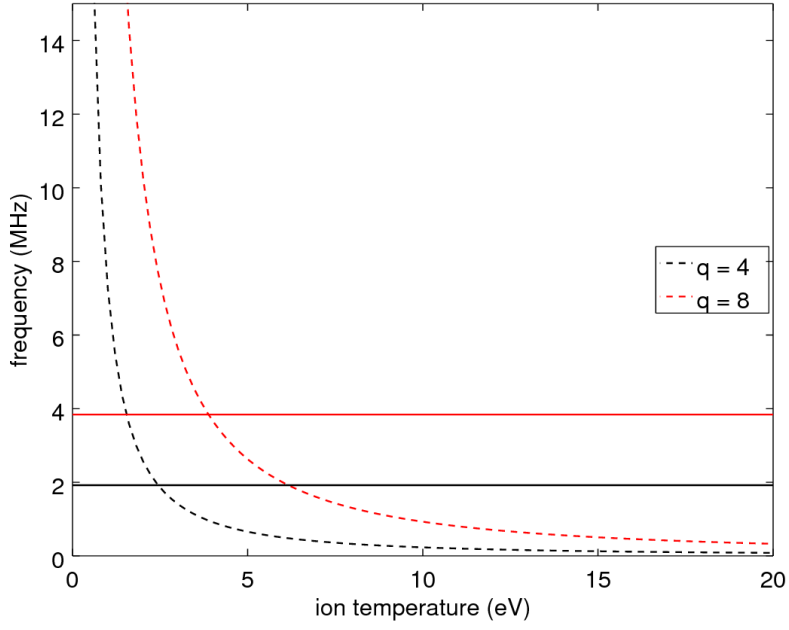
Due to their much higher mass, and the fact that in the ECRIS electrons are selectively heated, the ions remain cold and slow moving. They are thus highly collisional, which breaks their magnetic confinement as the required gyromotion is disturbed by collisions. Without proper orbits the ions do not feel the restoring force as they drift towards the increasing magnetic field. Thus, ion confinement is treated with diffusion models.

As an example, let's compare gyrofrequencies and collision frequencies for certain copper and oxygen ions. For the calculations, typical values for an oxygen plasma in a 14 GHz ECRIS were used:  $\ln \Lambda = 12$ ,  $n_e = 5 \times 10^{11} \text{cm}^{-3}$ , and  $q_{\text{eff}} = 4.5$ . Since the amount of copper sputtered into the plasma is small, the plasma can (to some accuracy) be treated as consisting of pure oxygen, and the summation over the different buffer gas species  $j$  in

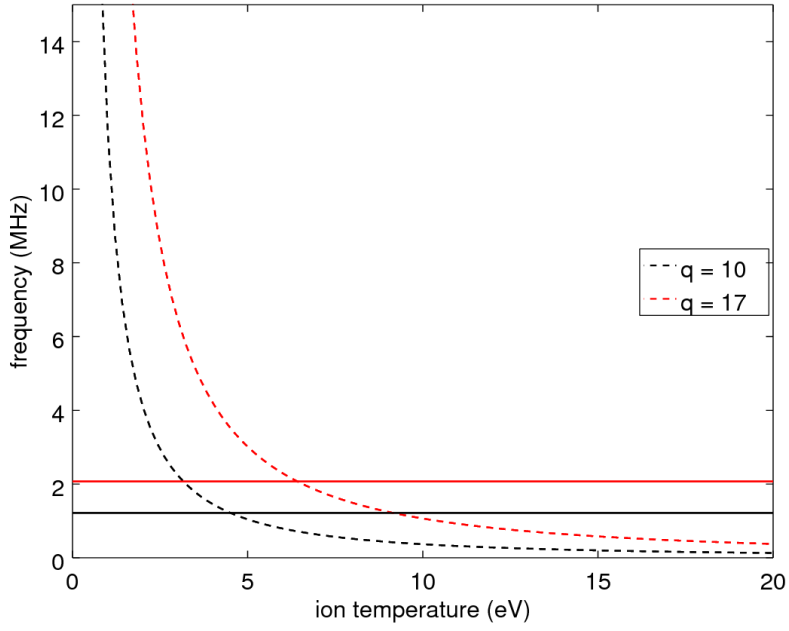
equation (30) can be omitted, and the collision frequency calculated by using  $A_i = 63$  for copper and  $A_j = 16$  for oxygen. The collision frequency of two charge states of copper is plotted in figure 18. The solid lines in the figure correspond to the ion's gyrofrequency about  $B = 0.5 \text{ T}$  – corresponding to  $B_{\text{ECR}}$  for 14 GHz microwaves. In order for the ion to be considered magnetically confined, its collision frequency must lie substantially below this line. For example The collision frequency of  $^{63}\text{Cu}^{17+}$  in an oxygen plasma at ion temperature of 10 eV for example is about 1.1 MHz. Meanwhile its gyrofrequency at  $B = 0.5 \text{ T}$  is 2.1 MHz, which means that the ion cannot be truly magnetically confined as collisions prevent it from completing multiple orbits about the magnetic field lines inside the resonance zone  $B < B_{\text{ECR}}$ .

Light ions on the other hand may be magnetically confined – provided that they reach high enough temperatures. For example, at the magnetic field strength of  $B = 0.5 \text{ T}$  the orbital frequency for an  $^{16}\text{O}^{4+}$  ion is about 1.9 MHz according to equation (21). Meanwhile, its ion-ion collision frequency in an oxygen plasma is around 230 kHz for 10 eV, as can be seen in figure 18 (a). Thus, the oxygen ions complete (statistically) multiple periods about the magnetic field lines before experiencing a collision, which means that they do feel the restoring force of the magnetic field gradient. Such mirror trapped low charge ions are lost through velocity space diffusion via collisions like the electrons [24].

Two main processes determine ion losses in ECRIS plasma [6]: firstly the classical charged particle motion in electromagnetic fields and elastic scattering detailed in section 3.4.2, and secondly turbulent phenomena and plasma instabilities. The effects of the second category are – as a rule – stronger, and they cause the Charge State Distribution (CSD) of the plasma and the HCI output of the source to worsen[28]. The design of the ECRIS magnetic field is such that it minimizes the effects of these turbulences and instabilities. Nevertheless, a proper 'tuning' of the source parameters is always necessary when operating the ECRIS. When considering ECRIS plasmas, it can then be supposed that a proper tuning has been made and that the plasma is stable with respect to these phenomena. In practice this means operating the ion source at magnetic field strengths below the threshold  $B_{\text{min}}/B_{\text{ECR}}$ -ratio corresponding to the transition from stable to unstable regime.



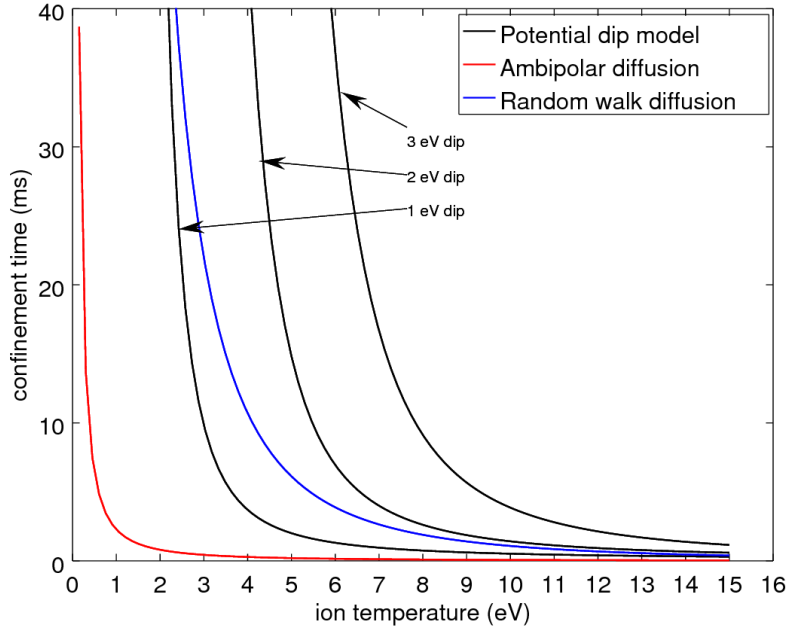
(a)



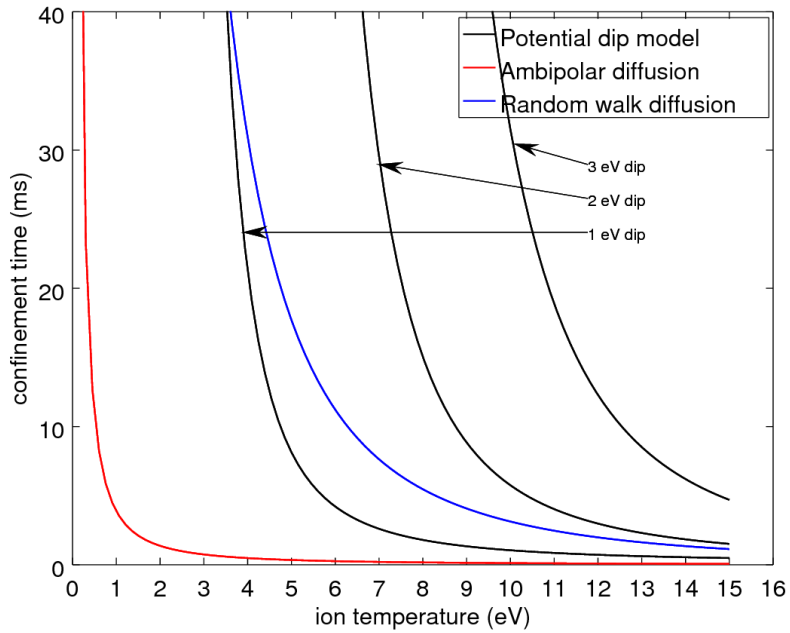
(b)

**Figure 18.** Ion-ion collision frequencies according to equation (30) for two different charge states of  $^{16}\text{O}$  (a) and  $^{63}\text{Cu}$  (b) in oxygen plasma as a function of ion temperature. The gyrofrequencies according to equation (21) for the ions about  $B_{\text{ECR}} = 0.5 \text{ T}$  are plotted as solid lines. In order for the ion to be magnetically confined, its collision frequency must lie significantly below this line. Typical parameters for a 14 GHz ECRIS were used for the calculations:  $q_{\text{eff}} = 4.5$ ,  $n_e = 5 \times 10^{11} \text{ cm}^{-3}$ , and  $\ln \Lambda = 12$ .

### 4.2.1 Diffusion models



(a)



(b)

**Figure 19.** The confinement times predicted by equations (37), (38), and (39) as a function of ion temperature for  $^{63}\text{Cu}^{10+}$  (a) and  $^{63}\text{Cu}^{17+}$  (b) in a plasma having  $q_{\text{eff}} = 4.5$  (typical for an oxygen plasma),  $\ln \Lambda = 12$ ,  $L = 15$  cm,  $n_e = 5 \times 10^{11} \text{cm}^{-3}$ ,  $E = 1$  V/cm,  $R = 4$ , and three different values of  $\Delta\phi$ .

The following diffusion models have been suggested to describe the ion confinement in the ECRIS. The confinement times for both the ambipolar -and random walk diffusion models are calculated axially, over the half-length  $L$  of the plasma.

**The potential dip model:** It was suggested by Pastukhov [8] that the ions are electrostatically confined in a potential dip which forms in the plasma potential profile as a consequence of the hot electron population, which is known to accumulate at the plasma center in the minimum-B ECRIS. The potential dip model leads to the following estimation for the confinement time [29]

$$\tau_{\text{conf}} = R \frac{\pi^{1/2} L}{v_T} \exp\left(\frac{|qe\Delta\phi|}{kT_i}\right) \quad (37)$$

Here  $R$  is the magnetic mirror ratio,  $L$  the half-length of plasma and  $v_T = \sqrt{2kT_i/m_i}$  the thermal velocity of the ions. The exponential dependence on charge state in this model can be understood by considering the ion temperatures. It is usually assumed that due to the large ion-ion collision frequency, all ions share the same temperature  $T$  regardless of their charge. Furthermore, their temperature is Boltzmann-distributed, which means that as the ion charge state increases the fraction of ions having an energy in excess of the confining potential barrier decreases exponentially, and consequently the confinement time exponentially increases. This effect of the increasing barrier height for higher charge states can be seen in figure 20.

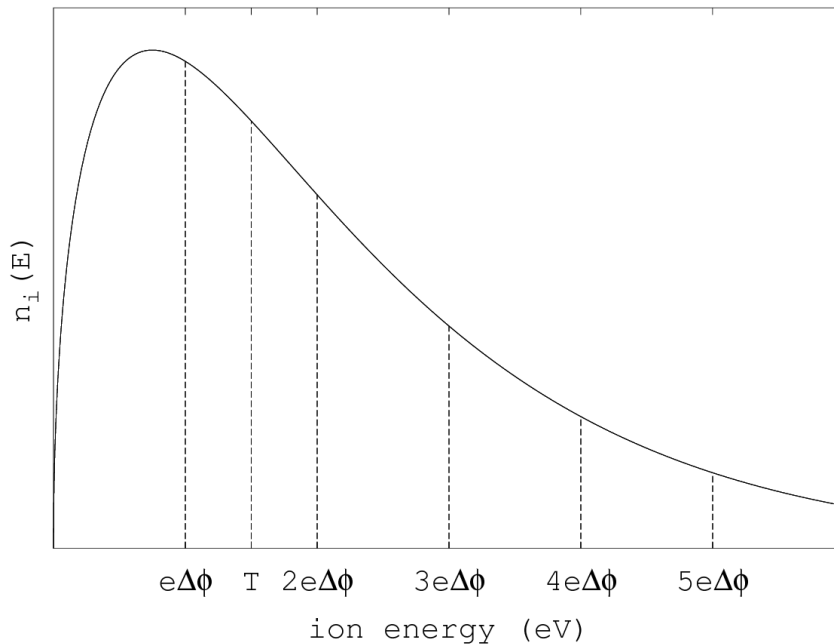


**Figure 20.** A Boltzmann-energy distribution for ions having temperature  $T$ , and the values of the potential barriers for ions of charge state  $q = 1, 2, 3, 4, 5$  in a potential well having a depth  $\Delta\phi$ .

**The ambipolar diffusion model:** The positive plasma potential creates an electric field, which causes the ions to accelerate out of the plasma. This ambipolar electric

field effect leads to a confinement time of the form[14]

$$\tau_{\text{conf}} = 7.1 \times 10^{-20} L q \ln \Lambda \sqrt{A_i} \frac{n_e q_{\text{eff}}}{T_i^{3/2} E} \quad (38)$$

Units:  $\tau = \text{s}$ ;  $L = \text{cm}$ ;  $n_e = \text{cm}^{-3}$ ;  $T_i = \text{eV}$ ;  $E = \text{V/cm}$ . This equation does not take into account ion losses in the radial direction, and only considers the ambipolar diffusion towards the injection and extraction ends of the plasma chamber.

**Random walk diffusion:** The collisions the ions experience between themselves leads to stochastic diffusion towards regions of lower plasma density. This so called random walk diffusion due to thermal motion yields a confinement time of the form[14]

$$\tau_{\text{conf}} = 7.1 \times 10^{-20} L^2 q^2 \ln \Lambda \sqrt{A_i} \frac{n_e q_{\text{eff}}}{T_i^{5/2}} \quad (39)$$

with the same units as in equation (38).

Based on these models, the following can be said about ion confinement[6]:

1. The confinement time increases with ion charge state.
2. Because the highly charged ions are better confined and remain in the plasma while the low charge states are expelled, the CSD of the plasma has a higher average charge the extracted beam. This deduction is also supported by the 'afterglow' effect, which is touched upon later.
3. Ion cooling causes the confinement times – and consequently the average charge – to increase.

It is most likely, that all of these processes described by the models above contribute to the total ion confinement time, and their significance depends on the ion source parameters. A linear dependence of the confinement time with respect to the ion charge state is usually observed, which would conform to the ambipolar diffusion model [14, 24]. However, assuming that the ion temperature scales with the ion charge state, the random walk diffusion model could also provide the correct linear dependence[10]. A charge state dependence of the ion temperature has indeed been measured, as was mentioned in section 3.5.2.

Figure 19 shows predictions of the confinement time based on the different diffusion models at typical 14 GHz ECRIS operating parameters, and three different potential dip depths  $\Delta\phi$ . The exponential dependence of the confinement time on the ion charge in the potential dip model would provide very long confinement times even for small dip depths, and as can be seen from the figure the confinement time reacts strongly to changes in the dip depth. Then again, multiple experimental observations are parsimoniously explicable by assuming the existence of a dip in the plasma potential profile. The grounds for believing that a potential dip forms are indirect: For example, it has been found that Ion Cyclotron Resonance Heating (ICRH) increases HCI currents, and causes otherwise hollow beam profiles to turn uniform, which suggests that the energy imbued to the ions 'boils' the ions out of the trap[24]. Furthermore, the increased HCI production in the 'afterglow' operation mode (see section 4.3), as well as beam emittance measurements

support the model. Again, a scaling of the ion temperature with the charge state could suppress the exponential increase in the confinement times, and a charge dependence of the temperature has been observed (see section 3.5). In the following are descriptions for how ICRH experiments and emittance measurements imply the existence of the dip.

**Potential dip and ICRH:** in [24], the effect of ion cyclotron resonance heating (ICRH) on the ion confinement was studied. In addition to the usual electron heating, the ions were heated by a 1.4 MHz frequency microwave at 2 kW power. The effect of ICRH is shown in figure 21, where the ion fluxes into the extraction end of the Constance B quadrupole mirror<sup>6</sup> are shown as function of the radial distance from the extraction aperture. It was found that ICRH causes the end loss flux profiles of the ions to peak at the center of the magnetic midplane, whereas without ICRH the flux profile has a local minimum at the center. Additionally, it can be seen from the figure that HCI currents decrease as a consequence of ICRH, which implies shortened confinement times. In other words: the heating of ions causes an otherwise hollow radial profile of the ion flux to become uniform – the ICRH boils the highly charged ions created in the plasma center out of the central trap.

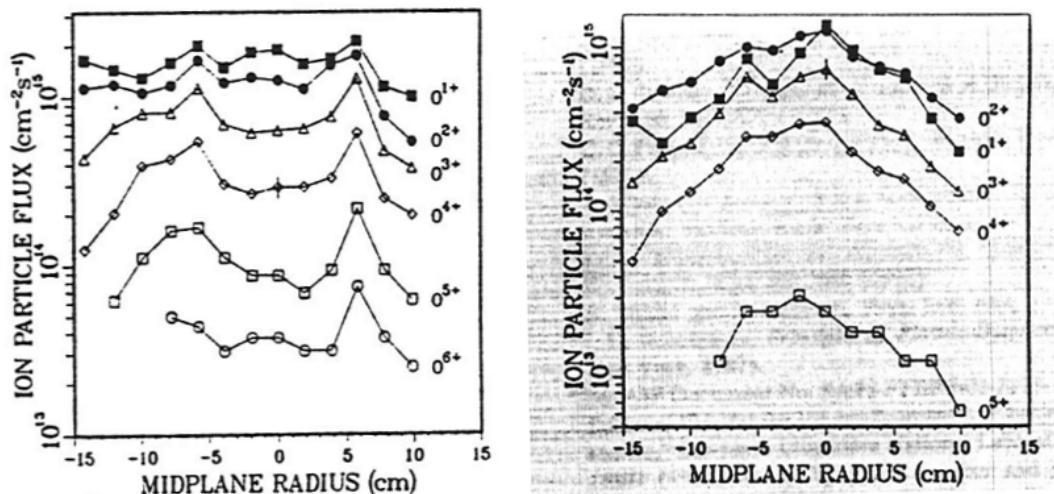


**Figure 21.** Ion end loss fluxes in the magnetic midplane without ICRH (left) and during 2 kW ICRH (right) in a 1 kW at 10.5 GHz ECR-heated  $5 \times 10^{-7}$  Torr oxygen plasma. From [24].

**Potential dip and beam emittance:** Emittance measurements also would imply that there is a potential dip component to the ion confinement in an ECRIS. In figure 22 the emittance of an  $O^{6+}$  ion beam has been plotted with respect to the proportional partial pressure of helium added as mixing gas. It can be seen, that upon adding a small amount of helium, the beam emittance decreases very slightly or remains constant until it begins to increase as the amount of added gas increases more

<sup>6</sup>In the Constance B, the radial confinement is achieved using a magnetic quadrupole instead of a hexapole configuration as in the JYFL 14 GHz ECRIS. Using a quadrupole field is beneficial for radial confinement, but it is not well suited for ion beam production, because it worsens the extraction properties of the source[10].

substantially. The increase in emittance towards the end is probably due to an increase in total pressure, which affects the ion beam momentum spread[30].

Given that adding a lighter mixing gas should decrease the ion temperatures in the plasma (see section 4.4), one would expect the momentum spread of the beam to decrease as helium is added. However, according to the potential dip model any ion that escapes from the electrostatic trap must have an energy in excess of the potential barrier. Therefore, even though the ion temperature decreases, the energies of the escaped ions won't change substantially, and the emittance remains constant<sup>7</sup>.

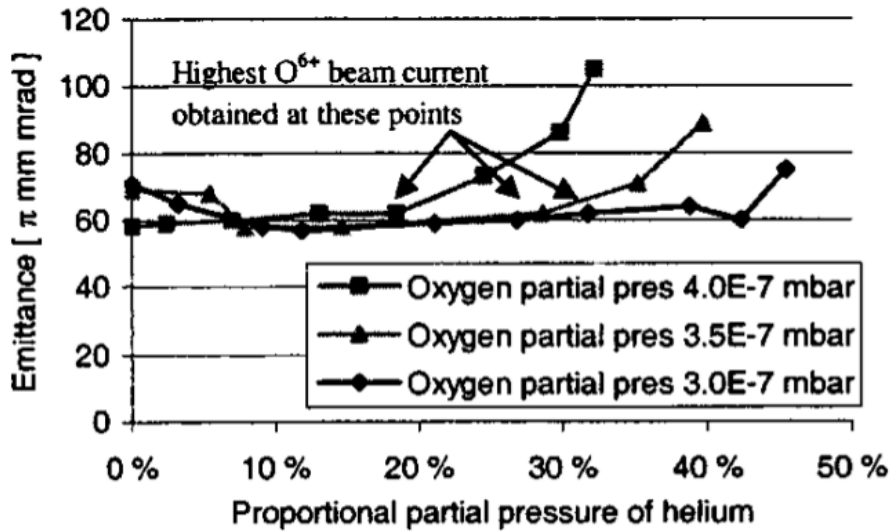


**Figure 22.** The emittance of an  $O^{6+}$  ion beam in the JYFL 6.4 GHz ECRIS as a function of proportional partial pressure of added helium mixing gas. From [30].

In [14], however, the confinement times were estimated based on the ionic densities and axial end loss fluxes, and the linear dependence on the charge, predicted by the ambipolar diffusion model, was observed. These confinement times are shown in figure 23. Here unlike with Petty *et al.* the flux distribution in the midplane was not taken into account, however. It would appear that in the magnetic midplane the confinement is influenced more by the potential dip model, while outside of the potential trap in the outside regions of the plasma, the ambipolar diffusion of caused by the plasma potential is more dominant. This makes sense, as outside of the potential dip region the effect of the plasma potential is to eject the ions rather than to confine them.

<sup>7</sup>Due to the nonlinear nature of the balance equation, the beam intensity will not necessarily change by much either. Although the percentage of ions having enough energy to escape the trap decreases with temperature, the number densities of especially the high charge states also increase as a consequence of their lengthened confinement times.

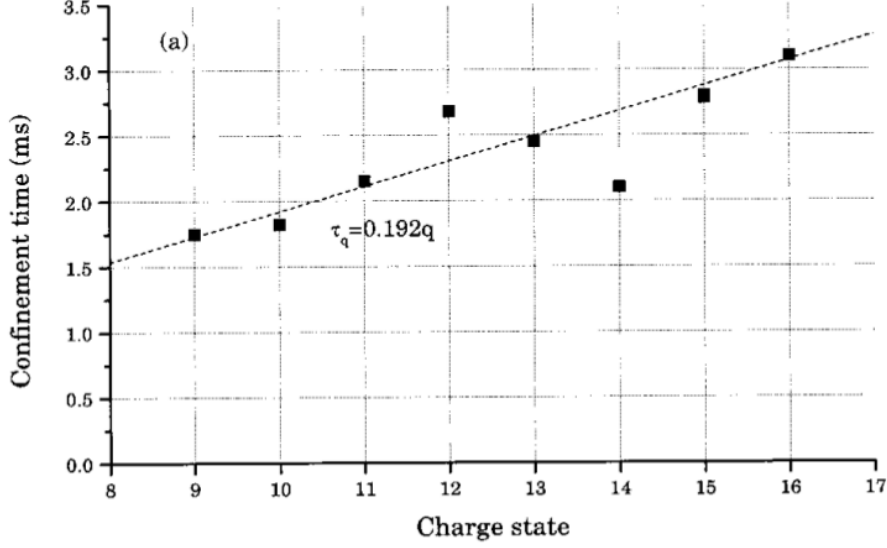


**Figure 23.** Confinement times estimated for argon ions at 1100 W heating power and Ar<sup>16+</sup> optimization. From [14].

#### 4.2.2 Spatial distribution of ions

It has been observed both directly and indirectly, as well as through numerical models, that the ions have a charge state dependent spatial distribution in the plasma volume. The highly charged ions are created (and confined) near the plasma center, while the lower charges are distributed more towards the edges – see figure 24. This distribution conforms to the potential dip model, as the dip would be formed in the center region of the plasma where the hot electron population is amassed. The spatial distribution is deduced from:

**Emittance measurements:** The (normalized) emittance due to ion temperature is described by [31]

$$\epsilon_{x,\text{rms},n}^{\text{temp}} = 0.0164r\sqrt{\frac{kT_i}{M}}, \quad (40)$$

where  $r$  is the radius of the extraction aperture in mm,  $kT_i$  is the ion temperature in eV and  $M$  is the ion mass in amu. Meanwhile, the minimum-B field configuration causes an additional rotation to the extracted ion beam. The rotation adds a component of emittance, which follows the equation [32]

$$\epsilon_{x,\text{rms},n}^{\text{mag}} = 0.0402r^2\frac{Bq}{M}, \quad (41)$$

where  $B$  is the magnetic field at ion source extraction (the origin of the beam) and  $q$  is the ion charge state. The emittance of an ion beam should increase with the ion charge state, as per equation (41). It is, however, observed that the emittance decreases for higher charges[33]. This is explicable, if we suppose that the higher charge state ions are confined in the plasma center. Then the axial electrostatic

confinement would act as a kind of collimator for the HCI currents, by effectively reducing the emittance by decreasing the parameter  $r$  in equations (40) and (41).

**Direct measurements:** The charge state distribution at the plasma electrode aperture has been directly measured by means of a 3D-movable puller electrode[34, 35]. The puller's aperture diameter was reduced to provide better resolution, and the plasma electrode aperture area was scanned by moving the puller. The ion beam extracted through each 'pixel' of the plasma electrode aperture was separated according to the charge to mass ratio, yielding the CSD at the aperture. The high charge states were found to be extracted only through the center area of the aperture, while the lower charges had a spatial spread.

**Numerical models:** The figure 24 shows spatial charge state distributions for argon ions in the transversal plane of the ion source, based on a particle-in-cell code designed to model ion dynamics in the ECRIS plasma[11]. The particle trajectories for different charge states were also calculated, and are shown in figure 25. The hollow profile traced by the  $\text{Ar}^{1+}$  trajectories, in contrast to the  $\text{Ar}^{8+}$  ions, is due to the fact that the low charge states ending up in the plasma center region get ionized to higher states.

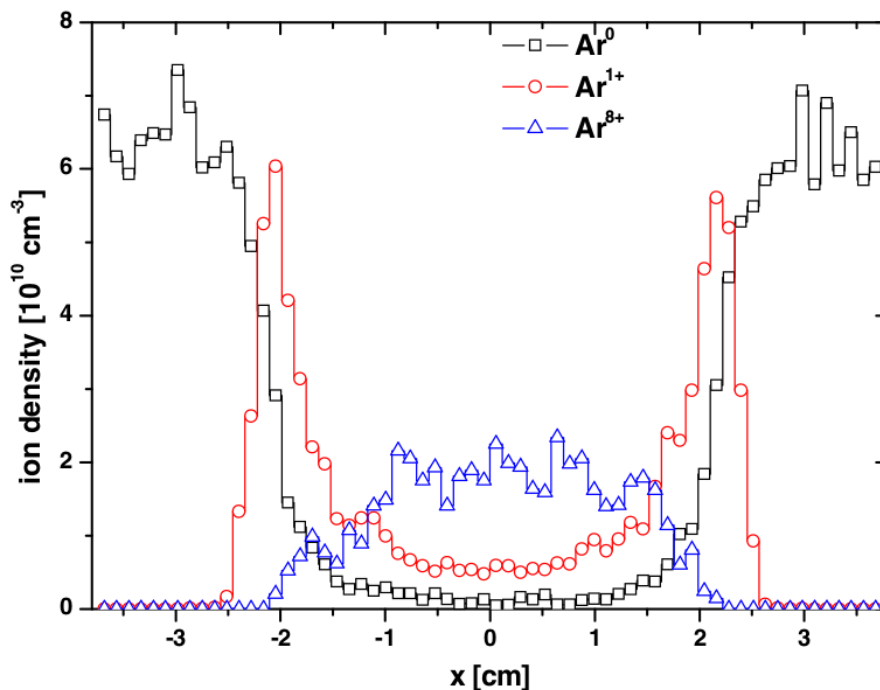


**Figure 24.** The number densities of different argon charge states as a function of the radius in the transversal plane near the  $B_{\min}$  region of the KVI AECRIS. From [11].

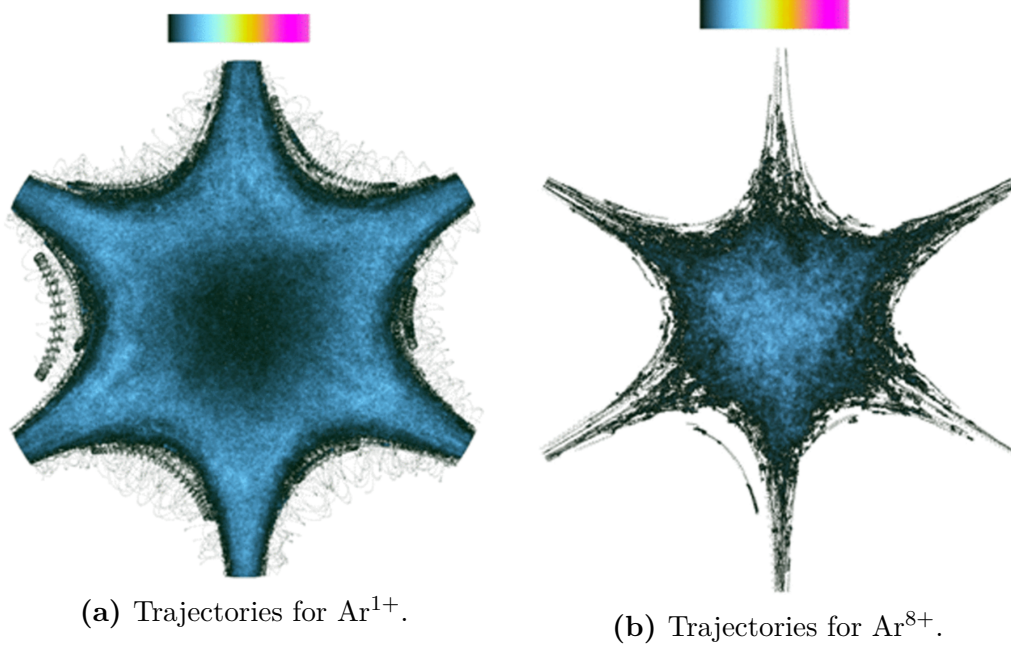


**Figure 25.** Argon ion trajectories in the transversal plane of the KVI AECRIS, nearby the  $B_{\min}$  region along the source longitudinal axis. From [11].

**Plasma electrode collar measurements:** In [32] the plasma electrode was fitted with a cylindrical collar, which extruded inwards from the plasma electrode (see figure 26). The collar limited the plasma flow in the radial direction, and any extracted ion current had to propagate along the collar, which thus acted as a kind of a collimator. The length of the collar was varied from 5 mm to 60 mm, and collars of different materials were employed. It was observed, that performances for some beams were moderately improved with collar lengths up to 30 mm.

The magnetic field structure of the minimum-B ECRIS causes the magnetic field lines to bunch together axially towards the extraction (and injection) region. The non-magnetized ions are not influenced by the field, but the electrons are, and thus due to the plasma quasi-neutrality condition, the ion density approximates that of the electrons. More importantly, it causes to some extent the ions to inherit the magnetic dynamics of the electrons. Numerical studies were conducted to show, that the flux of electrons into and along the collar has its origin towards the plasma center. This electron flux pulls the ions with them into the extraction aperture. This suggests that the origin of the ion beam, too, is along the axial direction further within the plasma. [32]

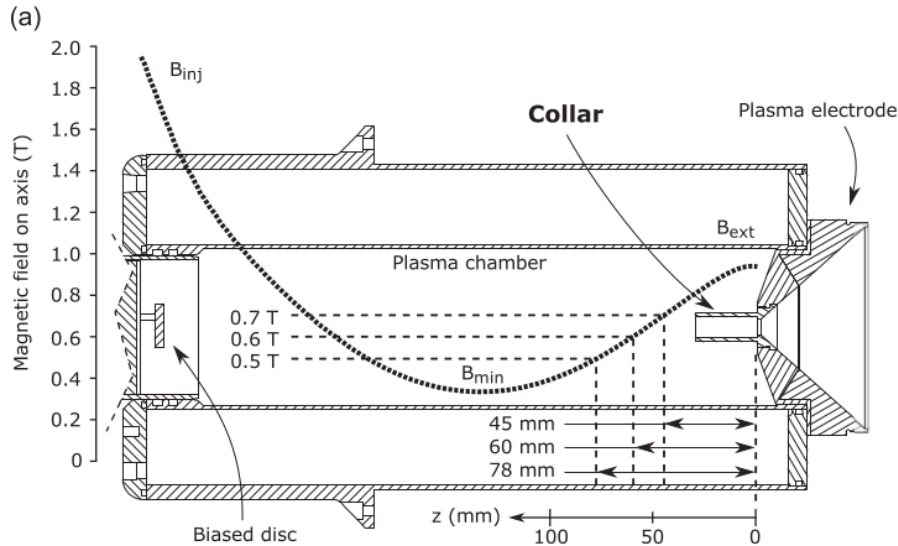


**Figure 26.** Schematic of the the plasma electrode fitted with a collar installed in the JYFL 14 GHz ECRIS plasma chamber. From [32]

### 4.3 Methods for improving ECRIS efficiency

Based on the discussion in section 4.2, the basic methods to increase ECRIS performance rely on increasing ion confinement times, which is achievable by ion cooling. The ambipolar diffusion model also suggests that decreasing the plasma potential should increase the confinement times.

As described in section 3.4, increasing the electron temperatures cannot provide indefinite improvements in HCI production, because the cross section for ionization begins to decrease for very high energies. For massive ions such as uranium, however, the ionization potentials are very high and increasing the electron temperatures is vital. As long as the plasma is stable, more microwave power can be injected (i.e. the electrons can be heated more) and neutral pressure be reduced (which reduces the charge exchange processes and thus increases HCI currents). In any case, as the electron temperature increases further the RF heating power begins to push them into the loss cone, which reduces the effectiveness of electron heating at high energy limit.

A brief description of some of the most common methods for improving HCI production in the ECRIS follows. For the purposes of this work, however, the most important is the gas mixing method, which is described in its own subsection.

**Negative bias disk:** A negative bias disk installed at the injection end of the ion source, can be used to increase the extracted ion currents from the plasma [19]. The negatively biased disk reflects electrons back towards the plasma interior, which inhibits the electron flux out of the plasma and thus decreases the plasma potential [22, 36] leading to increased ion confinement times. It has also been suggested that the improvement in the extracted currents is due to secondary electrons emitted into the axial region of the plasma chamber, which modifies the extraction properties

and thus causes the increase in extracted currents [37]. The negative bias disk is used in all the measurements in this work.

**Afterglow mode:** Another phenomenon speaking in favor of the potential dip model, is the so-called 'afterglow mode' or RF pulse mode, where the ECRIS is operated by injecting the microwave heating power into the source in pulses. It has been found that as the heating power is switched off, there is a sudden increase in the output of HCIs from the ion source, as can be seen in the figure 27. When the electron heating is switched off, the electrons begin to cool, and as they do, the hot electron population dissipates. This causes the potential well to disappear, which allows the ions previously confined in the trap to pour out[6]. This mode of operation for ECRIS is not applicable for supplying beams to cyclotrons, which require a continuous ion beam for correct operation, but the afterglow mode is ideal for injecting ion beams into synchrotrons.

**Plasma chamber materials:** The plasma potential is caused by electrons flowing out of the plasma volume, and onto the chamber walls. If the plasma chamber is coated with – or constructed out of – a material with a high secondary electron emission coefficient, the electron loss rate from the plasma can be balanced to some degree by electrons ejected from the wall coating material. The insulating effects of the coating material may also modify the plasma potential. [38] The plasma chamber of the JYFL 14 GHz ECRIS is made out of aluminum, which has been observed to be the most suitable metal as a plasma chamber material.

**Multiple frequency heating:** When an additional electron heating frequency is added, the production efficiency of the ion source has been observed to increase. The additional microwave frequency improves the ion source heating efficiency by providing another ECR surface [39], but also by suppressing plasma instabilities [40, 41]. It has also been observed that the additional heating frequency may slightly decrease the plasma potential value[42]. The beam intensities for krypton and xenon have been observed to increase twofold when the ECRIS is operated in double frequency heating mode, and by yet another factor of two when a third frequency is added[43].

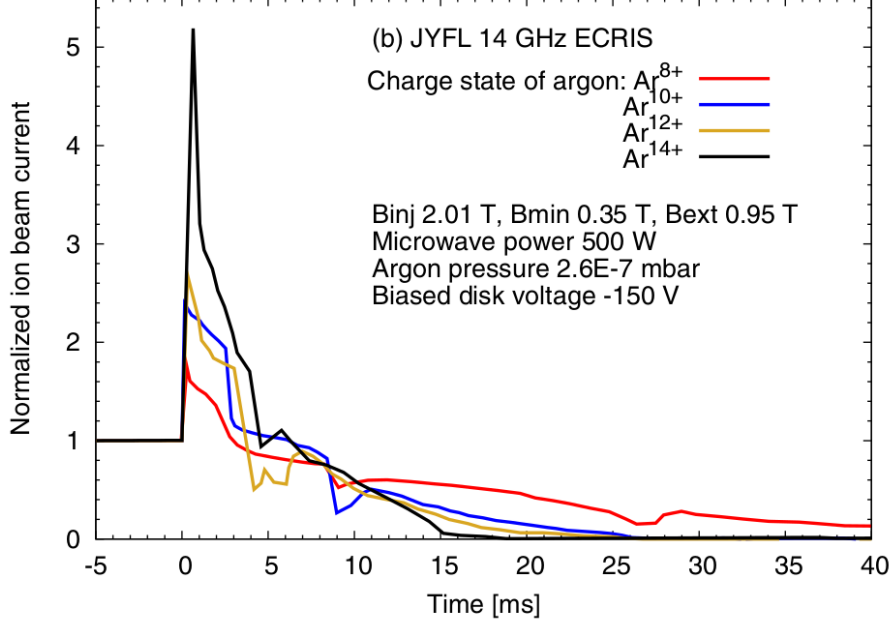


**Figure 27.** An example of afterglow current peaks for argon ions in the pulsed RF power regime in the JYFL 14 GHz ECRIS. From [44].

#### 4.4 Gas mixing

Gas mixing is a method where the HCI production in the ECRIS is significantly improved by mixing a lighter element into the plasma. In [21] it is shown, that the benefits of gas mixing are the result of improved ion confinement due to ion cooling. The temperature of the ion species, whose average charge state needs to be increased, is lowered in collisions with the lighter element: In the simplest case of an elastic head-on collision between two particles having masses  $m_1$  and  $m_2$ , the change in their speeds –  $\Delta v_1$  and  $\Delta v_2$  respectively – is determined by the relation  $|\Delta v_1| = |\Delta v_2| m_2 / m_1$ , whence it can be seen that the lighter element will deplete the heavier of its kinetic energy in the collision. As the ion temperature decreases, their confinement improves, which leads to its prolonged exposure to bombardment by electrons and thus to higher charge states.

In figure 28 the gas mixing -optimized argon currents and the ion temperatures calculated from the currents are shown as a function of the heating power. The figure shows the basic effect of gas mixing: introducing a lighter element causes the ion temperatures to decrease and consequently the HCI output to increase. It should be noted, that the gas mixing effect is not the simple result of the lighter gas depleting the heavier element of its kinetic energy, although that is a major part of it. As can be seen in figure 28, the ion temperature is lower when using  $^{22}\text{Ne}$  as the mixing gas than a lighter oxygen element. Regardless, the optimal ion current is achieved with  $^{18}\text{O}$ .

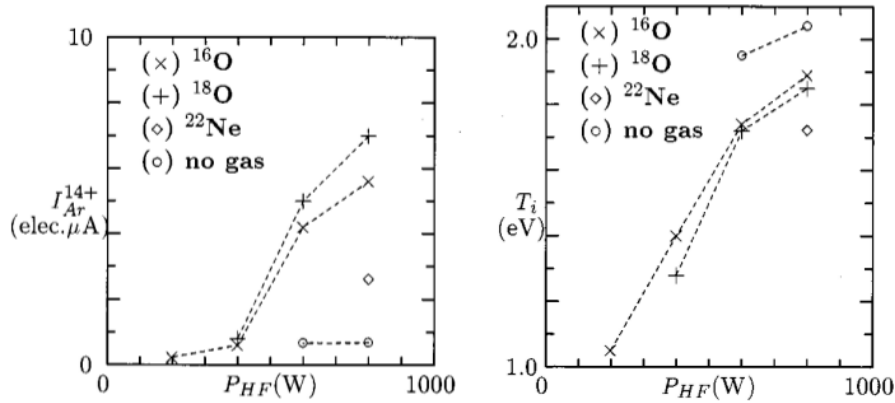


**Figure 28.** Gas mixing -optimized  $\text{Ar}^{14+}$  ion currents in  $\mu\text{A}$ , and calculated ion temperature  $T_i$  with respect to the input RF power  $P_{HF}$ . The maximum obtained ion current and the associated ion temperature are plotted in pure argon plasma, and argon plasma using either  $^{16}\text{O}$ ,  $^{18}\text{O}$  or  $^{22}\text{Ne}$  as mixing gas. From [21].

Neon – being a noble gas – has a low ionization rate compared to oxygen, which means that adding neon rather than oxygen would decrease the electron density of the plasma. Furthermore, a low mass element like oxygen only has low charge states available, which means that using oxygen as the mixing gas lowers the average charge state of the plasma. This in turn reduces the ambipolar losses from the plasma as a consequence of a lower plasma potential [4]. Additionally, the portion of low charge ions having an energy in excess of the confining potential barrier is much larger than for ions of higher charge, as can be seen from figure 20. This means that low charge ions can carry energy out of the plasma at a much higher rate than HCIs. Thus, in addition to the collisional mass effect, adding a light element to the plasma as a mixing gas will cool down the ions simply by carrying out energy from the plasma more efficiently.

On the other hand, the mixing gas should be massive in order to minimize the electron-ion equipartition power. According to equation (31), the electron-ion equipartition frequency becomes higher as the ion mass decreases. In other words, the equipartition time ( $\sim 1/\nu_{eq,e \rightarrow i}$ ) is less for light ions. On the other hand, the ion-ion energy equipartition time is very short (in the order of microseconds) regardless of the ion mass. As such, in a plasma comprising of a light and a heavy element, the light ion species can absorb energy from the electrons and conduct it to the heavy species. The particle loss rates and electron-ion equipartition powers determined by Melin *et al.* for the plasmas studied in [21] are depicted in figure 29. It can be seen that the particle loss rates as well as the equipartition powers are highest for the lighter mixing gases.

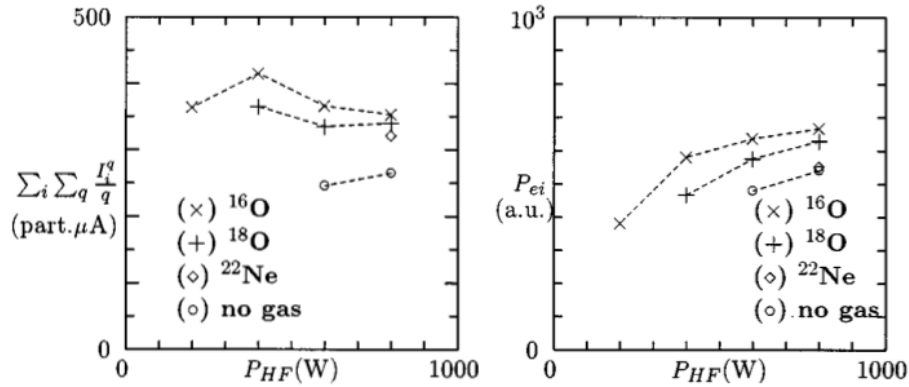


**Figure 29.** Total particle loss rate  $\sum_i \sum_q I_i^q/q$  in particle  $\mu A$ , and the calculated associated electron-ion equipartition power  $P_{ei}$  in arbitrary units with respect to the RF power for the same plasmas as in figure 28. From [21].

Thus, while the mixing gas should be light to reap maximum benefits of the collisional mass effect and energy loss via dilution, it should at the same time be massive in order to minimize the energy absorption from the electrons. Obviously these two requirements are at odds, and the only solution is a compromise between the two – in the case of Melin *et al.* in reference [21] the optimum is found with  $^{18}O$ .

In this work, copper is injected via sputtering into different buffer gases. Thus, the copper currents obtained are not determined solely by the amount of substance injected into the source, but they are heavily influenced by the gas mixing effects. Both the maximum currents and ion confinement times will be affected.

## 4.5 Material injection

The general method of material injection into ECRIS plasma is by gas injection. In fact, the ECRIS cannot produce a plasma if the fuel is not in the gas phase. Therefore, any material injected into the ECRIS must first be vaporised. This makes the production of especially metal ion beams challenging. There are a number of methods for injecting metallic elements into the ECRIS. All of them rely on a support plasma of another element (typically oxygen) in order to sustain the discharge, because the rate of material injection by these evaporative methods is typically quite small. This is usually not a problem, since the buffer gas provides ion cooling and actually improves the production rates of the desired ions. In the following, short descriptions of possible metal-ion injection methods are given, and a subsection is reserved for sputtering, which was chosen as the injection method in this work, as it allows the fast changes in the material injection rate that were required.

**Gaseous compounds:** Injecting a gaseous compound such as  $SO_2$ ,  $CH_4$ ,  $CCl_4$ , etc. can be used to produce beams from various metallic elements like sulfur, carbon and chlorine [45]. The injected gas molecules are atomized in electron impact and further ionized in the plasma. Injection of gaseous compounds is a simple, and thus a popular method of material injection, where the control over the gas input rate

allows easy tuning of the source [45]. The drawback of the method is the fact that the 'unwanted' elements in the compound are also injected into the plasma chamber, causing contaminations which may interfere with the ion source operation. This means that the viable compounds are limited to combinations of a desired heavy element and a light element, in order to take advantage of the gas mixing effects (see section 4.4) [45].

**Ovens:** Both low -and high temperature ovens are used to vaporize solid material for injection into the ion source [45]. The external heating of the oven is used to control the rate of material injection into the source, and is thus independent of the source parameters themselves [46]. The drawbacks of using oven methods are that the material consumption rate may be rather large, and that the extreme temperatures (in excess of 2100 °C) required to heat solids like tungsten and tantalum are not easily attainable [46].

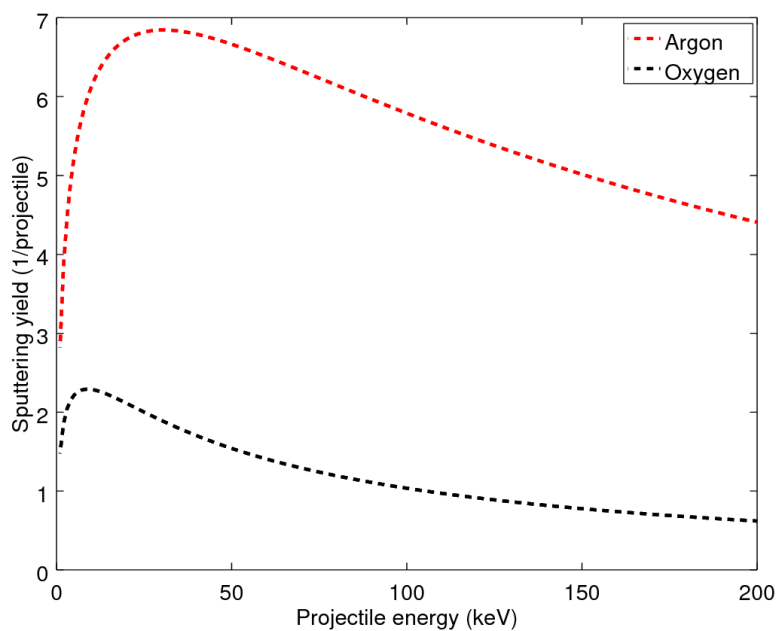
**The MIVOC method:** The MIVOC method (Metal Ions from Volatile Compounds) [47] utilizes chemical compounds containing metal atoms with ( $1 \times 10^{-3}$  mbar) vapor pressures at room temperature. Vapor from a vacuum chamber containing the volatile compound is allowed to diffuse into the lower pressure of the plasma chamber, where the gaseous molecule is atomized and subsequently ionized. Examples of the potential compounds include  $C_2B_{10}H_{12}$ ,  $Fe(C_5H_5)_2$  and  $(CH_3)_5C_5Ti(CH_3)_3$  which can be used to produce B, Fe and Ti beams respectively [48]. Unlike the oven method, MIVOC is not limited by the often very high melting temperatures of metals (e.g. Ti has a melting point of 1668 °C) [49]. The drawbacks of the method are that the chemical compounds contain many 'unwanted' elements – especially carbon, which contaminate the ion source, and that the number of suitable compounds is limited.

**Evaporation by plasma heating:** Instead of using an external heat source to vaporize the solid element, materials that have relatively low melting points may be inserted into the plasma chamber and be heated by the plasma itself [46]. The solid may be put in a tantalum 'boat' [50], which is then positioned at the plasma boundary by means of a mechanically driven wire. The boat itself is heated, and the vapor emanating from the solid enters the plasma through a vent hole in the boat. The material may also be heated directly by the plasma, in which case a metallic wire or an oxide pellet of the material may be inserted directly into the chamber [46]. Because the metal object inserted into the chamber interferes with the magnetic field configuration and the RF power propagation in the ion source, the plasma heating method comes with at the cost of added difficulties in optimizing the source [46].

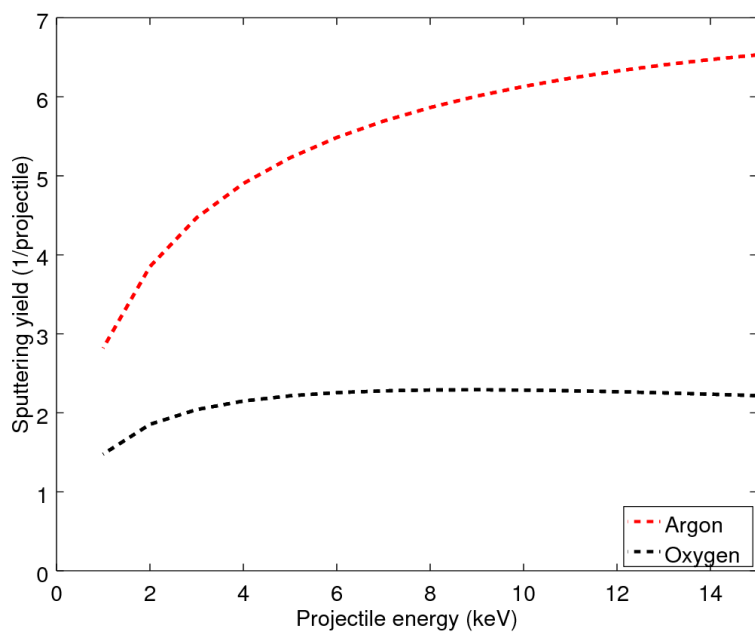
**Laser ablation:** The laser ablation method [46] applies a laser beam, which is targeted at a solid target positioned nearby the plasma boundary. Given a sufficient, target specific intensity of the laser beam, the beam evaporates substance from the target surface explosively. The explosion forces laser ablation plasma which rapidly expands. The expansion of the laser ablation plasma causes cooling and neutralization of the particles separated in the explosion, which form a flux of neutrals into the ECRIS plasma, where they have a high chance of becoming ionized [51]. The laser ablation technique can be used to produce ions of any solid material, and the

injection rate can be adjusted by varying the laser energy and repetition rate [37]. Laser ablation is pulsed by nature.

### 4.5.1 Sputtering method for material injection



(a)



(b)

**Figure 30.** The sputtering yield from a copper target for oxygen and argon projectiles with respect to energy. The general shape of the sputter yield is shown in (a) and the yield in the energy range more relevant for the sputtering voltages employed in this work in (b). Calculated using code from [52].

Sputtering[53, 54] is a phenomenon in which an ion impinging into a material breaks off atoms from its surface. Sputtering always occurs in ion sources as the plasma ions (accelerated by the plasma potential and plasma instabilities) collide with the chamber walls, but it is also intentionally employed as a method for metal injection into the source. In the sputtering method, a metal sample (the sputter sample) is positioned at the plasma chamber wall, and biased to a negative voltage, causing the sample to attract the positively charged ions from the plasma and accelerating them towards the sample. Upon collision, the ions cause sputtering from the surface of the sample, separating neutral atoms from the material which then pass into the plasma unaffected by the plasma potential or the confining magnetic field, until they become ionized by collisions with electrons in the usual manner.

The ratio of sputtered atoms to projectiles striking the sputtering probe is referred to as the sputtering yield:

$$Y = \frac{\text{sputtered atoms}}{\text{projectiles on target}}, \quad (42)$$

and it typically ranges between 0.1 and 10. The sputtering yield is a quantity dependent on the energy and angle of incidence of the projectile, as well as the structural integrity of the target material i.e. how difficult or easy it is to separate its atoms.

Sputtering yield for a copper target and argon or oxygen projectile is presented as a function of energy in figure 30. The yields in the figure are calculated based on empirical equations for sputter yields at normal incidence by [55] in a sputter yield code from [52]. The yield initially increases with the projectile energy, until it reaches a maximum value whence it begins to decrease. The reason for this is, that as the energy of the projectile increases, its penetration depth also increases. This means that at higher beam energies the ion will break off atoms from the target so deep within its surface, that the atoms cannot make their way out of the material. For this same reason, the sputtering yield is found to be highest when the projectile impinges on the target at an angle of around 60 to 80 degrees with respect to the surface normal[56]: As the ion comes in almost parallel to the surface, its energy is deposited in a narrow region near the surface, which allows any separated atoms to be easily ejected from the material.

The ions attracted by the voltage on the sputtering probe will have energies that are multiples of the accelerating potential (since the energy (in eV) of a particle having charge state  $q$  accelerated over a voltage  $V$  is  $qV$ ). This means that the average sputtering yield is acquired by averaging the energies over the charge state distribution of the different ion species in the plasma<sup>8</sup>:

$$Y_{\text{avg}} = \sum_{q=1+}^{q=q_{\text{max}}} w_q \cdot Y(qV), \quad (43)$$

where  $w_q$  is the fraction of ions having charge  $q$  colliding with the sample and  $V$  is the sputtering voltage.

---

<sup>8</sup>Assuming, of course, that the different charge states are uniformly distributed in the plasma volume. This is doubtful, as the HCIs are believed to be formed in, or near, the plasma center (see section 4.2.2). If only the low charge states are available near the sputtering probe, the average sputter yield is lower.

## 5 Experimental setup and methods

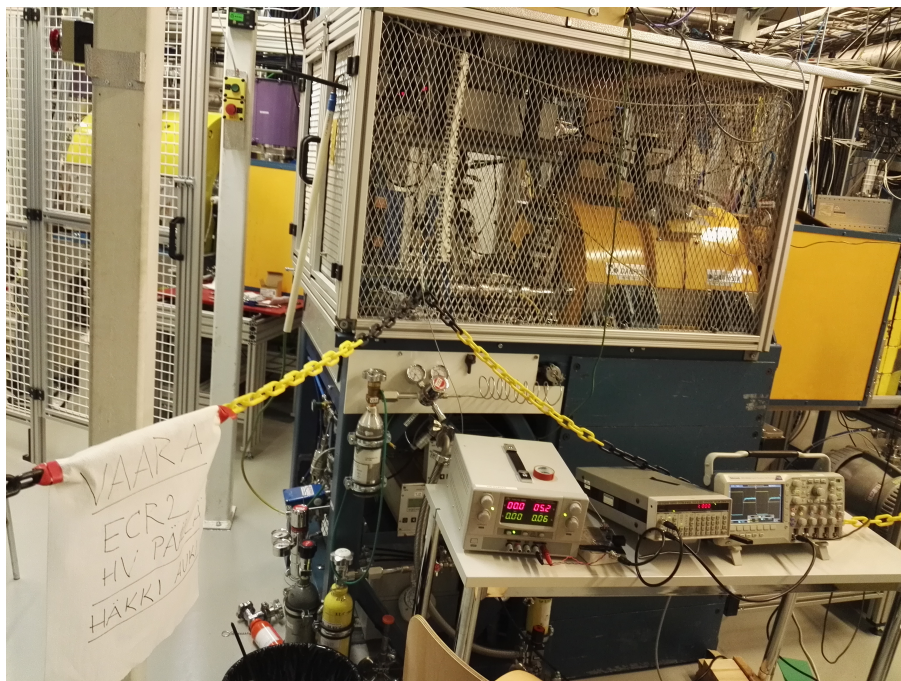


**Figure 31.** The JYFL 14 GHz ECRIS and the experimental setup for the parameter sweeps.

The experiments detailed here were carried out at the JYFL Accelerator Laboratory in the Department of Physics, University of Jyväskylä. The laboratory is equipped with three ECR ion sources used to produce heavy ions for the K130-cyclotron[57] employed in accelerator based, fundamental nuclear -and particle physics research. The JYFL 14 GHz ECRIS[58] – colloquially known as the ECR2 – was chosen for the experiments, as it is equipped with a radial port enabling the use of the sputtering method. The plasma chamber and the radial ports are shown in figure 32.

The purpose of the work presented in this thesis was to develop a method for estimating the ion confinement times from the transient current signal of an ion species, with a certain  $m/q$ -value, as it is being extracted from the plasma. It is assumed on the basis of the balance equation presented in section 4.1, that the time constant of the transient is proportional to the ion confinement time.

These time constants are studied as functions of the different operating parameters of the ECRIS. By independently varying the magnetic field, gas pressure, RF heating power,

the sputtering voltage, and the buffer gas, and by studying their effects on the scale of the time constant, the justification for drawing an equivalence between it and the confinement time is sought.

In the experiments, material injection into the plasma chamber was controlled by sputtering copper into a continuously sustained buffer gas plasma. The sputtering voltage was controlled using a TTL-guided switch developed in preparation for these experiments as a research training project during the summer of 2017. In the parameter sweep experiments, the sputtering voltage was pulsed at a frequency of 1 Hz (voltage on 500 ms / voltage off 500 ms) which was enough for the extracted copper beam current to saturate and decay – i.e. for the number density of copper to reach equilibrium while the sputtering was on, and for all the copper to be ejected from the plasma when the sputtering was off.

In addition, the ion production times were studied by means of fast sputtering. Here, the sputtering time was gradually shortened until the voltage was on for only 2 ms during a pulse. The resulting copper beams for the different pulse lengths were studied, and the possibility of determining ion production times from the extracted beam was considered.

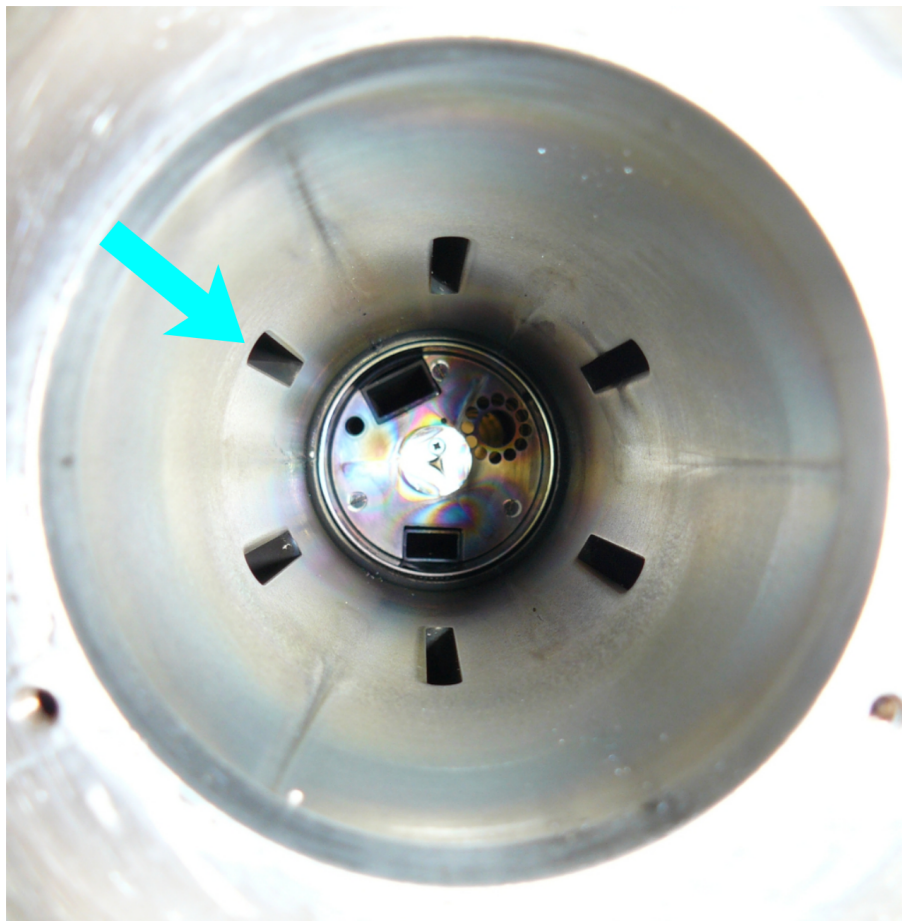


**Figure 32.** Picture of the JYFL 14 GHz ECRIS plasma chamber. One of the radial ports is indicated with the cyan arrow. Picture taken from the extraction end of the source. The negative bias disk can be seen at the injection end.

## 5.1 JYFL 14 GHz ECRIS

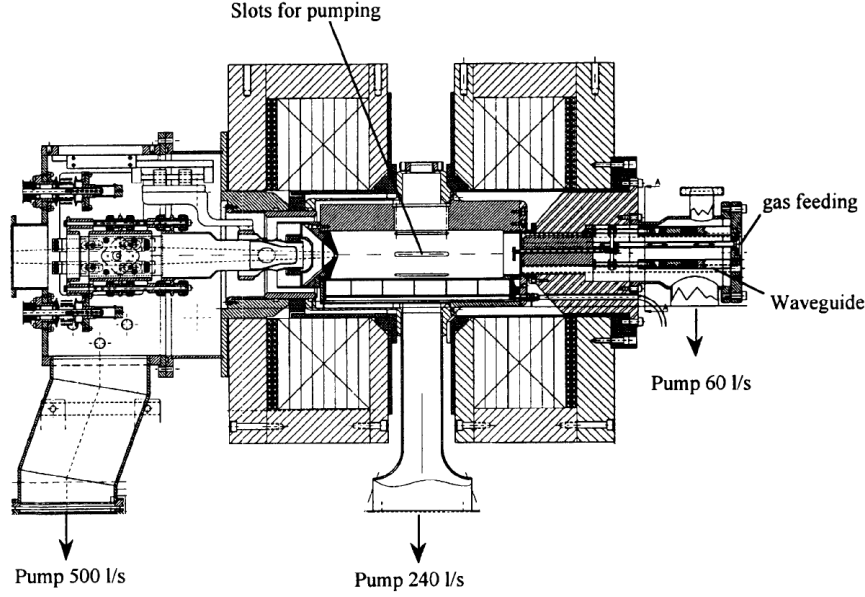


**Figure 33.** A schematic of the JYFL 14GHz ECRIS – or ECR2. Injection end to the right and extraction to the left. From [58].

The JYFL 14 GHz ECRIS – see figure 31 – is a room temperature ECR ion source based on the design of the AE-CR-U at the Lawrence Berkeley National Laboratory (LBNL), University of California. A schematic of the ion source is presented in figure 33, and a three dimensional representation in figure 34. The main operation parameters of the source are tabulated in table 2. The first plasma was ignited in the source in February of the year 2000[58]. The ion source extraction end has been upgraded in 2013[32].

The ion source operates at a main microwave frequency of 14.056 GHz with a maximum power of 2.5 kW (limited to 1 kW in normal operating conditions), but it can also be operated in multiple frequency heating mode (see section 4.3) thanks to the secondary microwave input produced by a Traveling Wave Tube Amplifier (TWTA) with a variable frequency in the range of 10.75 GHz – 12.45 GHz. The axial magnetic field is generated by two sets of solenoids, which are excited by two power supplies to a maximum current of 650 A at 95 V. The radial magnetic field is provided by NdFeB hexapole magnets. The maximal on-axis fields in the injection and extraction ends are 2.0 T and 1.0 T respectively. The magnetic field at resonance is 0.50 T. The hexapole magnets provide a radial magnetic field of approximately 1.07 T at the poles. With these values, the magnetic field conforms to the experimentally determined conditions for stable operation [59, 60]

$$B_{\text{ext}}/B_{\text{ECR}} \geq 2 \quad (44)$$

$$B_{\text{inj}}/B_{\text{ECR}} \geq 4 \quad (45)$$

$$B_{\text{rad}}/B_{\text{ECR}} \geq 2 \quad (46)$$

$$B_{\text{min}} \approx 0.4B_{\text{rad}} \quad (47)$$

$$B_{\text{ext}} \approx 0.9B_{\text{rad}}. \quad (48)$$

Here  $B_{\text{ext}}$  and  $B_{\text{inj}}$  correspond to the maximum axial values of the magnetic field at the plasma chamber extraction and injection,  $B_{\text{rad}}$  is the maximum radial field,  $B_{\text{min}}$  the field minimum and  $B_{\text{ECR}}$  the field at resonance. Configuring the magnetic field such that these relations are approximately met has been found to result in stable operation conditions.

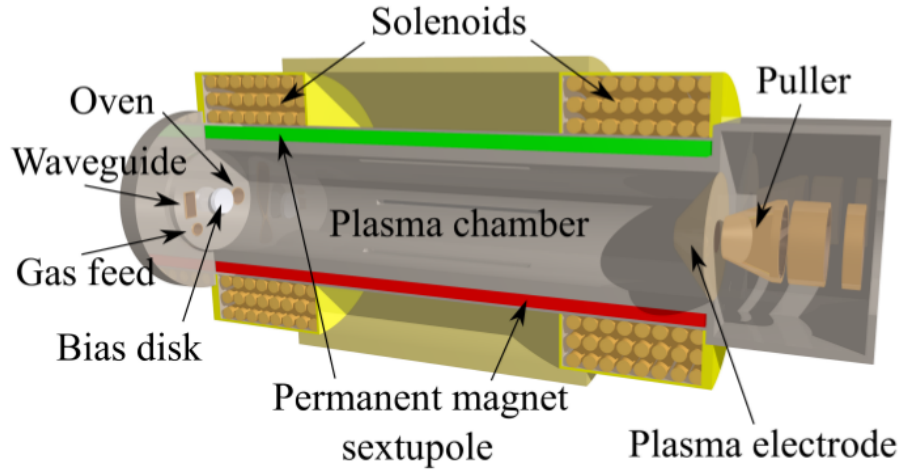


**Figure 34.** Schematic of the ECRIS basic structure. From [61].

**Table 2.** Main parameters of the JYFL 14 GHz ECRIS [58, and changes thereafter].

Main parameters	
Operating frequency	14.1 GHz
Maximum radial field on wall	1.07 T
Hexapole	NdFeB
Maximum axial field at injection	2.0 T
Maximum axial field at extraction	1.0 T
Coils' power supplies	$2 \times 650\text{A} / 95\text{V}$
Extraction voltage (max)	20 kV
Vacuum pumps	
Injection	60 l/s
Plasma chamber	240 l/s
Extraction	500 l/s
Base vacuum in plasma chamber	$\approx 3 \times 10^{-8}$ mbar



**Figure 35.** The sputter probe.

## 5.2 Pulsed sputtering method for material injection

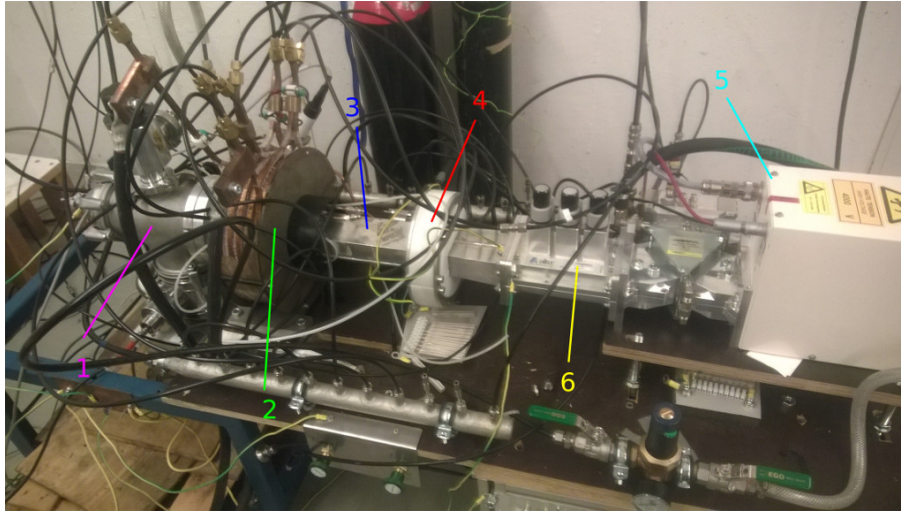


**Figure 36.** The diagnostics purposes microwave ion source. The main components: (1) the pumping chamber, (2) plasma chamber surrounded by a coil, (3) wave guide (4) insulator (5) 2.45 GHz microwave generator and (6) a set of impedance matching stubs.

In preparation for these experiments, a pulsed sputtering setup was developed and tested in the spring of 2017. The rig consisted of a fast high voltage switch and the sputter probe, shown in figure 35. The rig was tested using a small 2.45 GHz microwave ion source set aside for diagnostics purposes at the accelerator laboratory.

The diagnostics ion source is shown in figure 36. The pumping chamber is connected to a vacuum pump and a turbo pump. The plasma chamber is connected to the pumping chamber via the beam extraction end. In operation conditions the plasma chamber was kept at approximately  $5 \times 10^{-5}$  mbar pressure. Because there is only one coil wound around the chamber, and there is no magnetic multipole configuration, the plasma is not truly confined, but the magnetic field of the coil allows the heating of the electrons by microwaves, although no closed ECR surface is formed.

The plasma chamber is fitted with an optical port, which allows the measurement of light spectra from the plasma. To verify that the sputtering probe worked, the optical spectrum of a pure argon plasma was compared to spectra measured as the sputtering voltage was increased. In figure 37 is shown an example of the relative spectra in the 300 nm wavelength neighborhood. It can be seen that two peaks characteristic to copper, but not to argon, appear as the sputtering voltage is increased. Because the sputter probe

attracts ions from the plasma, the power source must constantly supply a current to the metal sample in order to maintain the negative bias. At -2000 V potential the power source's internal safety limit for the current was met, and the sputtering voltage could not be maintained for longer than a few seconds. The high -2 kV sputtering bias was required, because the diagnostics source is not capable of producing high charge states, and its plasma consists mainly of ions in the 1+ state, with the occasional 2+ charge. In contrast, it was found that in the JYFL 14 GHz ECRIS a bias of -700 V is quite sufficient.

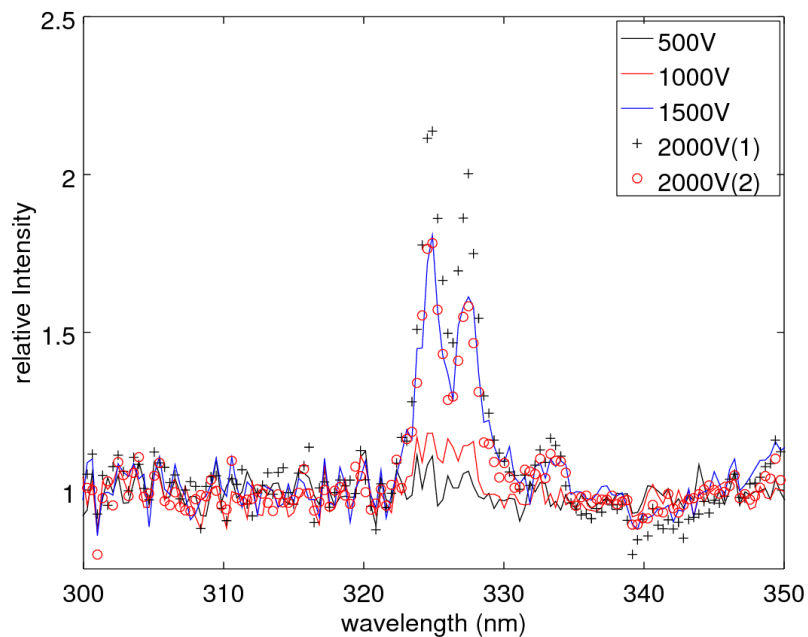


**Figure 37.** The optical spectra measured from the diagnostics source at increasing sputtering voltages relative to the pure argon plasma. The source was operated at 2.45 GHz, 200 W microwave frequency and power at  $6.3 \times 10^{-5}$  mbar pressure in the pumping chamber with argon as the buffer gas. The sputter probe was injected axially.

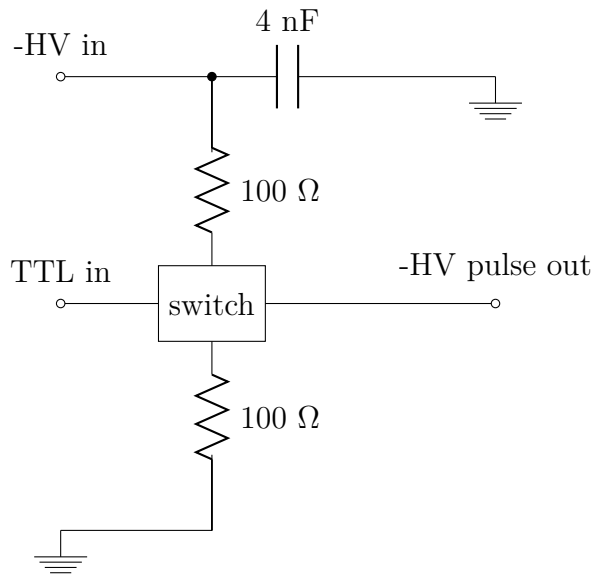


**Figure 38.** Circuit diagram for the switch connections. The switch takes in negative high voltage and the TTL signal, and outputs the negative high voltage pulse.



**Figure 39.** The BEHLKE FAST HIGH VOLTAGE PUSH-PULL SWITCH. The black wire takes negative high voltage in and the yellow wire outputs the pulsed high voltage. The red wire is for alternative mode positive high voltage input, but here it's used as the ground wire.

As the sputter probe was found functional and a reasonable sputtering voltage threshold was acquired, the green light was given for rigging the sputter probe with a switch capable of quickly switching on and off the probe voltage. A FAST HIGH VOLTAGE PUSH-PULL SWITCH by BEHLKE was chosen based on its ability to handle the high voltages involved. The circuit diagram of the switch is shown in figure 38, and a picture of the switch in figure 39. The switch was operated using a 1 Hz TTL signal from a function generator. Upon closing or opening the switch, the sputtering voltage was found to rise and decay in around 50 $\mu$ s. It is important that the sputtering voltage decays quickly, because the ECR plasma contains highly charged ions, whose energy can be of order keV when accelerated

over a 100 eV voltage, and thus can have high sputtering yields. Given that the dissipation time for the voltage is of the order of 100 microseconds, and the first ionization times in the ECRIS are in the order of milliseconds[62], we can safely say that the sputtering ceases before ionization begins to affect the equilibrium conditions in the plasma.

### 5.3 Transient of the ion current

As metal atoms are sputtered into the plasma and ionized, the number densities of the different charge states will develop towards a new equilibrium: the change in time of the ion density tends to zero, and the balance equation (35) becomes

$$\frac{dn_i^q}{dt} = 0 \quad (49)$$

or

$$\begin{aligned} \frac{n_{i,eq}^q}{\tau_i^q} = & + n_e n_i^{q-1} \langle \sigma v \rangle_{q-1 \rightarrow q}^{ion} - n_e n_i^q \langle \sigma v \rangle_{q \rightarrow q+1}^{ion} \\ & + n_0 n_i^{q+1} \langle \sigma v \rangle_{q+1 \rightarrow q}^{cx} - n_0 n_i^q \langle \sigma v \rangle_{q \rightarrow q-1}^{cx}, \end{aligned} \quad (50)$$

where  $n_{i,eq}^q/\tau_i^q$  is the loss term at equilibrium. In other words, equation (50) states, that ions diffuse and are transported out of the plasma at the same rate as they are being formed. The loss term at equilibrium can be substituted in place of the first four terms of the balance equation to yield a separable differential equation, which has the solution

$$n_i^q(t) = n_{i,eq}^q [1 - \exp(-t/\tau_i^q)]. \quad (51)$$

By differentiating the previous equation we get

$$\frac{dn_i^q}{dt} = \frac{n_{i,eq}^q}{\tau_i^q} \cdot \exp(-t/\tau_i^q) \quad (52)$$

and since the extracted ion current is proportional to the time derivative of the ion number density, it can be seen that the ion current decays exponentially from the equilibrium state due to the diffusion and transport coefficient as

$$I_i^q = I_{i,sat}^q \cdot \exp(-t/\tau_i^q), \quad (53)$$

where  $(n_i^q/\tau_i^q)_{eq}$  is taken to represent the steady-state saturation current  $I_{i,sat}^q$ . Strictly speaking, the extracted current is proportional to the axial confinement time. It was shown in [32] that the extracted ion beam originates in somewhere in the plasma center regions, and – pulled by the escaping electrons – propagates axially through the extraction aperture. Thus, due to the spatial distribution of the ions (see section 4.2.2) at least for the HCIs the axial confinement time corresponds well to the total confinement time (see equation (36))

In a short span of time after the sputtering has been ceased the equilibrium conditions have not changed substantially and the main component contributing to the decay of the ion current is the diffusion term of the balance equation, which defines the confinement

time. By measuring the ion current transient when the material injection is ceased, the time constant of the transient should correspond to the ion confinement time  $\tau_i^q$ . A similar treatment is presented in [63], where it is also shown that the decay constant is a lower bound of the confinement time. It is also shown, that if the ionization and charge exchange rates can be neglected, the decay constant should be equivalent to the confinement time. This suggests that by applying the fit to the transient only in the region where the ion current has not yet decayed significantly from the saturation current, the obtained time constant would be closer to the true value of the confinement time (See section 6.2).

## 5.4 Measurements with the JYFL 14 GHz ECRIS

Two sets of measurements were carried out: parameter sweeps of the ion current transients, and a fast sputtering experiment. In the parameter sweeps, the goal was to measure the transients of the ion current when material injection to the plasma is ceased. Parameter sweeps were conducted by independently varying one of the operating parameters of the ECRIS, and then measuring the transient.

Figure 40 shows a flow chart of the measurement setup. A negative high voltage from a JYFL PROXANT NP 23 high voltage source was run through the switch, while a SRS MODEL 05345 30 MHz SYNTHESIZED FUNCTION GENERATOR supplied the square pulse (TTL) signal, which was used to operate the switch (In the fast sputtering experiment, the function generator was replaced by a DIGILENT ANALOG DISCOVERY multi function instrument). The TTL signal was run through optical isolation, which allowed operating the control system at ground potential while the sputter sample and its voltage switch were floating at the ion source potential. The switch control box could be used to determine whether the square pulse got through to the switch – i.e. whether the sputtering voltage was pulsed or continuous. From the switch, the negative high voltage is directed to the sputter probe itself, which is radially injected into the ion source. The sample was injected from in between the magnetic poles such that its surface was in the same level as that of the plasma chamber wall (radial ports are indicated in figure 32). The beam was extracted towards the magnetic dipole, where the ions were separated according to their charge to mass ratio. The ion current selected at the dipole was then collected at the Faraday cup (FC). Because of the low, microampere scale currents, the current was first sent through a SRS MODEL SR570 LOW-NOISE CURRENT PREAMPLIFIER. Finally, the current was measured at the TEKTRONIX DPO 2024B DIGITAL PHOSPHOR OSCILLOSCOPE. Due to noise, the currents were averaged over 16 samples. For currents with a very high noise/signal ratio, the averaging was done over up to 128 samples.

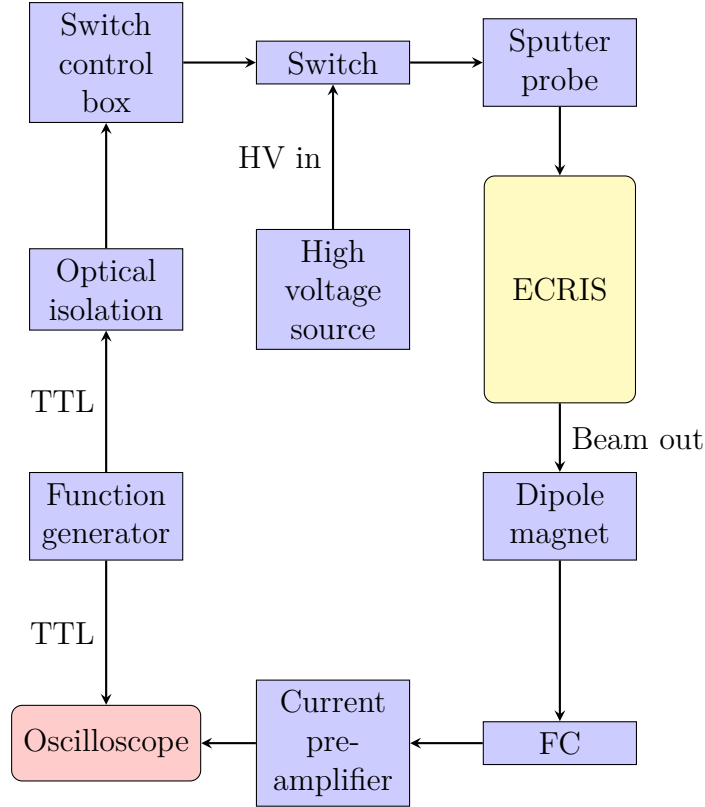


**Figure 40.** Flow chart of the experimental setup.

#### 5.4.1 Parameter sweep measurements

By default, the operating parameters of the ECRIS were set to  $B_{\min}/B_{\text{ECR}} = 0.68$ , heating power 300 W and sputtering voltage  $-700$  V. The plasma chamber gas pressure was approximately  $1 \times 10^{-7}$  mbar  $- 2 \times 10^{-7}$  mbar, but it was only precisely measured (with the heating power at 0 W) in the pressure sweep measurement. Otherwise the pressure was determined by optimizing the gas input to achieve the desired HV leak current at operating conditions. The buffer gas input was adjusted such that the HV leak current was approximately 1 mA<sup>9</sup>. This was done while the sputtering voltage was on, to maximize the extracted current while copper was also present in the plasma. The extraction voltages were set to typical values: extraction High Voltage (HV) at 10 kV, puller-electrode at 0.5 kV and the einzel lens at 6 kV. The negative bias plate at the injection end of the source was kept at  $-50$  V bias.

In each parameter sweep the function generator was set to produce a square pulse at a 1 Hz frequency, causing the sputtering probe bias to be on for 500 ms and off for 500 ms in one period. The 500 ms on/off time was sufficient for the ion current to saturate and to completely decay. The dipole magnet was then used to select  $^{63}\text{Cu}^{q+}$  beams such that the  $m/q$  peaks did not overlap with those of the background plasma. The beam current was collected at the FC, and guided via a pre-amplifier to the oscilloscope. Each ion current

<sup>9</sup>The leak current corresponds to the net current out of the ion source, and it is measured at the HV source. The leak current needs to be compensated for the source to remain at the correct potential.

maximum was found by adjusting the beam line focusing solenoid and the dipole magnet until the current measured at the oscilloscope peaked. Transients for the currents were then measured for as many  $^{63}\text{Cu}$  charge states as possible. The sweep parameter was then adjusted and the process repeated. The parameter sweeps were made with respect to the coil currents, microwave heating power, sputtering voltage, plasma chamber pressure and the buffer gas species.

#### **5.4.2 Fast sputtering measurements**

The setup for the fast sputtering experiment was the same as for the parameter sweeps, except that the function generator was replaced by a DIGILENT ANALOG DISCOVERY multi function instrument, which was used to produce the asymmetric sputtering pulse. The pulse frequency was still kept at 1 Hz, but the symmetry was varied such that the sputtering pulse was gradually shortened until the pulse duration was no more than 0.3 ms. The currents were measured as before in the parameter sweeps. The ECRIS operating parameters were set to the default values listed in the previous section.



## 6 Results and analysis

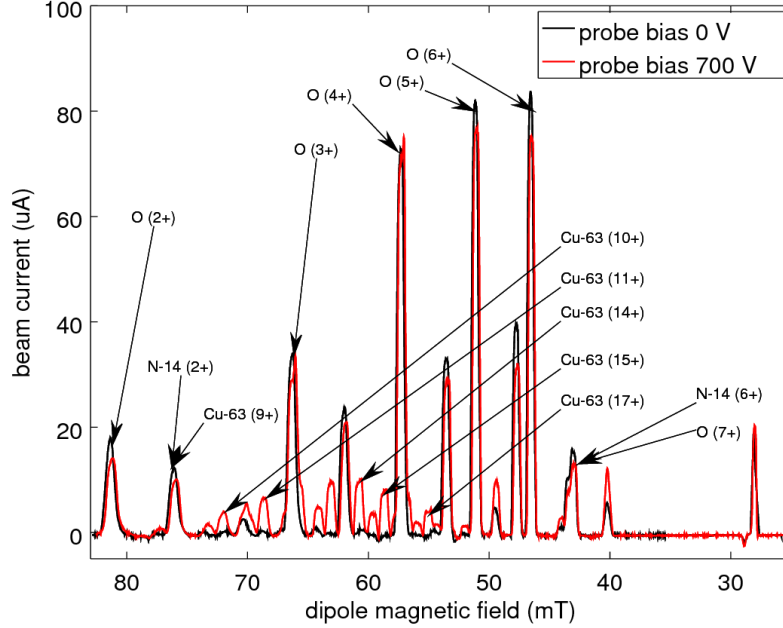


**Figure 41.** The charge state distribution in the ion beam extracted from an oxygen buffer plasma without and with sputtering probe bias.

The experiments with ECR2 were initiated by igniting an oxygen plasma and measuring the extracted charge state distribution (CSD) of the ions. The sputtering probe was then biased to a steady voltage and the CSD was scanned again, to verify that sputtering takes place. This scan was repeated for a -700 and -1000 volt bias on the sputtering probe. It was found that -700 volts is sufficient for measurable amounts of copper – specifically  $^{63}\text{Cu}$  – to be sputtered into the plasma. Comparison of the spectra is shown in figure 41. In addition to the oxygen and copper, there are impurities in the plasma chamber – either contaminations from previous runs or residues of air and moisture. Nitrogen remnant has been indicated in the figure, but hydrogen and carbon are also present. Impurities in the plasma interfered with the measurements: For example, in figure 41 can be seen the overlap in the CSD between  $^{14}\text{N}^{2+}$  and  $^{63}\text{Cu}^{9+}$ , both of which have a charge to mass ratio  $q/m = 2/14 = 9/63 = 1/7$ , and consequently are not separable in the magnetic dipole. In order to measure the transient of the copper current, the peaks in the CSD need to be distinctly separate<sup>10</sup>. Oxygen is thus a good choice for buffer

<sup>10</sup>Furthermore: The gas mixing effects of the added copper – and the sputtering voltage itself – cause changes in the CSD. As such, the additional copper current does not appear simply on top of the nitrogen

gas in these experiments, as its few available charge states reduce the number of overlaps.

The default settings used in the experiments were such that the  $B_{\min}/B_{\text{ECR}}$  was set to 0.68 (well below the instability threshold), microwave heating power to 300 W, and the sputtering voltage to -700 V. The gas injection was set such that the resultant HV leak current was approximately 1 mA. Whenever the pressure is explicitly written, it is given as a raw value of the pressure gauge i.e. for the  $N_2$  calibration<sup>11</sup>.

## 6.1 Selecting the fitting range

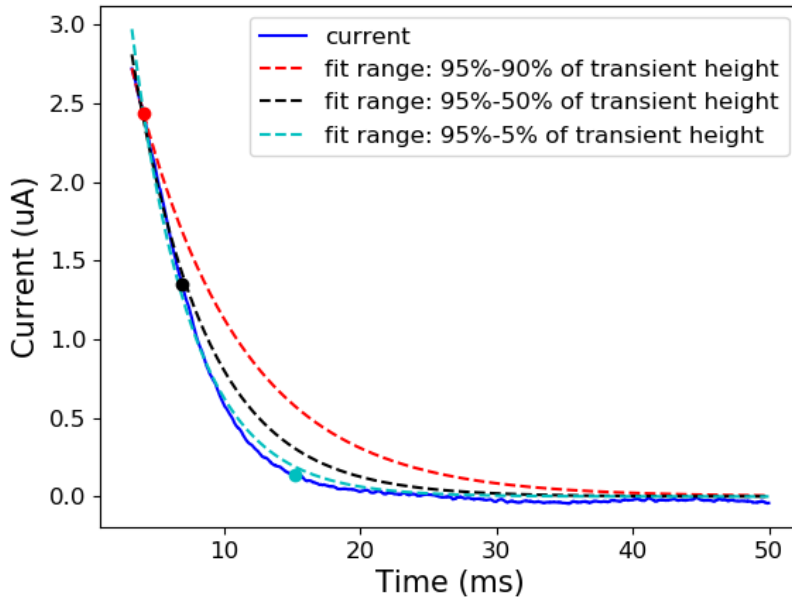


**Figure 42.** Examples of exponential fits made to the current transient with different fitting ranges. Three fits made to the transient of  $^{63}\text{Cu}^{10+}$  in an oxygen plasma are illustrated. The source was operated at 300 W heating power, with  $B_{\min}/B_{\text{ECR}} = 0.68$ , and a sputtering bias was  $-700$  V. The chamber pressure was set such that the HV leak current was approximately 1 mA. All fitting ranges begin from 95% of the saturation current (i.e. the transient height).

Next, the sputtering voltage was pulsed at a 1 Hz frequency – sufficient for the ion currents to saturate at their maximum values, and the transients of the currents were studied. In

---

current in the CSD, but rather the nitrogen current is modified by the effects of sputtering.

<sup>11</sup>Different gases have different calibration coefficients, thus a pressure of  $1 \times 10^{-7}$  mbar measured for e.g. oxygen and helium would be different for both of the two gases. Additionally, the pressure is measured outside of the plasma chamber through one of the radial ports, so the pressure reading does not correspond to the true chamber pressure. The pressure is, however, considered just an operating parameter of the ECRIS – specific to the ion source – and simply correlates with pressure dependent quantities in the plasma.

figure 42 are shown three fits to the transient of an extracted  $^{63}\text{Cu}^{10+}$  current. The fitting ranges are chosen such that the fit begins from 95% of the saturation current – i.e. the transient height – and ends at some other percentage ( $xx\%$ ) of the saturation current. In the figure, the lower limit of the fitting range for each fit is shown with a colored dot on the transient.

Figure 43 shows the behavior of the time constant with respect to the fitting range for  $^{63}\text{Cu}$  charge states 10+ and 17+. The x-axis value corresponds to the lower limit of the fitting range, as a percentage of the maximum height of the transient (see figure 42.). It can be seen that the time constant becomes shorter as the fitting range is expanded.

There are two reasons for the dependency of the time constant on the fitting range. First and foremost, in the derivation of the transient equation (53) it was assumed that the plasma is in equilibrium conditions. The equilibrium, however, is perturbed as the lost ions are no longer replaced by material injection via sputtering. This causes the ion particle densities, and consequently the ionization rates, to decrease. As a consequence, the time constant appears to decrease, although the apparent decrease is due to the failure of the assumption of equilibrium conditions: It can be seen from equation (50) that as the ionization rates decrease the time constant must also diminish in order for the equilibrium assumption to hold. This indicates a failure of the transient equation to describe the current beyond a few milliseconds after the switching off of sputtering.

Secondly, the first ions to escape are the ones having the largest energies. They thus carry out the ionic energy from the plasma, leaving behind only ions having small energies. This means, that as the highly energetic ions evacuate the plasma, the remnant ions will be better confined due to their smaller temperature. This, contrary to the observed behavior in figure 43, increases the time constant. It can be inferred that the decay of the equilibrium conditions is a more significant contributor to the dependency.

Therefore, the time constant obtained from the fit in the narrowest fitting range – from 95% to 90% – should best correspond to the confinement time. When, however, the operating parameters of the ECRIS were set to 300 W heating power,  $B_{\text{min}}/B_{\text{ECR}} = 0.68$ , and sputtering voltage of -700 V the time constants obtained were very long – in the case of the charge state  $q = 17$ , the decay constant was found to be 31.1 ms. For the charge states 14 and 10 the time constants were 21.8 ms and 7.7 ms respectively. Thus, the given time constants are believed to be more representative of the cumulative confinement time than the confinement time of an ion at a specific charge state. It can also be seen from figure 42, that by using the complete transient range from 95% of saturation to 5% the best fit can be obtained. Because of this, the decay constants presented in the following sections have been determined from fits to the complete transient range<sup>12</sup>. Nevertheless, a sample of the time constants obtained from the short fitting range is also presented in section 6.2.

---

<sup>12</sup>Neben *et al.* [64] also fit to the full transient length, so the choice here is further influenced by convenience of comparison of the results.

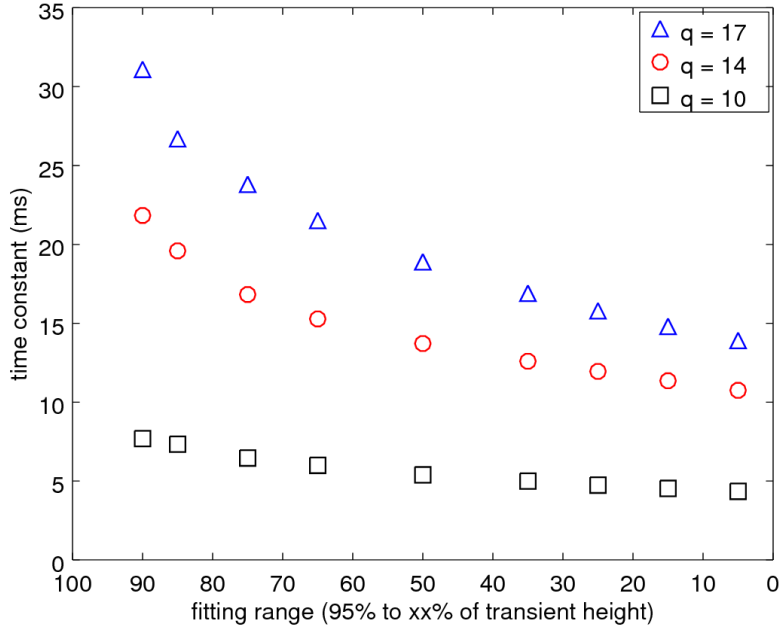


**Figure 43.** The time constant of the exponential fit to the current transient as a function of the fitting range. The dependency is illustrated for  $^{63}\text{Cu}$  charge states 10+ and 17+ in an oxygen plasma at 300 W heating power with  $B_{\text{min}}/B_{\text{ECR}} = 0.68$ , and a sputtering voltage of  $-700$  V. The chamber pressure was set such that the HV leak current was approximately 1 mA.

## 6.2 Error estimation

The ion currents extracted from the ECRIS are subject to significant internal uncertainty of the ion source itself – much greater than that of any of the other measurement apparatus involved in the experiment. The uncertainty is due to the dependency of the ion source operating conditions on, for example, contaminations from previous runs, small deviations in the gas pressure, and – simply put – unknown reasons, which affect the extracted currents in unpredictable ways. Therefore, the error analysis is done by comparing time coefficients acquired from different measurements at the same ion source parameter settings.

Five separate parameter sweep experiments were conducted. In each experiment, the default setting for the ECRIS operation was: heating power 300 W,  $B_{\text{min}}/B_{\text{ECR}} = 0.68$ , sputtering voltage  $-700$  V and oxygen buffer gas, whose pressure was set such that the leak current of approximately 1 mA was achieved. In each experiment, there is thus one data point corresponding to a transient measured at these settings. By averaging the time constants acquired from all the parameter sweep experiments, and calculating the standard deviation, an estimation for the uncertainty of the time constant can be acquired. The thus obtained averages of the time constant, their standard deviations and relative uncertainties are listed in table 3.

From the table it can be seen, that there is a significant uncertainty to the average value

of the time constant. The uncertainty ranges from  $\sim 10\%$  to  $\sim 20\%$ . There doesn't seem to be a clear tendency to the uncertainty with respect to the ion charge state, but the error estimate is higher for the high charge states, which are more sensitive to variations of the ion source parameters. The sample size is not very large – the average values and standard deviations are determined from five measurements per charge state (four for charge states 11 and 14), which makes the analysis statistically questionable. In any case, it can be assumed that the relative uncertainty of the time constants determined from fits to the full length of the transient is around 20%.

In section 6.1 it was noticed that the effect of the fitting range on the scale of the decay constant is very significant. For fits to just the beginning portion of the transient, the time constant is twice as large as those obtained from fits to the full transient length.

For the sake of comparison, a sample of decay constants determined in the fitting range 95% to 90% of saturation current, is listed in table 4. The values in the table are determined at the same operating parameters as those in table 3. The time constants thus obtained are consistently twice as large as those acquired from fits to the full length of the transient, but the relative uncertainty stays almost the same.

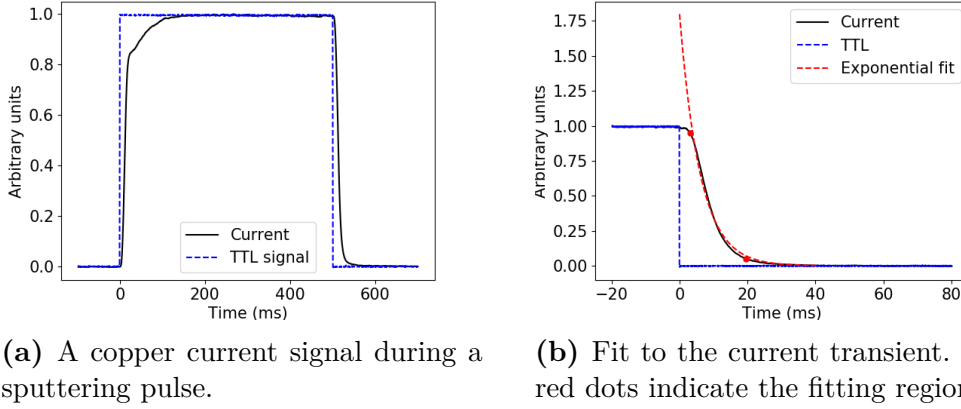
**Table 3.** Standard deviations and relative uncertainties of the average time constants of the transients obtained for the copper ions from the parameter sweep experiment at the default setting of 300 W microwave heating power, -700 V sputtering voltage,  $B_{\min}/B_{\text{ECR}} = 0.68$  and oxygen pressure set to produce a leak current of 1 mA. The time constants presented in the table were obtained from fits to the full length of the transients.

Ion	Average time constant (ms)	Standard deviation (ms)	Relative uncertainty (%)
$^{63}\text{Cu}^{10+}$	4.8	0.5	10.4
$^{63}\text{Cu}^{11+}$	6.9	0.9	13.0
$^{63}\text{Cu}^{14+}$	13.3	2.7	20.3
$^{63}\text{Cu}^{15+}$	15.5	2.8	18.1
$^{63}\text{Cu}^{17+}$	17.2	3.0	17.4

**Table 4.** Time constants obtained from fits to the beginning of the transient – i.e. with the transient current within the range 95% to 90% of the saturation current. The tabulated time constants are obtained at the same ion source operating settings as the ones in table 3.

Ion	Average time constant (ms)	Standard deviation (ms)	Relative uncertainty (%)
$^{63}\text{Cu}^{10+}$	8.3	1.2	14.5
$^{63}\text{Cu}^{11+}$	12.1	1.9	15.7
$^{63}\text{Cu}^{14+}$	26.2	8.5	32.4
$^{63}\text{Cu}^{15+}$	28.8	4.5	15.6
$^{63}\text{Cu}^{17+}$	32.7	9.2	28.1

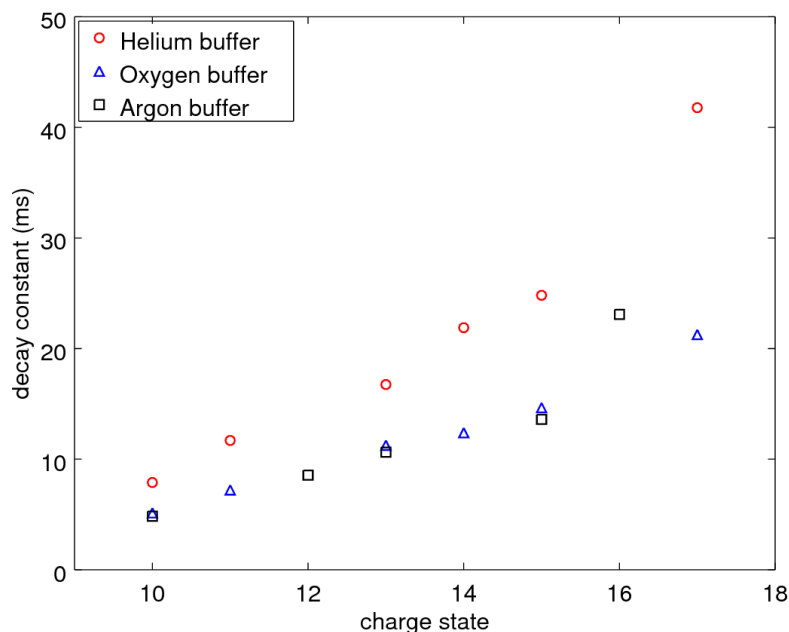
### 6.3 Parameter sweep results



**Figure 44.** Examples of a  $^{63}\text{Cu}^{11+}$  current signal measured with the oscilloscope (a), and a fit to the current transient for the same signal (b). The TTL signal corresponds to the normalized sputtering voltage (voltage up = sputtering on). The ion source parameters were  $B_{\text{min}}/B_{\text{ECR}} = 0.64$  at a heating power of 300 W. The sputtering voltage was  $-700$  V.

An example of the current signals measured with the oscilloscope is given in figure 44a. As the sputtering bias is switched on, the ion current begins to rise. There is a small delay due to the ionization time, which can be better seen in the example figure for the fast sputtering experiment – see figure 52. Meanwhile, in figure 44b is shown an example of the exponential fits made according to equation (53). Here also a small delay can be observed after the sputtering is ceased. The delay is probably due to the lower charge state ions, which feed the number density of the higher charge state ions and thus maintain their equilibrium. These example figures are representative of all the currents obtained.

### 6.3.1 The effect of the buffer gas species



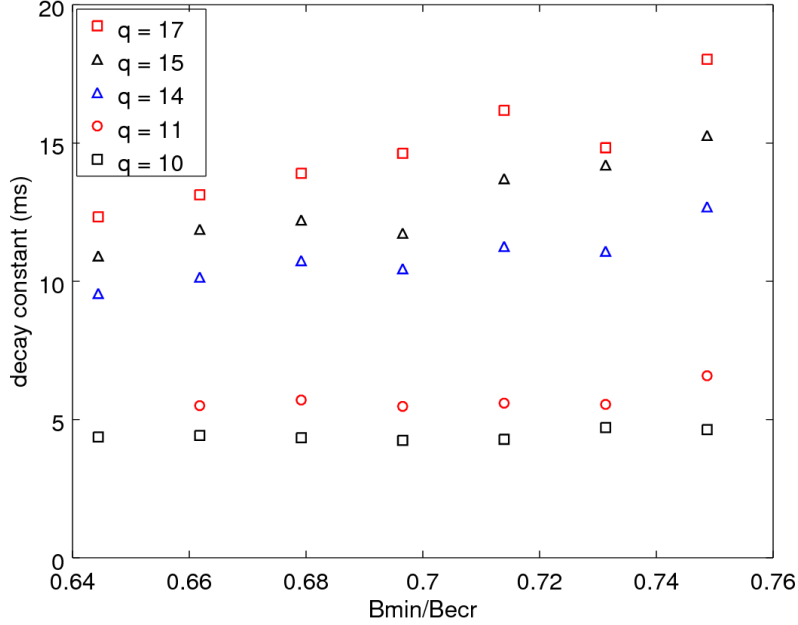
**Figure 45.** The decay constant of the ion current transient for different  $^{63}\text{Cu}$  charge states in various buffer plasmas. Plasma chamber pressures: Argon plasma:  $1.8 \times 10^{-7}$  mbar, oxygen plasma  $1.4 \times 10^{-7}$  mbar, helium plasma  $1.3 \times 10^{-7}$  mbar (in  $\text{N}_2$  calibration of the pressure gauge).

Figure 45 indicates, that the time constant is larger for lighter buffer gas species: e.g. the time constant for  $^{63}\text{Cu}^{14+}$  is 12.4 ms in oxygen plasma, but 21.9 ms in helium. This is probably due to ion cooling due to gas mixing effects – primarily the collisional mass effect and charge dilution effects. That is: the copper ions are depleted of their energy in collisions with the lighter ions of the buffer gas, and simultaneously the poorly confined low charge state ions of the buffer gas carry out energy from the plasma.

The figure also shows, that the time constant increases approximately linearly with the charge state: the decay constant in the oxygen buffer for  $^{63}\text{Cu}^{10+}$  is 5.1 ms while for  $^{63}\text{Cu}^{17+}$  it is 21.3 ms. This behavior is in accordance with measurements of the charge state dependence of the confinement time made by other authors [14] and indicates the ambipolar diffusion model for ion confinement. However, it should be recalled that an increase of the ion temperature with the charge state could also reproduce the linear dependence of the confinement time on the charge state.

The decrease in the average charge state of the plasma caused by a lighter buffer gas also causes the plasma potential to decrease. This in turn decreases the ambipolar losses by weakening the ambipolar electric field, which accelerates ions out of the plasma, thus improving ion confinement.

### 6.3.2 The effect of the minimum-B field



**Figure 46.** The decay constant of the ion current transient for different  $^{63}\text{Cu}$  charge states as a function of the  $B_{\min}/B_{\text{ECR}}$  structure of the ECRIS magnetic field.

The effect of the  $B_{\min}/B_{\text{ECR}}$ -parameter is strongest for the higher charge states, where the increase of the parameter causes an increase in the time constant. For example, the time constant of  $^{63}\text{Cu}^{17+}$  ranges from 12.3 ms at  $B_{\min}/B_{\text{ECR}} \simeq 0.64$  to 18.0 ms at  $B_{\min}/B_{\text{ECR}} \simeq 0.75$ . Because ions are not confined magnetically, changes in the magnetic field do not affect them directly. The electrons, however, experience its effects strongly. The increase of  $B_{\min}/B_{\text{ECR}}$  causes the gradient of the magnetic field at resonance to decrease – i.e. the resonance zone becomes broader – and thus the electron heating improves. Thus, the hot electron population increases and the potential dip becomes deeper, which strengthens ion confinement – particularly for the HCIs.

The observed behavior of the decay constant is in accordance with findings showcased in [65], represented in figure 47. The figure shows how the (normalized) beam currents for  $\text{He}^{2+}$ ,  $\text{O}^{7+}$  and  $\text{Ar}^{14+}$  ions increase as the value of the  $B_{\min}/B_{\text{ECR}}$ -parameter is increased, until the plasma becomes unstable at strong magnetic fields. This is explicable by a corresponding increase in the respective ion densities in the plasma, which implies an extended confinement time.

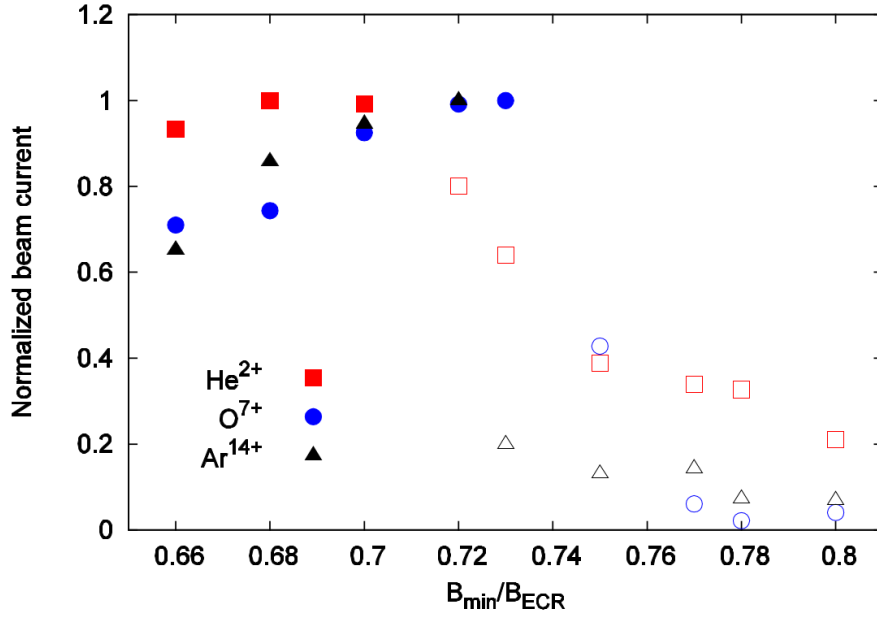


**Figure 47.** The JYFL 14 GHz ECRIS beam currents for  $\text{He}^{2+}$ ,  $\text{O}^{7+}$  and  $\text{Ar}^{14+}$  as a function of the parameter  $B_{\min}/B_{\text{ECR}}$ . The solid points correspond to stable currents, and the hollow points to unstable currents. From [65]

### 6.3.3 The effect of the injection pressure

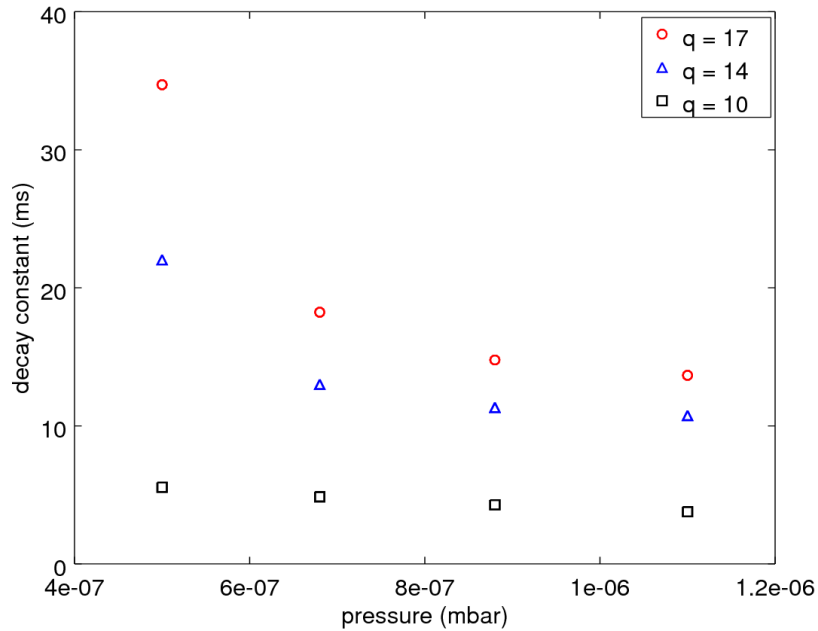


**Figure 48.** The decay constant of the ion current transient for different  $^{63}\text{Cu}$  charge states as a function of the pressure in the injection end of the ion source ( $\text{N}_2$  calibration!).

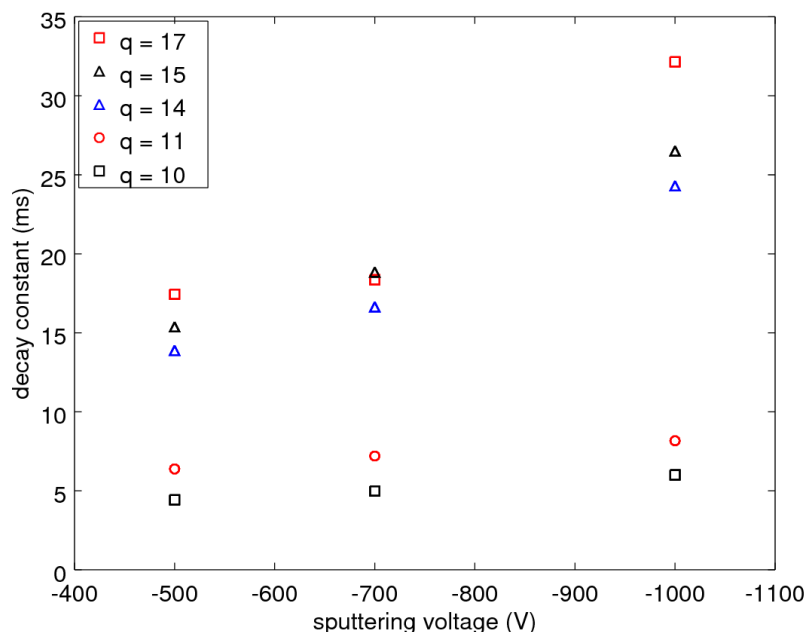
In the pressure sweep, it was found that the value of the decay constant decreases as the pressure increases, as indicated by figure 48. For example, the confinement time of  $^{63}\text{Cu}^{17+}$  at  $5 \times 10^{-7}$  mbar was found to be 34.7 ms, while at  $1.1 \times 10^{-6}$  mbar it was only 13.7 ms. This correlates well with the fact that a low neutral pressure is a necessary condition for HCI production. Accordingly, it can be seen from the figure, that particularly the HCIs benefit from the decrease in pressure.

An increase in the neutral pressure leads to an increase in the rate of charge exchange processes, causing the average charge state of the plasma to decrease. This in turn, would lead to ion cooling due to their energy being carried out by the weakly confined low charge state ions, thus improving the ion confinement.

It can be speculated, that an increasing pressure causes the particle distributions in the plasma to become more uniform, and consequently the hot electron population responsible for the potential dip diminishes. Furthermore, the larger neutral pressure means that the electron energy is dissipated in collisions with a greater number of neutrals, which leads to a decrease in electron temperatures and a consequent decrease in the potential dip depth. With the shallower potential dip the ion confinement conditions become less favorable. It has also been observed that a higher pressure corresponds to a slightly larger plasma potential[66]. This in turn causes the ambipolar losses to increase, which worsens the confinement conditions in the plasma.

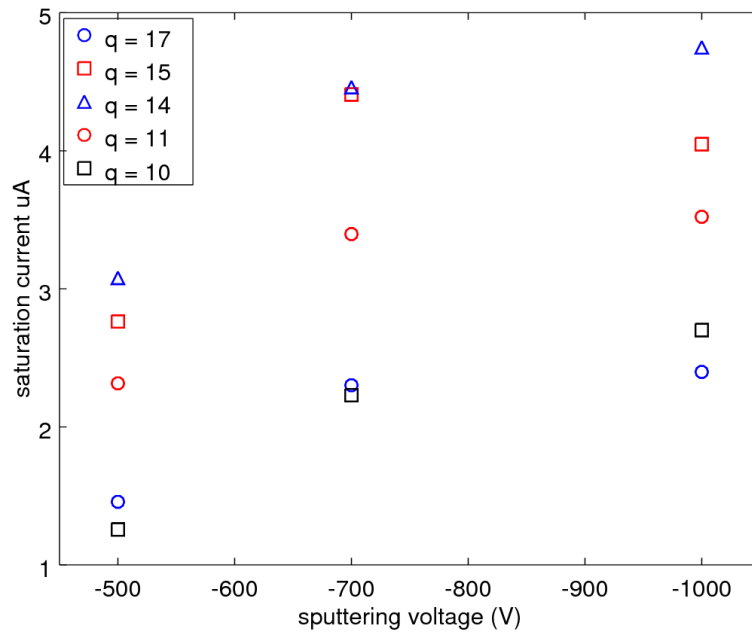
According to [14], the potential dip model becomes questionable for high ion densities – i.e. when the pressure increases – due to increased ion-ion collisionality. In [24] it was also found that the potential dip model no longer correctly describes the measured confinement times for high pressures.

### 6.3.4 The effect of sputtering voltage



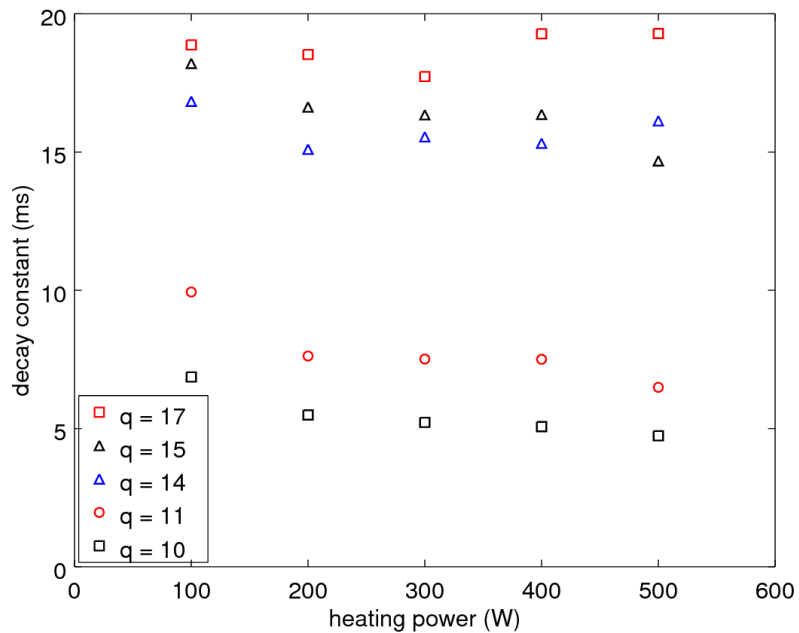
**Figure 49.** The decay constant of the ion current transient for different  $^{63}\text{Cu}$  charge states as a function of the sputtering voltage.

Figure 49 shows that the decay constant increases with the (decreasing) sputtering voltage. This is probably caused by increased gas mixing effects brought on by the larger population of copper sputtered into the plasma due to the increasing sputtering yield. Figure 50 shows the saturation currents of the different charge states of  $^{63}\text{Cu}$  in the sputtering voltage sweep. The increase in extracted copper current with the sputter sample bias correlates with the amount of copper present in the plasma. It should be recalled, however, that the extracted current has a lower average charge than the plasma, because the low charge states are more easily extracted, which means that the amount of e.g.  $^{63}\text{Cu}^{17+}$  in the plasma is larger than the figure would imply. With more copper ion targets, the poorly confined low charge oxygen ions deplete the copper ions of their energy at a greater rate and carry it out of the plasma. Again, it is found that the high charge states have the strongest reaction. As an example, the ion  $^{63}\text{Cu}^{15+}$  has a decay constant of 15.4 ms at when the sputtering voltage is -500 V, and 26.5 ms at -1000 V.



**Figure 50.** The saturation currents of  $^{63}\text{Cu}$  ions in the sputtering voltage sweep.

### 6.3.5 The effect of microwave heating power



**Figure 51.** The decay constant of the ion current transient for different  $^{63}\text{Cu}$  charge states as a function of the microwave heating power.

From figure 51 it can be seen that the microwave heating power does not have a significant effect on the time constant. This is to be expected, as the ECR heating is electron-selective, and does not directly affect the ion temperatures. However, the effect of the heating power on the electron temperature is not significant at powers higher than 200 W [20]. Thus, the increased heating power does not alter the potential dip notably, and the effect on the ion confinement is minimal.

## 6.4 Fast sputtering results

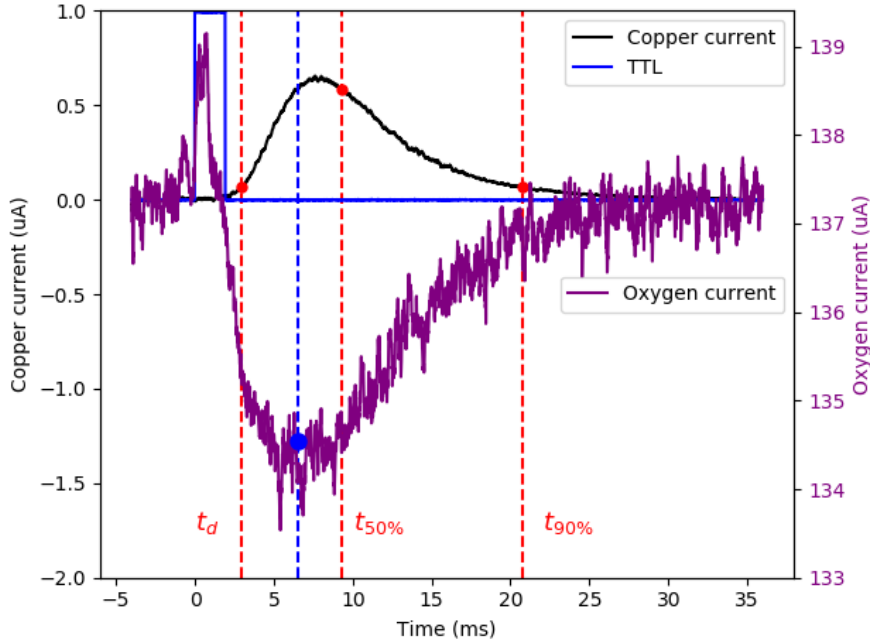


**Figure 52.** An example of a fast sputtering measurement. The current of  $^{63}\text{Cu}^{11+}$  is shown alongside the  $\text{O}^{6+}$  current from the buffer plasma. The TTL signal corresponds to the normalized sputtering voltage (voltage up = sputtering on). Here the sputtering pulse duration has been reduced to 2 ms. In red are shown the current delay time  $t_d = 2.9\text{ ms}$  and the points in time  $t_{50\%}$  and  $t_{90\%}$  when 50% and 90% respectively of the copper ions have been extracted. The dashed blue line designates the point of maximum displacement for the oxygen current at  $t = 6.9\text{ ms}$ .

In fast sputtering, the pulse duration was gradually shortened until the sputtering bias was on for no more than 0.3 ms. In figure 52 is shown an example of the currents obtained. The figure shows a  $^{63}\text{Cu}^{11+}$  ion current for a pulse width of 2 ms. It can be seen that the sputtering voltage disappears before any ions are registered at the Faraday cup (FC), meaning that the measured ion current is not disturbed by the effects of the voltage.

In the figure are illustrated the times  $t_d$ ,  $t_{50\%}$  and  $t_{90\%}$ . The delay time  $t_d$  is the time it takes for copper current to be first registered at the FC, and it is defined as the time it

takes for the current to reach 10%<sup>13</sup> of its maximum value after the sputter probe is first biased. The delay is mostly due to the time required for ionization processes to produce ions of the charge state. The times  $t_{50\%}$  and  $t_{90\%}$  are the moments in time, when 50% and 90% of the total produced ion beam has been extracted, and they can be acquired by integrating the current.

The current of  $O^{6+}$  is shown alongside the copper current. As the sputter bias is switched on, the oxygen current momentarily increases. As the copper current builds up, however, the amount of extracted oxygen decreases. This is probably due to gas mixing effects: the copper ions are cooled by the oxygen ions, and as the temperature of the oxygen decreases its confinement time increases. Consequently, the amount of extracted oxygen decreases.

### 6.4.1 Production times

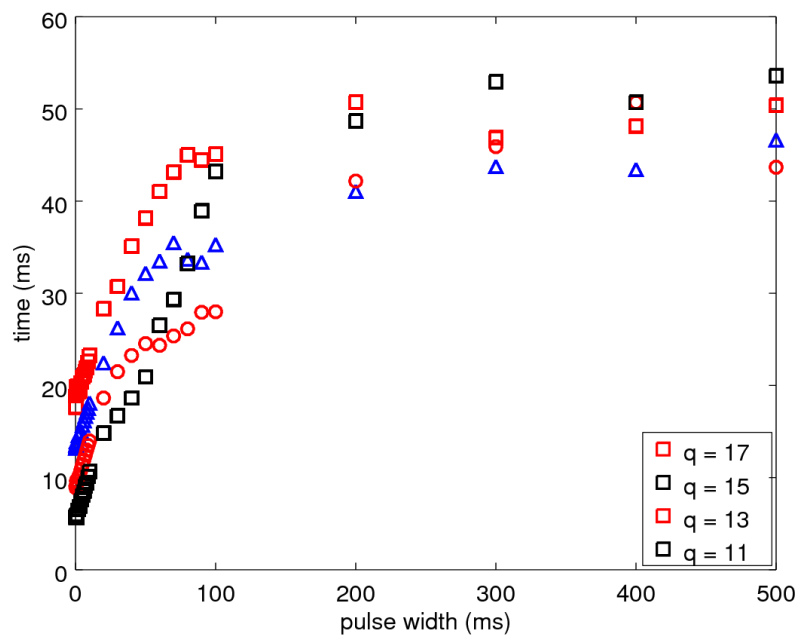


**Figure 53.** The time required for the current bump caused by the sputtering pulse to reach 90% of its maximum value as a function of the sputtering pulse width for different charge states of  $^{63}\text{Cu}$ .

<sup>13</sup>The 10% limit is sufficiently high to distinguish true ion current from noise.

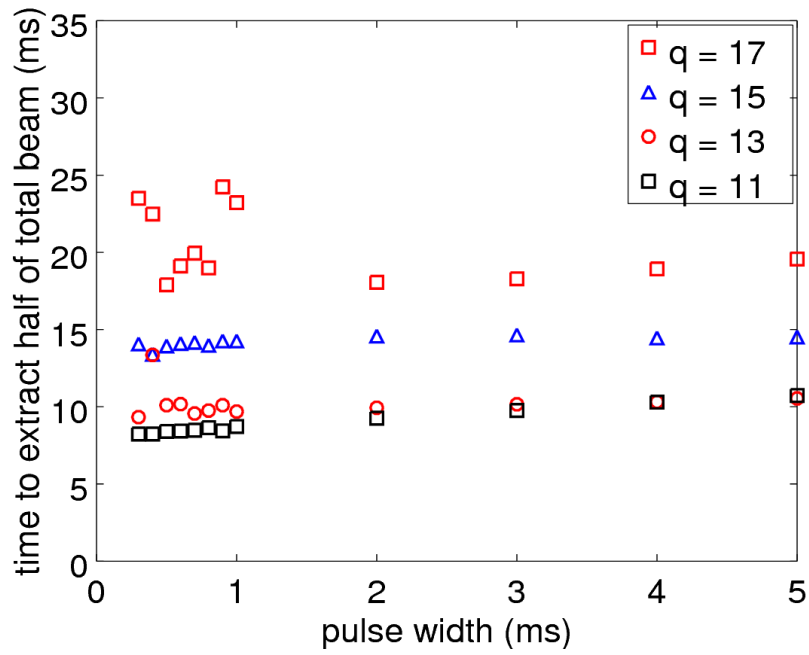
**Table 5.** Saturation times, and 50% -and 90% production times ( $t_{50\%}$  and  $t_{90\%}$ ) for  $^{63}\text{Cu}$  ion currents determined in the fast sputtering experiment.

charge state	saturation time	$t_{50\%}$ (ms)	$t_{90\%}$ (ms)
11	47.1	8.1	13.0
13	42.4	9.5	19.3
15	38.0	14.7	29.2
17	49.0	16.9	33.3

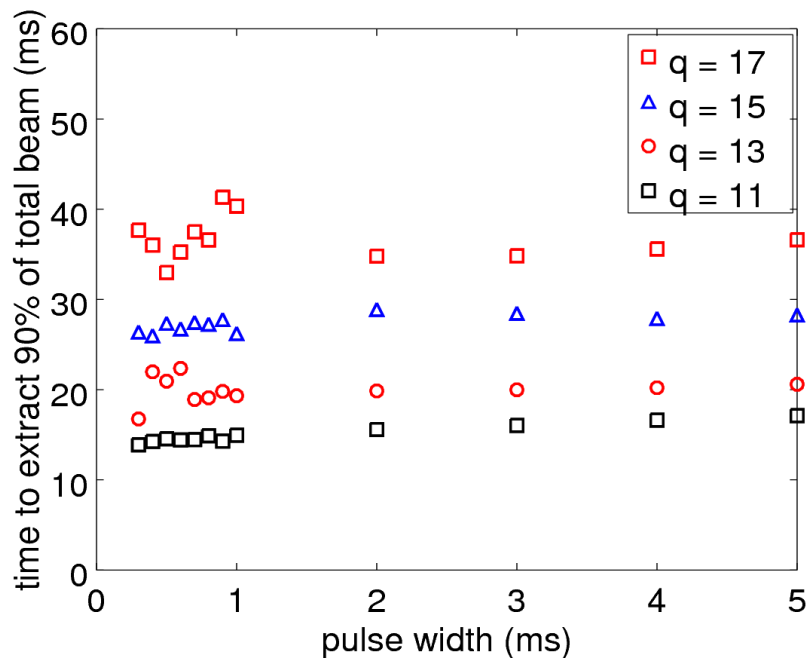
Figure 53 shows the time it takes to reach 90% of the maximum current for the  $^{63}\text{Cu}$  ion currents obtained for different pulse widths. At a pulse width of around 200 ms the ion currents reach saturation values (i.e. the equilibrium for ion densities is found). The saturation times are found as the intersection with the y-axis of a linear fit to the linear interval (200 ms – 500 ms) in the figure. The obtained saturation times are listed in table 5.

By integrating the ion currents, it is possible to find out the moment when fifty and ninety percent of the total produced ions have been extracted. These points in time are illustrated in figure 52, and their dependence on the sputtering pulse width is shown in figure 54. In the sub 1 ms pulse width region, some of the charge states deviate from linearity. This is due to the sinusoidal 50 Hz noise present in the measurement devices, brought on by the power company. Therefore, to determine the production times, a linear fit was made to the interval 2 ms – 5 ms. The production times are obtained as the intersection of the fit with the y-axis, and they are shown in table 5.

The 90% saturation time is commonly used in charge breeding sources[67, 68] as an estimate of the charge breeding time – i.e the time required for ions of charge state  $q$  to be produced. The 90% production time, however, can be seen from table 5 to be less than the saturation time. This means, that e.g.  $^{63}\text{Cu}^{17+}$  is produced 15.7 ms (32%) faster than the current saturation time would imply. The saturation time can be said to describe the ion cumulation time, rather than their production. The finding is relevant when estimating the yields of radioactive ions.



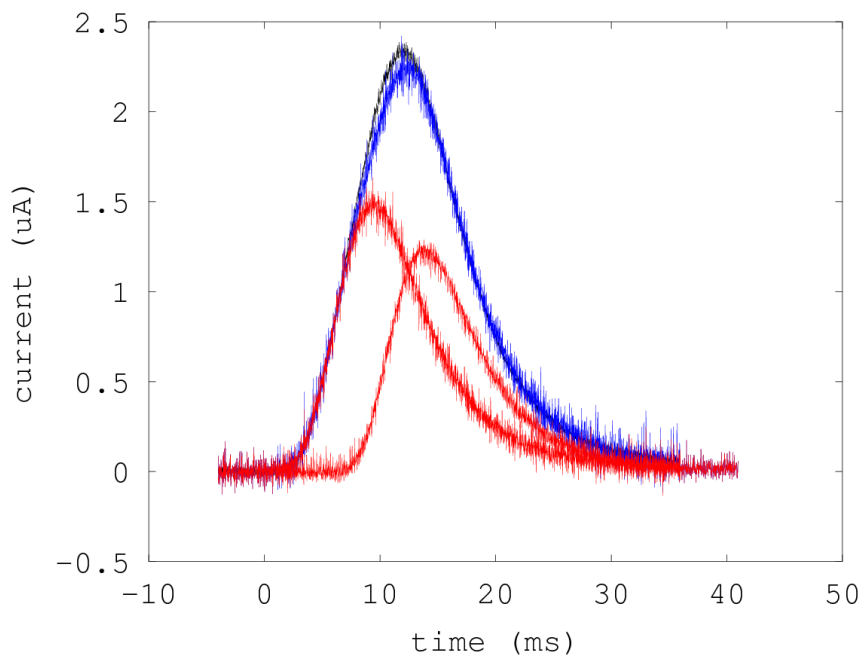
(a)



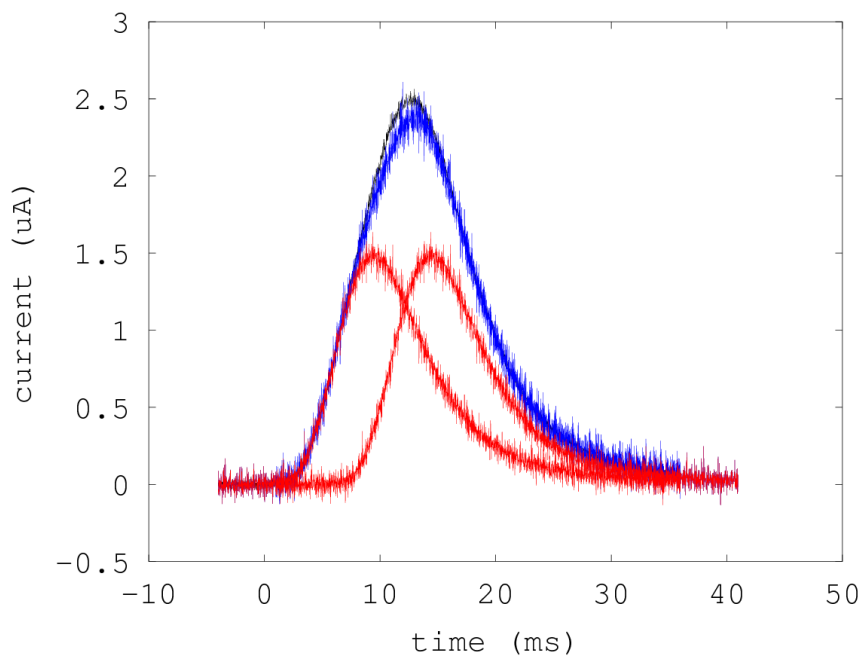
(b)

**Figure 54.** The 50% (a) and 90% (b) extraction times for the ion currents in the fast sputtering experiment as functions of the sputtering pulse width.

### 6.4.2 Superpositions

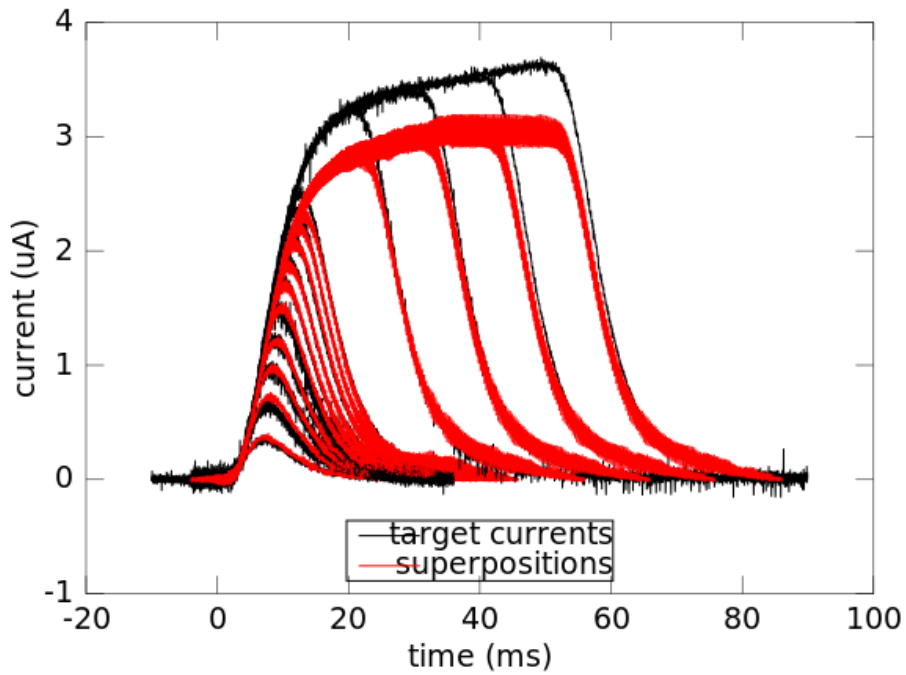


(a)

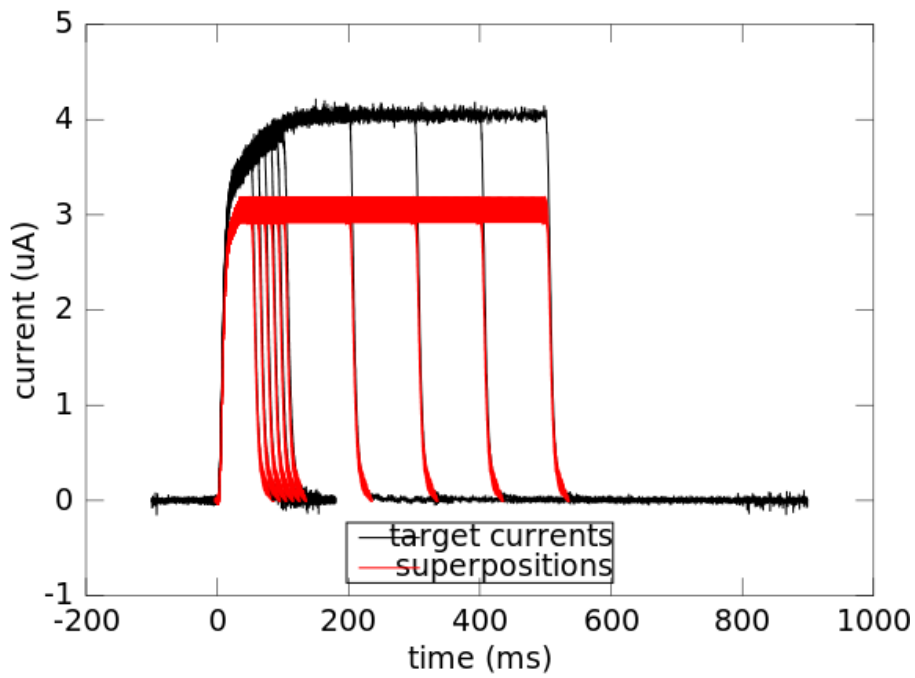


(b)

**Figure 55.** Currents measured in the fast sputtering experiment for  $^{63}\text{Cu}^{11+}$  obtained from sputter pulses of duration 5 ms and 4 ms (a), and 5 ms and 5 ms (b) are superposed and compared to the actually measured currents (obtained from 9 ms and 10 ms pulses respectively). The superposed currents are shown in red, the superposition in blue and the actually measured current in black.



(a)



(b)

**Figure 56.** Comparisons of the actually measured  $^{63}\text{Cu}^{11+}$  target currents to superposition currents obtained by shifting and superposing with itself the current bump from a 0.3 ms sputtering pulse. The current bump is superposed with itself three times to obtain an equivalent of the 1 ms sputter pulse current bump, seven times to obtain the current bump from a 2 ms sputtering pulse, etc. Figure (a) shows comparisons to currents obtained from 1 ms – 50 ms pulses, and (b) from 50 ms – 500 ms pulses.

When the sputtering pulse becomes shorter than the ionization time, the current bumps manifest after the sputtering voltage has dissipated. For very short pulses, then, the measured currents are obtained from a plasma which is not perturbed by the probe bias. Furthermore, the shorter the sputtering pulse, the fewer copper atoms are sputtered into the plasma, and thus the lesser the disturbance caused onto the buffer gas. As such, a current bump caused by as short a sputtering pulse as possible should correspond to the least perturbed plasma. In order to compare the effects of an extended sputtering pulse to a short pulse, the currents from short pulses were time-shifted and superposed to obtain equivalents of long pulse current bumps. The purpose here, thus, is to ensure that the time constants of the current transients do not depend on the sputtering pulse width, and that they are not strongly affected by the perturbation caused by the sputter sample drawing positive ions and emitting neutrals.

In figure 55, is shown an example of the superpositions of two current signals (of  $^{63}\text{Cu}^{11+}$ ) to produce the equivalent of an actually measured current. In (a), two current bumps caused by 5 ms and 4 ms sputtering pulses respectively are summed to yield the equivalent of a current bump obtained from a 9 ms pulse. Here the 4 ms pulse current bump is first shifted by 5 ms, and then summed with the 5 ms pulse current bump. Similarly in (b) a current bump from a 5 ms pulse is shifted by 5 ms and then superposed with itself to obtain the equivalent of a current bump from a 10 ms sputtering pulse.

In figure 56 the current bump resulting from the shortest possible sputtering pulse (0.3 ms) was used to reconstruct all the measured  $^{63}\text{Cu}^{11+}$  currents. It can be seen, that the reconstructed current bumps have the same shape as the actually measured currents, but the saturation current is approximately a microamp less for the superposition. This is probably because the current bump, which was used to reconstruct the actual target currents, corresponded to a small amount of copper in the plasma. This means, that the gas mixing effects – which have the effect of increasing copper confinement times and thus HCI currents – for the small bump were not so prominent as for the currents obtained from the long pulses. The rising and decaying edges of the reconstructed current bumps correspond well to the actual currents, which indicates that the sputtering pulse width does not affect the time constant of the decay, which is considered reassuring for the conclusions of this work.

## 6.5 Buffer plasma response to sputtering

In order to get reliable data from the plasma, the disturbance caused by the diagnostic method needs to be as small as possible. Ideally, the method does not cause the plasma to be disturbed from normal ion source operating conditions. If the diagnostic perturbs the plasma, the obtained data corresponds to the perturbed state, and not to the state that the plasma is in during normal operation.

In order to determine the effect of the effect of the sputtering on the buffer plasma, measurements were made on the extracted buffer currents. It was noticed that the presence of sputtering causes the extracted currents from the buffer plasma to decrease. Here, the disturbance caused on the buffer plasma by the sputtering is defined as the maximum change in the current extracted from the buffer plasma relative to its saturation current.

The relative disturbance is determined as:

$$\text{Disturbance} = \frac{|\text{saturation current} - \text{minimum current}|}{\text{saturation current}} \cdot 100\% \quad (54)$$

There is a small uncertainty in determining the saturation current, because the offset of the current is not precisely known. For the copper currents it was possible to determine the offset, because it was known that when sputtering is off, there is no copper in the plasma and the current has to be zeroed in that region. For copper the offset was on average  $0.14 \mu\text{A}$ , and should be the same for other currents. Nevertheless, these offsets are very small in comparison to the absolute current values which are more than  $50 \mu\text{A}$ , and even  $100 \mu\text{A}$ . Even for  $\text{Ar}^{6+}$  current the offset cannot create a significant error to the relative disturbance, regardless of its small saturation current ( $\sim 7 \mu\text{A}$ ).

### 6.5.1 Response as a function of the pulse width

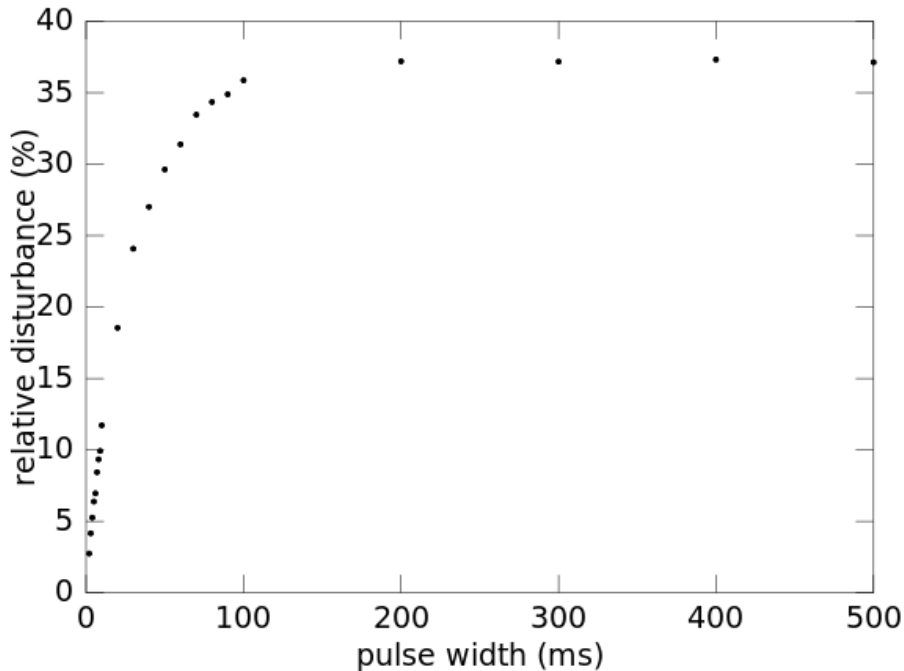


**Figure 57.** The maximum relative disturbance of the  $\text{O}^{6+}$  current as a function of the sputtering pulse width as measured in the fast sputtering experiment.

Figure 57 and 58 show the effect of the sputtering pulse width on the extracted  $\text{O}^{6+}$  current of the oxygen buffer. From figure 57 it can be seen, that the relative disturbance increases as a function of the pulse width. This is due to the increased number of copper sputtered into the plasma as a consequence of the broader sputtering pulse. The same phenomenon has been observed by O. Tarvainen *et al.* in [69], where the currents extracted from the buffer gas were observed to decrease as injection of a heavier element into the plasma was increased. Notice, that the saturation time corresponds to that of the copper current saturation (see figure 56), which indicates that the disturbance is caused by the interaction of the buffer gas plasma with copper – and not a direct consequence of

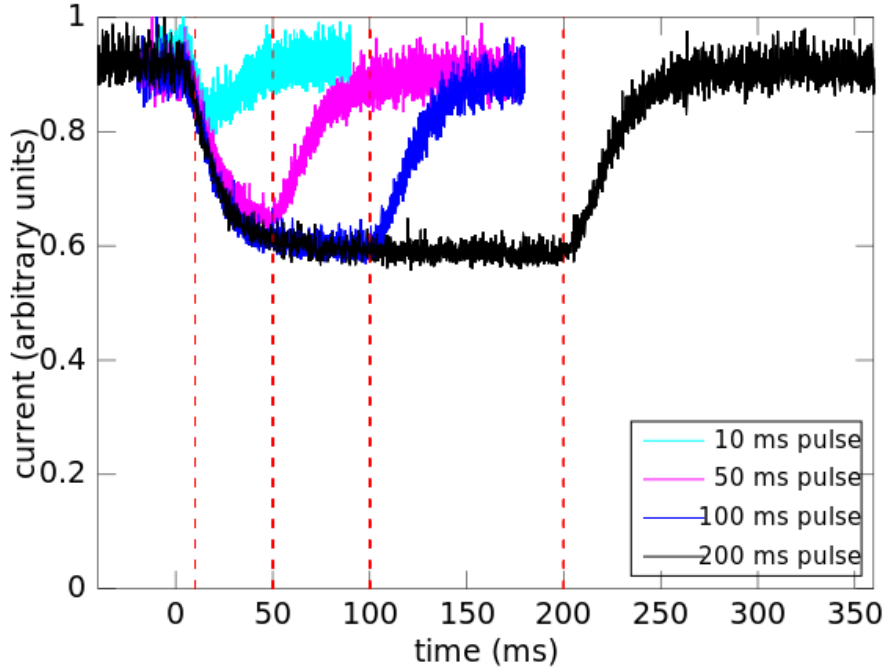
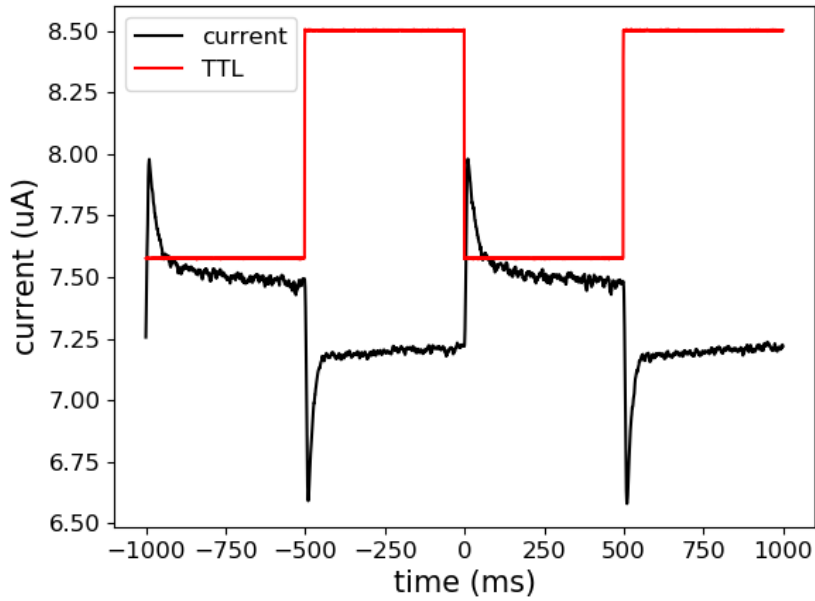


**Figure 58.** The effect of sputtering on the extracted  $O^{6+}$  ion current for different sputtering pulse widths measured in the fast sputtering experiment. The red lines mark the endpoints of the different sputtering pulses.

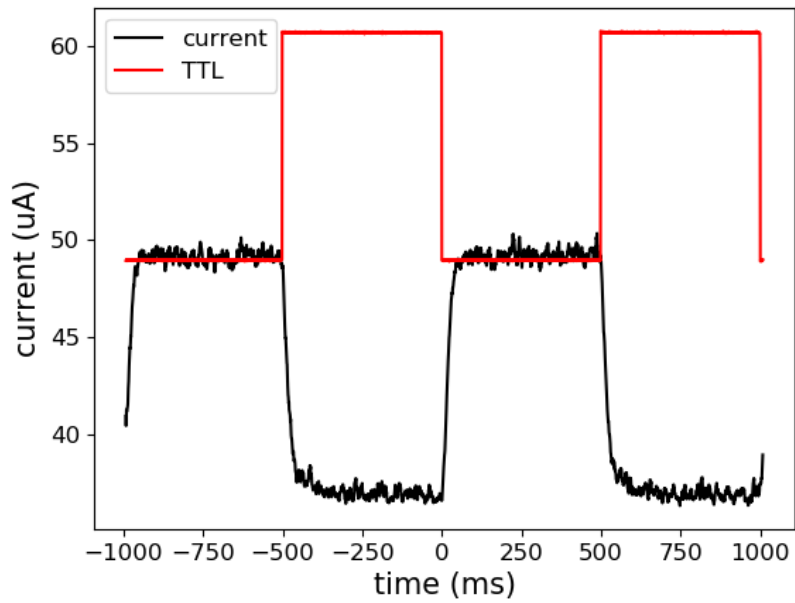
the sputter probe bias. Meanwhile, figure 58 shows how the current actually looks like as a function of the sputtering pulse width. It can be seen, that the oxygen current behaves in the opposite manner to the copper currents, and the rise time of the current after sputtering is switched off corresponds to that of the copper decay time. This implies, that the introduction of the copper element into the plasma causes collisional heating of the oxygen plasma, which leads to a diminishing oxygen particle density in analogy with the ICRH experiment by Petty *et al.* [24] where the ion heating was found to decrease HCI currents.

### 6.5.2 Response in different buffer gases

Figures 59 and 60 show the effect of the sputtering voltage on the argon and helium buffers respectively. First of all, there is a difference between the disturbance caused onto the ion currents of the two charge states of argon. The smaller current of  $Ar^{6+}$  is disturbed by a maximum of 13% while the maximum disturbance to the  $Ar^{10+}$  current is 25%. This is due to the fact that ion-ion collisionality is proportional to the charge, and consequently the gas mixing effects are stronger. Meanwhile, the effect on the light helium buffer is small regardless of the large ion current. The disturbance is greater for high charge state ions because gas mixing effects diminish their confinement time, which means that they have less time to become ionized by electron impact. Helium is not significantly affected, because it does not require a long confinement time to reach the 2+ state.



(a)



(b)

**Figure 59.** The reactions of extracted  $\text{Ar}^{6+}$  (a) and  $\text{Ar}^{10+}$  (b) currents to sputtering. The TTL signal corresponds to the normalized sputtering voltage (voltage up = sputtering on). The maximum relative disturbances in the currents, respectively, are 13% and 25%.

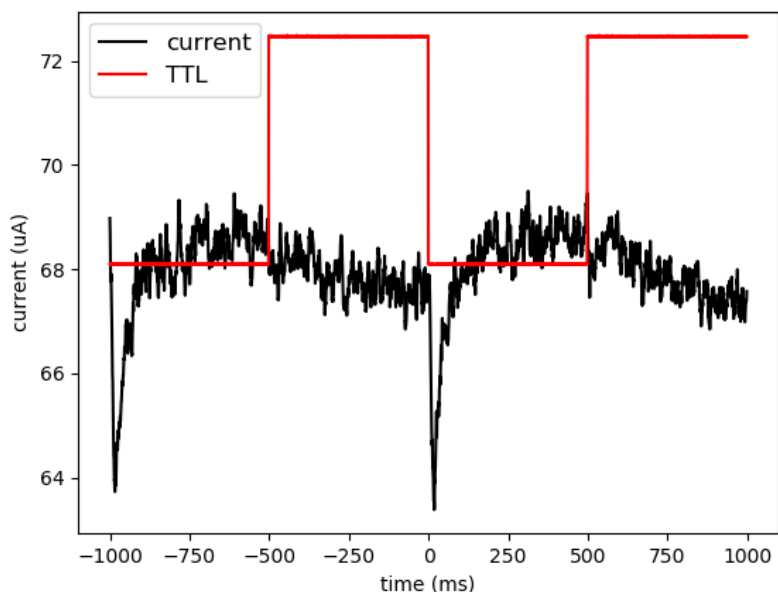


**Figure 60.** The reaction of extracted  $\text{He}^{2+}$  current to sputtering. The TTL signal corresponds to the normalized sputtering voltage (voltage up = sputtering on). The maximum relative disturbance is 7%.

## 6.6 Comparison to literature values

Neben *et al.* in reference [64] have studied current transients produced by pulsed sputtering using the transient method reproduced here to estimate confinement times for different charge states of uranium. In addition to the transient of the decaying current, they study the rising edge of the current bumps obtained in the same manner as in the fast sputtering experiment in this thesis. The experiments were performed on the the 14.5 GHz Advanced Room TEMperature Ion Source (ARTEMIS)[70] and the 18 GHz/24 GHz Superconducting Source for Ions (SuSI) [71] at the cyclotron facility at the NSCL. Their findings in the ARTEMIS source (which is more closely comparable to the JYFL 14 GHz ECRIS than the superconducting source) for the time constant are similar to those obtained from the parameter sweeps. They found the decay times of  $\text{U}^{23+}$ ,  $\text{U}^{25+}$  and  $\text{U}^{28+}$  to be on average 50.6 ms. Of course, uranium being a much heavier element, and with the measured charge states being much higher, the values are not directly comparable. Nevertheless, the order of magnitude for confinement times of the uranium HCIs is found to be in the tens of milliseconds, in agreement with what was found here.

The time constants obtained using the transient methods are vastly in excess of the confinement times determined from ion densities and end loss fluxes. For example,  $\text{Ar}^{16+}$  was estimated to have a confinement time of around 3 ms by Douysset *et al.* in [14]. Meanwhile, Petty *et al.* have determined the confinement times of different charge states of oxygen to range between 1 ms and 9 ms. The results by Douysset *et al.* are shown in figure 23, and those of Petty *et al.* in figure 61. It should be noted, that the decay constants measured here are all obtained in measurements with a light buffer gas, which

makes comparisons to experiments made on pure plasmas more complicated. By systematically varying the mixing gases and sputter sample materials, these dependencies of the decay constant could be resolved.

It seems that the confinement times determined by Petty *et al.* and Douysset *et al.* are confinement times in the traditional sense, in that they measure the extraction probability of ions at charge state  $q$ . Meanwhile, the transient method provides an estimate for the cumulative confinement time, which measures the total time that an ion spends in the plasma before being expelled at charge state  $q$ . This is corroborated by comparing the 90% production times shown in table 5, to the decay constants obtained from fits to the first few milliseconds of the transient, shown in table 4. The production times are essentially the same as the corresponding decay constants.

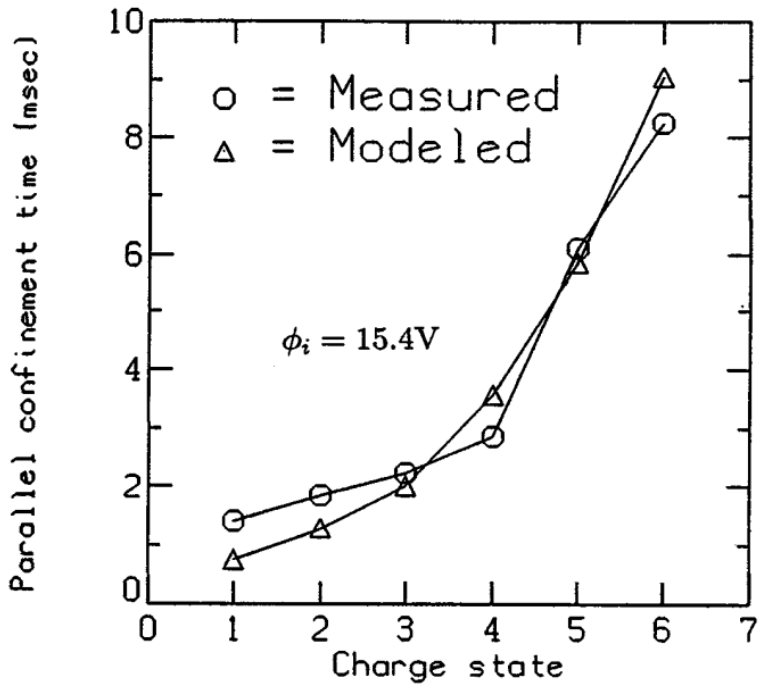


**Figure 61.** Confinement times obtained in [23] in the Constance B quadrupole ion source both experimentally and calculated through the potential dip model with a potential dip depth set to  $(\phi_i)$  15.4 eV. The ion source operating parameters were: hot electron density  $n_e^{\text{hot}} = 4.1 \times 10^{11} \text{cm}^{-3}$ , cold electron density  $n_e^{\text{cold}} = 1.2 \times 10^{11} \text{cm}^{-3}$ , at microwave frequency 10.5 GHz at 1 kW power, in a pure oxygen plasma at pressure  $5 \times 10^{-7} \text{Torr}$ .

## 7 Conclusions and future prospects

In this thesis a transient method for estimating ion confinement times was applied to estimate the ion confinement times in ECRIS plasmas. Material injection into a buffer plasma was controlled by a pulsed sputtering method. The transients of the decaying extracted current were studied based on a transient equation derived from the balance equation of ion density. The dependence of the decay constant of the current transients on the ion source parameters (buffer gas species, minimum-B field strength, neutral gas injection pressure, sputtering voltage and microwave heating power) was analyzed. Ion production times were analyzed in a fast sputtering experiment. The disturbance caused by the sputtering was also inspected.

The fitting range for the transient equation was chosen to be the full transient length, as was done by Neben *et al.* in [64]. According to Neben, the decay constant obtained from the fit is a lower limit for the ion confinement time. The effect of a shorter fitting range on the decay constant was also inspected, and it was found that fits made to the first few milliseconds of the transients produced decay constants roughly twice as long as fits to the full transient length. The assumptions made in the derivation of the transient equation imply, that the first few milliseconds of the transient are indeed the only region where the equation is valid.

The parameter sweeps showed consistently, that the dependence of the decay constant on the ion source operating parameters corresponds to that of the confinement time. The gas mixing effects of the lighter buffer gas plasma – coupled with the assumption of an electrostatic confinement model for the ions – explain many of the dependencies. Because all the measurements were made in a light buffer plasma (compared to the copper sputtering sample) the question arises, how the transient would behave in a heavier buffer gas, and in future measurements e.g. aluminum sputtering can be studied in oxygen and argon buffers. The decay constants obtained from the parameter sweeps were in accordance with the fact, that long confinement times are necessary for HCl production: The decay constants were found to be long whenever the source parameters corresponded to efficient HCl production. The cumulative confinement times are found to be so long, that they indicate the electrostatic confinement of ions in a potential dip, which is believed to form in the plasma center.

The ion production times were studied in a fast sputtering experiment, where the length of the sputtering pulse was gradually shortened until it was no longer than 0.3 ms. The current bumps thus produced were integrated to determine the time it takes for 50% and 90% of the ions created by the sputtering pulse to be extracted. The production times were compared to the current saturation times, which were found to be of the order ten milliseconds longer than the ion production times. This finding has important consequences for radioactive beam production, where the viability of the beam requires

the radioisotope to be ionized to a high charge state in a length of time short compared to its half life. Traditionally, the production time has been estimated to be similar to the saturation time, but the definition of the production time here would imply, that the production times are, in fact, much shorter. This can cause the viability of many previously neglected radioactive ion beams to be reconsidered.

The disturbance caused to the plasma by the sputtering method was studied in two ways. First of all, it was reasoned that a current bump generated by a fast sputtering pulse would correspond to a minimally perturbed plasma state, as the electric field of the sputtering voltage was on for only a short while, and the amount of substance sputtered into the plasma was small. The currents obtained from longer pulses were thus reconstructed by time shifting and summing with itself the current bump produced by the shortest sputtering pulse. It was observed, that the difference between the reconstructed and measured currents was mainly in their respective values of the absolute current, and not in the time constants. Because the reconstructed currents match well with the shape of the measured currents, it can be said that although the maximum currents are affected by sputtering, the time constant can be reliably measured. The effects of the sputtering on the buffer plasma can be circumvented to some degree, by pulsing the sputtering voltage between, for example, -500 V and -600 V. Then the relative disturbance caused by the sputtering voltage will be smaller than in the measurements performed here, where the bias was either on or off. This measurement will be performed in the future. Secondly, the buffer plasma response to the sputtering was studied. It was noticed, that sputtering causes the currents extracted from the buffer plasma to decrease. The decrease increases with the sputtering pulse width and charge state, which indicates that the increased gas mixing effects of a larger amount of substance sputtered into the plasma is the culprit to the disturbance: The gas mixing effects cause the lighter buffer gas to heat up and thus causes its confinement to worsen.

The values obtained here seem to be in mutual agreement with those acquired by Neben *et al.* in [64], where they studied the confinement of Uranium ions using the same transient method. Uranium being a much heavier element, naturally has significantly longer confinement times than the copper ions measured here (otherwise the higher charge states of uranium couldn't even be produced). Nevertheless, a decay constant in the range of fifty milliseconds is found by Neben *et al.*, in accordance with the roughly 17 ms decay constant of the  $^{63}\text{Cu}^{17+}$ . Comparison to values by Petty *et al.* and Douysset *et al.* ([23, 14]) shows that the transient method gives much larger estimates of the confinement time than those that are calculated from the ion end loss fluxes and densities. This allows the speculation, that either these two methods measure different things, or the underlying assumptions of the approaches could be questioned. The end loss flux method probably measures the confinement time as the probability for an ion having charge  $q$  to be expelled from the plasma. Meanwhile, the transient method gives an estimate of the time that an ion spends in the plasma (leaping from charge state to charge state) until it is finally expelled at charge state  $q$ . This speculation seems to agree with the fact, that the 90% production times shown in table 5 agree to within 1 ms precision with the decay constants obtained from the fits made to the first few milliseconds of the transient, shown in table 4 – recalling that the beginning of the transient is the region where the transient equation (53) is justifiably valid.

## References

- [1] R. J. Goldston and P. H. Rutherford. *Introduction to Plasma Physics*. Institute of Physics Publishing Bristol and Philadelphia, 1995.
- [2] K. Wiesemann. A Short Introduction to Plasma Physics. In *CAS–CERN Accelerator School, Ion Sources*, pages 85–122. CERN, 2013.
- [3] P. Debye and E. Hückel. *Phys. Z.*, 1923.
- [4] R. Geller. *Electron Cyclotron Resonance Ion Sources and ECR Plasmas*. IOP Publishing, 1996.
- [5] G Melin, A Girard, A Drentje, and D Hitz. Ion behavior and gas mixing in electron cyclotron resonance plasmas as sources of highly charged ions (concept). *Journal of Applied Physics*, 86, 11 1999.
- [6] G D Shirkov. A classical model of ion confinement and losses in ecr ion sources. *Plasma Sources Science and Technology*, 2(4):250, 1993.
- [7] M. Sakildien, O. Tarvainen, R. Kronholm, I. Izotov, V. Skalyga, T. Kalvas, P. Jones, and H. Koivisto. Experimental Evidence on Microwave Induced Electron Losses from ECRIS Plasma. *Physics of Plasmas*, 25:062502, 2018.
- [8] V. P. Pastukhov. *Review of Plasma Physics*, 13:203, 1987.
- [9] A. Girard, C. Perret, G. Melin, and C. Lécot. Modeling of Electron-Cyclotron-Resonance Ion Source and Scaling Laws. *Review of Scientific Instruments*, 69(2):1100, 1998.
- [10] O. Tarvainen. *Studies of Electron Cyclotron Resonance Ion Source Plasma Physics*. PhD thesis, University of Jyväskylä, 12 2005.
- [11] V. Mironov, S. Bogomolov, A. Bondarchenko, A. Efremov, and V. Loginov. Numerical Model of Electron Cyclotron Resonance Ion Source. *Physical Review Special Topics – Accelerators and Beams*, 18:123401, 2015.
- [12] V. Toivanen. *Studies of Electron Cyclotron Resonance Ion Source Beam Formation, Transport and Quality*. PhD thesis, University of Jyväskylä, 2013.
- [13] I. Izotov, O. Tarvainen, V. Skalyga, D. Mansfeld, T. Kalvas, H. Koivisto, and R. Kronholm. Measurement of the Energy Distribution of Electrons Escaping Minimum-B ECR Plasmas. *Plasma Sources Science and Technology*, 27:025012, 2018.
- [14] G. Douysset, H. Khodja, A. Girard, and J. P. Briand. Highly charged ion densities and ion confinement properties in an electron-cyclotron-resonance ion source. *Phys. Rev. E*, 61(3):3015–3022, 2000.

- [15] H. Tawara and T. Kato. Total and Partial Ionization Cross Sections of Atoms and Ions by Electron Impact. *Atomic Data and Nuclear Data Tables*, 36:167–353, 1987.
- [16] W. Lotz. Electron-impact ionization cross-sections and ionization rate coefficients for atoms and ions from hydrogen to calcium. *Zeitschrift für Physik*, 216(3):241–247, June 1968.
- [17] H. Knudsen, H. K. Haugen, and P-Hvelplund. Single-electron-capture cross section for medium- and high-velocity, highly charged ions colliding with atoms. *Phys. Rev. A.*, 23(2):597, 1981.
- [18] G. D. Shirkov, C. Mühle, G. Musiol, and G. Zschornack. Ionization and Charge Dispersion in Electron Cyclotron Resonance Ion Sources. *Nuclear Instruments and Methods A*, 302:1–5, 1991.
- [19] G. Melin et al. Recent Developments and Future Projects on ECR Ion Sources at Grenoble. In *Proceedings of the 10th International Workshop on ECR Ion Sources*, page 1, Knoxville, USA, November 1990.
- [20] C. Barué, M. Lamoureux, P. Briand, A. Girard, and G. Melin. Investigation of Hot Electrons in Electron-Cyclotron-Resonance Ion Sources. *Journal of Applied Physics*, 76(5):2662, 1994.
- [21] G. Melin, A. G. Drentje, A. Girard, and D. Hitz. Ion Behavior and Gas Mixing in Electron Cyclotron Resonance Plasmas as Sources of Highly Charged Ions. *Journal of Applied Physics*, 86(9):4772, 1999.
- [22] V. Mironov, K. Stiebling, O. Hohn, H. Schmidt-Böcking, S. Runkel, A. Schempp, G. Shirkov, S. Biri, and L. Kenéz. Influence of the Biased Electrode on the Plasma Potential in ECRIS. *Review of Scientific Instruments*, 73:623, 2002.
- [23] C. Petty, D. Goodman, D. Smith, and D. Smatlak. Physics of Multiply Charged Oxygen in the Constance B Quadrupole Mirror. *Journal de Physique Colloques*, 50(C1):C1–783, 1989.
- [24] C. C. Petty, D. L. Goodman, D. L. Smatlak, and D. K. Smith. Confinement of Multicharged Ions in an Electron Cyclotron Resonance Heated Mirror Plasma. *Phys. Fluids B*, 3(3):705–713, 1991.
- [25] R. Kronholm et al. manuscript in preparation. 2018.
- [26] A. G. Drentje. The ECR Ion Source and Associated Equipment at the KVI. *Nuclear Instruments and Methods in Physics Research*, B9:526, 1985.
- [27] M. R. Jana. *Dynamics and Kinetics of Ion Impact Dissociation of Molecules*. PhD thesis, University of Calcutta, 2013.
- [28] O. Tarvainen, T. Kalvas, H. Koivisto, J. Komppula, R. Kronholm, J. Laulainen, I. Izotov, D. Mansfeld, V. Skalyga, V. Toivanen, and G. Machicoane. Limitation of the ECRIS Performance by Kinetic Plasma Instabilities (invited). *Review of Scientific Instruments*, 87:02A703, 2016.

- [29] T.D. Rognlien and T.A. Cutler. Transition from pastukhov to collisional confinement in a magnetic and electrostatic well. *Nuclear Fusion*, 20(8):1003, 1980.
- [30] P. Suominen, O. Tarvainen, and H. Koivisto. The Effects of Gas Mixing and Plasma Electrode Position on the Emittance of an Electron Cyclotron Resonance Ion Source. *Review of Scientific Instruments*, 75(5):1517–1519, 2004.
- [31] I. G. Brown, editor. *The Physics and Technology of Ion Sources*. John Wiley & Sons, Inc., 1989.
- [32] V. Toivanen, T. Kalvas, H. Koivisto, and O. Tarvainen. Double Einzel Lens Extraction for the JYFL 14GHz ECR Ion Source Designed with IBSimu. *Journal of Instrumentation*, 8(5):P05003, 2013.
- [33] D. Leitner, D. Winklehner, and M. Strohmeier. Ion Beam Properties for ECR Ion Source Injector. *Journal of Instrumentation*, 6:P07010, 2011.
- [34] L. Panitzsch, T. Peleikis, M. Stalder, and R. F. Wimmer-Schweingruber. Spatially Resolved Charge State and Current Density Distributions at the Extraction of an Electron Cyclotron Resonance Ion Source. *Review of Scientific Instruments*, 82:093002, 2011.
- [35] L. Panitzsch, T. Peleikis, M. Stalder, and R. F. Wimmer-Schweingruber. Experimental Results: Charge-State- and Current Density Distributions at the Plasma Electrode of an ECR Ion Source. In *Proceedings of the 20th International Workshop on ECR Ion Sources*, page 101, September 2012.
- [36] O. Tarvainen, P. Suominen, and H. Koivisto. A New Plasma Potential Measurement Instrument for Plasma Ion Sources. *Review of Scientific Instruments*, 75:3138, 2004.
- [37] S. Runkel, O. Hohn, K. Stiebling, A. Schempp, H. Schmidt-Böcking, V. Mironov, and G. Shirkov. Time Resolved Experiments at the Frankfurt 14 GHz Electron Cyclotron Resonance Ion Source. *Review of Scientific Instruments*, 71:912, 2000.
- [38] C. M. Lyneis. Operating Experience with the LBL ECR Source. In *International Conference on ECR Ion Sources and their Applications*, 1987.
- [39] Z. Q. Xie. State of the Art of ECR Ion Sources. In *Proceedings of the 1997 Particle Accelerator Conference (Cat. No.97CH36167)*, volume 3, pages 2662–2666, 1997.
- [40] V. Skalyga, I. Izotov, T. Kalvas, H. Koivisto, J. Komppula, R. Kronholm, J. Laulainen, and O. Tarvainen. Suppression of Cyclotron Instability in Electron Cyclotron Resonance Ion Sources by Two-Frequency Heating. *Physics of Plasmas*, 22:083509, 2015.
- [41] Z. Q. Xie and C. M. Lyneis. Two-Frequency Plasma Heating in a High Charge State Electron Cyclotron Resonance Ion Source. *Review of Scientific Instruments*, 66(8):4218–4221, 1995.
- [42] R. C. Vondrasek, R. Scott, and R. C. Pardo. title. In *Proceedings of the 16th International Workshop on ECR Ion Sources*, page 31, Berkeley, California, September 2004.

- [43] R. C. Vondrasek, R. Scott, and R. C. Pardo. ECRIS Operation with Multiple Frequencies. *Review of Scientific Instruments*, 77:03A337, 2006.
- [44] O. Tarvainen, T. Ropponen, V. Toivanen, T. Kalvas, J. Ärje, and H. Koivisto. Diagnostics of Plasma Decay and Afterglow Transient of an Electron Cyclotron Resonance Ion Source. *Plasma Sources Science and Technology*, 19:045027, 2010.
- [45] R. Geller, P. Ludwig, and G. Melin. Meta Ion Production in ECRIS (invited). *Review of Scientific Instruments*, 63:2795, 1992.
- [46] R. Harkewicz, J. Stacy, J. Greene, and R. Pardo. Solid Material Evaporation Into an Electron Cyclotron Resonance Source by Laser Ablation. *Review of Scientific Instruments*, 65(4):1104, 1994.
- [47] H. Koivisto, J. Ärje, and M. Nurmia. Metal Ion Beams from an ECR Ion Source Using Volatile Compounds. *Nuclear Instruments and Methods in Physics Research B*, 94:291, 1994.
- [48] S. Bogomolov, A. Bondarchenko, A. Efremov, K. Kuzmenkov, A. Lebedev, K. Lebedev, V. Lebedev, V. Loginov, V. Mironov, and N. Yazvitzky. Production of Intense Metal Ion Beams from ECR Ion Sources Using the MIVOC Method. *Physics of Particles and Nuclei Letters*, 12(7):824, 2015.
- [49] H. Koivisto. Production of Titanium Ion Beams in an ECR Ion Source. *Nuclear Instruments and Methods in Physics Research B*, 187:111, 2002.
- [50] R. Pardo and P. Billquist. Operating Experience with the Argonne PIIECR Ion Source System. *Review of Scientific Instruments*, 61:239, 1990.
- [51] V. Mironov, O. Hohn, S. Runkel, L. Schmidt, G. Shirkov, K. Stiebing, H. Schmidt-Böcking, and A. Schempp. Laser Ablation Plasma Injection into the Frankfurt 14 GHz ECRIS. In *14th International Workshop on ECR Ion Sources*, page 212, CERN, Geneva, Switzerland, May 1999.
- [52] A Simple Sputter Yield Calculator. <https://www.iap.tuwien.ac.at/www/surface/sputteryield>, July 2018.
- [53] R. Harkewicz, P. J. Billquist, J. P. Greene, Jr. J. A. Nolen, and R. C. Pardo. Ion Plasma Sputtering as a Method of Introducing Solid Material Into an Electron Cyclotron Resonance Ion Source. *Review of Scientific Instruments*, 66:2883, 1995.
- [54] S. Sugiyama, Y. Kato, and S. Ishii. Production of Multiply Charged Si and Fe Ions from Solid Materials by Sputtering and Evaporating Methods in a 2.45 GHz ECR Source. *Review of Scientific Instruments*, 73(2):542, 2002.
- [55] N. Matsunami, Y. Yamamura, Y. Itikawa, N. Itoh, Y. Kazumata, S. Miyagawa, K. Morita, R. Shimizu, and H. Tawara. Energy Dependence of the Yields of Ion-Induced Sputtering of Monatomic Solids. *IPPJ-AM-32 (Institute of Plasma Physics, Nagoya University Japan)*, 1983.
- [56] E. Lammentausta. Metallionisuihkujen Tuottaminen ECR-Ionilähteellä Sputterointimenetelmän Avulla. Master's thesis, University of Jyväskylä, 2004.

- [57] E. Liukkonen. New K130 Cyclotron at Jyväskylä. In *13th International Conference on Cyclotrons, Vancouver*, page 22, 1992.
- [58] H. Koivisto, P. Heikkinen, V. Hänninen, A. Lassila, H. Leinonen, V. Nieminen, J. Pakarinen, K. Ranttila, J. Ärje, and E. Liukkonen. The First Results with the New JYFL 14 GHz ECR Ion Source. *Nuclear Instruments and Methods in Physics Research B*, 174:379–384, 2001.
- [59] S. Gammino, L. Celona, G. Ciavola, M. Castro, F. Chines, and S. Marletta. Production of Intense Highly Charged Ion Beams with SERSE. In *14th International Workshop on ECR Sources, ECRIS99*, CERN, Geneva, Switzerland.
- [60] D. Hitz, A. Girard, G. Melin, S. Gammino, G. Ciavola, and L. Celona. Results and Interpretation of High Frequency Experiments at 28 GHz in ECR Ion Sources, Future Prospects. *Review of Scientific Instruments*, 73(2):509, 2002.
- [61] T. Ropponen. *Electron Heating, Time Evolution of Bremsstrahlung and Ion Beam Current in Electron Cyclotron Resonance Ion Sources*. PhD thesis, University of Jyväskylä, January 2010.
- [62] T. Ropponen, O. Tarvainen, P. Jones, P. Peura, T. Kalvas, P. Suominen, and H. Koivisto. Time Evolution of High-Energy Bremsstrahlung and Argon Ion Production in Electron Cyclotron Resonance Ion-Source Plasma. *IEEE Transactions on Plasma Science*, 37(11):2146, 2009.
- [63] D. Neben, G. Machicoane, G. Parsey, A. Pham, J. Stetson, and J. Verboncoeur. An Analysis of Fast Sputtering Studies for Ion Confinement Time. In *Proceedings of LINAC2016*, volume 4B, page 475, East Lansing, MI, USA, 2016.
- [64] D. Neben, J. Fogelman, D. Leitner, G. Machicoane, G. Parsey, A. Pham, S. Renteria, J. Stetson, L. Tobos, and J. Verboncoeur. Fast Sputtering Measurement Studies Using Uranium with the NSCL ECR Ion Sources. In *Proceedings of ECRIS2016*, page 128, Busan, Korea, 2016.
- [65] O. Tarvainen, T. Kalvas, H. Koivisto, J. Komppula, R. Kronholm, J. Laulainen, I. Izotov, D. Mansfeld, V. Skalyga, and V. Toivanen. (unpublished), 2010.
- [66] T. Ropponen. ECR-ionilähteiden plasmapotentialiaali ja ambipolaarinen diffuusio. Master’s thesis, University of Jyväskylä, August 2005.
- [67] N. Chauvin, J. Bruandet, J. Bouly, R. Geller, T. Lamy, P. Sole, P. Sortais, and J. Vieux-Rochaz. The  $1+ \rightarrow n+$  Charge Breeding Method for the Production of Radioactive and Stable Continuous/Pulsed Multi-Charged Ion Beams. In *International Workshop on ECR Sources 14*.
- [68] R. Vondrasek. On-Line Charge Breeding Using ECRIS and EBIS. *Nuclear Instruments and Methods in Physics Research B*, 376:16, 2016.
- [69] O. Tarvainen, T. Lamy, J. Angot, P. Delahaye, L. Maunoury, J. Choinski, L. Standylo, A. Galatà, and H. Koivisto. Injected  $1+$  Ion Beam as a Diagnostics Tool of Charge Breeder ECR Ion Source Plasmas. *Plasma Sources Sci. Technol.*, 2015.

- [70] G. Machicoane et al. *Review of Scientific Instruments*, 77:03A322, 2006.
- [71] G. Machicoane et al. First Results at 24 GHz with the Superconducting Source for Ions (SuSI). In *Proceedings of ECRIS14*, Nizhny Novgorod, Russia, 2014. Paper MOOMMH03.